Mon. Not. R. Astron. Soc. **314**, 511–545 (2000)

Starburst-driven galactic winds – I. Energetics and intrinsic X-ray emission

David K. Strickland[1]★† and Ian R. Stevens[2]★

[1]*Department of Physics and Astronomy, The Johns Hopkins University, 3400 North Charles Street, Baltimore, MD 21218, USA*
[2]*School of Physics and Astronomy, The University of Birmingham, Edgbaston, Birmingham B15 2TT*

Accepted 1999 December 14. Received 1999 December 6; in original form 1999 September 13

ABSTRACT

Starburst-driven galactic winds are responsible for the transport of mass, in particular metal-enriched gas, and energy out of galaxies and into the intergalactic medium. These outflows directly affect the chemical evolution of galaxies, and heat and enrich the intergalactic and intercluster medium.

Currently, several basic problems preclude quantitative measurements of the impact of galactic winds: the unknown filling factors of, in particular, the soft X-ray-emitting gas prevent accurate measurements of densities, masses and energy content; multiphase temperature distributions of unknown complexity bias X-ray-determined abundances; unknown amounts of energy and mass may reside in hard to observe $T \sim 10^5$ K and $T \sim 10^{7.5}$ K phases; and the relative balance of thermal versus kinetic energy in galactic winds is not known.

In an effort to address these problems, we perform an extensive hydrodynamical parameter study of starburst-driven galactic winds, motivated by the latest observation data on the best-studied starburst galaxy M82. We study how the wind dynamics, morphology and X-ray emission depend on the ISM distribution of the host galaxy, the starburst star formation history and strength, and the presence and distribution of mass-loading by dense clouds. We also investigate and discuss the influence of finite numerical resolution on the results of these simulations.

We find that the soft X-ray emission from galactic winds comes from low filling factor ($\eta \lesssim 2$ per cent) gas, which contains only a small fraction ($\lesssim$10 per cent) of the mass and energy of the wind, irrespective of whether the wind models are strongly mass-loaded or not. X-ray observations of galactic winds do not directly probe the gas that contains the majority of the energy, mass or metal-enriched gas in the outflow.

X-ray emission comes from a complex phase-continuum of gas, covering a wide range of different temperatures and densities. No distinct phases, as are commonly assumed when fitting X-ray spectra, are seen in our models. Estimates of the properties of the hot gas in starburst galaxies based on fitting simple spectral models to existing X-ray spectra should be treated with extreme suspicion.

The majority of the thermal and kinetic energy of these winds is in a volume-filling hot, $T \sim 10^7$ K, component which is extremely difficult to probe observationally because of its low density and hence low emissivity. Most of the total energy is in the kinetic energy of this hot gas, a factor that must be taken into account when attempting to constrain wind energetics observationally. We also find that galactic winds are efficient at transporting large amounts of energy out of the host galaxy, in contrast to their inefficiency at transporting mass out of star-forming galaxies.

Key words: methods: numerical – ISM: bubbles – ISM: jets and outflows – galaxies: individual: M82 – galaxies: starburst – X-rays: galaxies.

† Send offprint requests to D. K. Strickland.
★ E-mail: dks@pha.jhu.edu (DKS); irs@star.sr.bham.ac.uk (IRS)

1 INTRODUCTION

Starbursts, episodes of intense star formation lasting $\lesssim 10^8$ yr, are now one of the cornerstones of the modern view of galaxy formation and evolution. Starbursts touch on almost all aspects of extragalactic astronomy, from the processes of primeval galaxy formation at high redshift to being a significant mode of star formation even in the present epoch, and covering systems of all sizes from dwarf galaxies to the dust-enshrouded starbursts in ultraluminous merging galaxies (see Heckman 1998 for a recent review).

An inescapable consequence of a starburst is the driving of a powerful galactic wind (total energy $10^{54} \leq E \leq 10^{58}$ erg, velocity $v \gtrsim 10^3\,\mathrm{km\,s^{-1}}$) from the host galaxy into the intergalactic medium (IGM) due to the return of energy and metal-enriched gas into the interstellar medium (ISM) from the large numbers of massive stars formed during the burst (Chevalier & Clegg 1985, hereafter CC; McCarthy, Heckman & van Breugel 1987).

The best-developed theoretical model for starburst-driven galactic winds, elaborated over the years by various workers (see the review by Heckman, Lehnert & Armus 1993; see also Tomisaka & Bregman 1993, hereafter TB, and Suchkov et al. 1994, hereafter S94), is of outflows of supernova-ejecta and swept-up ISM driven by the mechanical energy of multiple type II supernovae and stellar winds from massive stars. This paradigm is very successful at explaining almost all of the observed properties of galactic winds, and can reproduce quantitatively what is known of the kinematics and energetics of observed local starburst-driven outflows.

Galactic winds are unambiguously detected in many local edge-on starburst galaxies (Lehnert & Heckman 1996), and their presence can even be inferred in starbursts at high redshift (e.g. Pettini et al. 2000). Filamentary optical emission-line gas, soft thermal X-ray emission and non-thermal radio emission, all extended preferentially along the minor axis of the galaxy and emanating in a loosely collimated flow from a nuclear starburst, are all classic signatures of a galactic wind. In the closest and brightest edge-on starburst galaxies the outflow can be seen in all phases of the ISM, from cold molecular gas to hot X-ray-emitting plasma (Dahlem 1997).

Galactic winds are of cosmological importance in several ways.

(i) The transport of metal-enriched gas out of galaxies by such winds affects the chemical evolution of galaxies and the IGM. This effect may be extremely important in understanding the chemical evolution of dwarf galaxies, where metal ejection efficiencies are expected to be higher (Dekel & Silk 1986; Bradamante, Matteucci & D'Ercole 1998).

(ii) Galactic winds may also be responsible for reheating the IGM, evidence of which is seen in the entropy profiles of gas in the intercluster medium (ICM) of groups and clusters (Ponman, Cannon & Navarro 1999). A substantial fraction of the metals now in the ICM were probably transported out of the source galaxies by early galactic winds (e.g. Loewenstein & Mushotzky 1996).

(iii) Galactic winds are an extreme mode of the 'feedback' between star formation and the ISM. This feedback is a necessary, indeed vital, ingredient of the recipes for galaxy formation employed in todays cosmological *N*-body and semi-analytical models of galaxy formation. An aspect of feedback where galactic winds will have an important effect, and where the existing prescriptions for feedback need updating with less ad hoc models, is in the escape of hot gas from haloes of galaxies, in particular low-mass galaxies. This directly affects the faint end of the galaxy luminosity function in semi-analytical galaxy formation models (e.g. Cole et al. 1994; Kauffman, Guiderdoni & White 1994; Somerville & Primack 1999), as recently discussed by Martin (1999).

Assessing the importance of starburst-driven winds quantitatively requires going beyond what is currently known of their properties. It is necessary to make more quantitative measurements of parameters such as mass-loss rates, energy content and chemical abundances, and how these relate to the properties of the underlying starburst and host galaxy.

This in turn requires a deeper understanding the basic physics of such outflows, and the mechanisms underlying the multiwavelength emission we see. In particular, the origin of the soft X-ray emission seen in galactic winds is currently uncertain, with several different models currently being advanced (as we shall discuss below). This uncertainty in what we are actually observing makes estimating the total mass and energy content of these winds difficult.

Recent theoretical and hydrodynamical models (De Young & Heckman 1994; Mac Low & Ferrara 1999; D'Ercole & Brighenti 1999) suggest that starburst-driven winds are in general not efficient at ejecting significant amounts of the host galaxy's ISM, in the single-burst scenarios that have been explored until now. More complex star formation histories have yet to be explored numerically, but qualitative arguments suggest mass-loss rates will be even lower than in single-burst scenarios (Strickland & Stevens 1999). This is beginning to overturn the popular concept of catastrophic mass-loss in dwarf galaxies due to galactic winds advanced by Dekel & Silk (1986) and Vader (1986).

Despite the sophistication of these and other recent models, it has not been shown that these simulations reproduce the observed kinematics, energetics and emission properties of any real starburst-driven outflow. A very wide range of model parameters can produce a bipolar outflow – only a relatively small number of models have been run, and these have explored only a limited parameter space. More rigorous tests and comparisons of the *observable* properties of the different theoretical models against the available observational data are now required to judge the relative successes and failures of the current theory.

Observational attempts to directly measure the mass and energy content of galactic winds, using optical or X-ray observations (cf. Martin 1999; Read, Ponman & Strickland 1997; Strickland, Ponman & Stevens 1997) have been made. Unfortunately, these may be accurate only to an order of magnitude, given that the volume-filling factors of the cool $T \sim 10^4$ K and hot $T \sim 10^{6.5}$ K gas phases that are probed by these observations are unknown. This uncertainty in filling factor affects all observational studies of the hot gas in starburst galaxies, such as Wang et al. (1995), Dahlem et al. (1996) and Della Ceca, Griffiths & Heckman (1997), to name only a few.

The soft X-ray emission from galactic winds and starburst galaxies is well fitted by thermal plasma models of one or more components with temperatures in the range $kT \sim 0.1$ to 1.0 keV (cf. Ptak et al. 1997; Read et al. 1997; Dahlem, Weaver & Heckman 1998 among many others).

A variety of models have been put forward to explain the soft X-ray emission from galactic winds. Currently, the origin and physical state of the emitting gas is not clear, either observationally or theoretically. There is little disagreement that the diffuse

soft X-ray emission comes from some form of hot gas. The main uncertainties lie in the filling factor and thermal distribution of this gas. These in turn affect the degree to which soft X-ray observations provide a good probe of the important properties of galactic winds that we need to measure – the mass and energy content and the chemical composition.

Different models for the origin of the soft X-ray emission from galactic winds range from shock-heated clouds (of low volume-filling factor) embedded in a more tenuous wind (e.g. CC), through conductive interfaces between hot and cold gas (e.g. D'Ercole & Brighenti 1999), to emission from a volume-filling hot gas where the wind density has been increased by the hydrodynamical disruption of clouds overrun by the wind (e.g. Suchkov et al. 1996, hereafter S96).

In M82 the X-ray emission occupies a similar area in projection to both the emission line filaments (Watson, Stanger & Griffiths 1984; Shopbell & Bland-Hawthorn 1998) and to the radio emission (Seaquist & Odegard 1991). Although existing X-ray observations of M82 and other galactic winds do not have the spatial resolution necessary to constrain the exact relationship between the emission-line gas and the hot gas, the general similarity in the two spatial distributions have prompted models where the soft X-ray emission comes from shock-heated clouds (cf. Watson et al. 1984; CC). In this hypothesis both the optical line emission and the soft X-ray emission come from clouds shocked by a fast tenuous, and presumably hotter, wind that the clouds are embedded in. The wind drives fast shocks into less tenuous clouds causing soft thermal X-ray emission, and slower shocks into denser clouds causing optical emission. The clouds occupy very little of the total volume, but dominate the total emission. The distribution of clouds within the wind hence determines both the observed distribution of optical and X-ray emission. The temperature of the X-ray-emitting gas is determined by the speed of the shock waves driven into them, which is then determined by the density of the clouds and the density and velocity of the wind running into them. Two-dimensional (2D) hydrodynamical models of galactic winds (e.g. Tomisaka & Ikeuchi 1988 hereafter TI; TB; S94) strongly favour interpretations of the X-ray emission coming from shock-heated ISM overrun by the wind.

In this model we do not see the 'wind' itself, as it is too tenuous to emit efficiently enough to be detected. If this model is correct, then X-ray observations do not directly probe the heavy-element-enriched wind fluid that drives the outflow and contains most of the total energy.

D'Ercole & Brighenti (1999) suggest that S94's conclusion, namely that the majority of soft X-ray emission in their hydrodynamical simulations arise from shocked disc and halo gas, was incorrect. They point out that the numerically unresolved interfaces between cold and hot gas have the correct temperature and density to produce large amounts of soft X-ray emission. Such regions are almost inevitable in hydrodynamical simulations, and would be very difficult to distinguish from regions of cold disc gas shock-heated by the surrounding hot wind material.

In reality, thermal conduction can lead to physically broadened interface regions, which could be a significant source of soft thermal X-ray emission in galactic winds. Such conductive interfaces are believed to dominate the X-ray emission in wind-blown bubbles (Weaver et al. 1977), which are very similar to the superbubbles that young starbursts blow.

Fabbiano (1988) and Bregman, Schulman & Tomisaka (1995) explicitly interpret the X-ray emission from M82 in terms of it being from an adiabatically expanding hot wind, in contrast to shock-heated clouds model above. The temperature and density of the gas in such a model of a volume-filling X-ray-emitting wind is determined by the energy and mass injection rates within the starburst, and also by the outflow geometry which controls the degree of adiabatic expansion and cooling the wind experiences. If this model is correct, then soft X-ray observations provide a good probe of the hot gas driving the outflow, and hence of the metal abundance, mass and energy content of starburst-driven winds.

CC had explicitly rejected the wind itself being the source of the X-ray emission seen in M82 by Watson et al. (1984). The problem is that, for reasonable estimates of the wind's mass and energy injection rate based on M82's supernova (SN) rate, the outflow has a very low density. As the X-ray emissivity is proportional to the square of the density, the resulting X-ray luminosity is extremely low. For example, for a SN rate of $0.1\,\mathrm{yr}^{-1}$ with a resultant wind mass injection rate of $\dot{M}_{\mathrm{w}} \sim 1\,\mathrm{M}_{\odot}\,\mathrm{yr}^{-1}$, and a starburst region of radius $R_{*} = 150\,\mathrm{pc}$, the resulting total 0.1–2.4 keV X-ray luminosity from within a radius $R = 10 \times R_{*}$ is only $3.2 \times 10^{37}\,\mathrm{erg\,s}^{-1}$, about 60 per cent of which comes from within the starburst region itself. This is 10^{-5} times the starburst's wind energy injection rate, and considerably less than the observed 0.1–2.4 keV luminosity of M82's wind of $L_{\mathrm{X}} \sim 2 \times 10^{40}\,\mathrm{erg\,s}^{-1}$ (Strickland et al. 1997).

It is possible to rescue the concept of a volume-filling wind fluid being responsible for the observed X-ray luminosity if the wind has been strongly mass-loaded (i.e., additional mass has been efficiently mixed into the wind) – a theoretical model presented by S96 and subsequently explored further by Hartquist, Dyson & Williams (1997). Increasing the mass injection rate into the wind by a factor N increases the wind density by $N^{1.5}$ and the emissivity by a factor of N^{3}, as not only is there more mass in the wind but its outflow velocity is lower.

Bregman et al. (1985) used *ROSAT* HRI observations of M82 to argue that the observed X-ray surface brightness distribution was consistent with a well-collimated adiabatically expanding hot gas. However, analysis of the spectral properties of a set of regions along M82's wind using *ROSAT* PSPC data by Strickland et al. (1997) shows that the entropy of the soft X-ray-emitting gas increases with distance from the plane of the galaxy, which is inconsistent with an adiabatic outflow model.

A conservative assessment would be that X-ray observations do not strongly constrain the origin of the soft X-ray emission in galactic winds beyond that it is from a hot thermal plasma. The existing observations are broadly consistent with any of the models advanced above: shocked clouds, thermal conduction or mass-loading.

Even assessing theoretically the relative importance of processes such as mass-loading as compared to shock-heating or thermal conduction has not been possible up until now. S96 argued that M82's wind must be mass-loaded to produce the required soft X-ray luminosity and temperatures. However, their mass-loaded wind simulations did not include the interaction of the wind with the ambient ISM, which S94 had showed was capable of providing the observed X-ray luminosity.

Uncertainties in the filling factor are not the only problems affecting the interpretation of soft X-ray data on galactic winds. Understanding the temperature distribution of the X-ray-emitting gas is also an important, if relatively unexplored, theoretical aspect of galactic winds. Deriving plasma properties from X-ray spectra requires fitting a spectral model that is a good approximation to the true emission process. Failure to do so can lead to models that fit the data well but give meaningless results.

A good example of this is X-ray-derived metal abundances, where many *ROSAT* and *ASCA* studies of starburst galaxies report extremely low metal abundances, between 0.05 to 0.3 times solar (cf. Ptak 1997; Ptak et al. 1997; Read et al. 1997; Tsuru et al. 1997) for the soft thermal plasma components. We believe this to be primarily an artefact of using overly simplistic spectral models to fit the limited-quality data available from these missions. Consistent with the idea that the X-ray emission comes from a complex range of temperatures, Dahlem et al. (1998) have shown that, when using multiple hot plasma components to represent the soft thermal emission from galactic winds, most of the galaxies in their sample could be fitted using solar element abundances. Strickland & Stevens (1998), using simulated *ROSAT* PSPC observations of wind-blown bubbles (physically very similar to superbubbles and the early stages of galactic winds), show that undermodelling the X-ray spectra leads to severely underestimating the metal abundance.

Failure to correctly fit one parameter, such as the metal abundance, can also severely bias other plasma properties. For example, the derived emission measure (proportional to the density squared integrated over the volume) is approximately inversely proportional to the fitted metal abundance for gas in the temperature range $T = 10^5$ to 10^7 K. Underestimating the metal abundance then leads to overestimates of the gas density, and hence the gas mass and energy content.

In an effort to address many of the issues described above, we have performed the most detailed hydrodynamical simulations of galactic winds to date. We investigate a larger volume of model parameter space than any previous numerical study, inspired by the latest observational studies of the archetypal starburst galaxy M82. We study the variation in the properties of these galactic winds due to the starburst star formation history and intensity, the host galaxy ISM distribution, and the presence and distribution of mass-loading of the wind by dense clouds.

Our aim in this series of papers is to go beyond the previous hydrodynamical simulations of galactic winds, and to:

(i) explore in a more systematic manner the available model parameter space, focusing on M82 (the best-studied starburst with a galactic wind), using 2D hydrodynamical simulations run at high numerical resolution;

(ii) investigate several important aspects of galactic winds that are currently uncertain or have previously not been devoted much attention:

(a) the origin and filling factor of the soft X-ray-emitting gas, along with the temperature distribution of this gas;

(b) the wind energy budget and energy transport efficiency, and the degree to which the energy content can be probed by soft X-ray observations, and

(c) wind collimation. Producing the observed properties of well-collimated winds with narrow bases seems to be a problem for the simulations of TI, TB and S94, as has been pointed out by Tenorio-Tagle & Muñoz-Tuñón (1997) and Tenorio-Tagle & Muñoz-Tuñón (1998, hereafter TT);

(iii) assess the effect of finite numerical resolution and other numerical artefacts on the results of these simulations, and

(iv) directly compare the observable properties of these models (primarily concentrating on their soft X-ray emission) to the available observational data for M82 and other local starburst galaxies.

In Paper II we discuss the *observable* X-ray properties of the winds in these simulations. Focusing on artificial *ROSAT* PSPC X-ray images and spectra (the PSPC has been the best X-ray instrument for the study of superbubbles and galactic winds due to its superior sensitivity to diffuse soft thermal emission over other instruments such as the *ROSAT* HRI or the imaging spectrometers upon *ASCA*), we consider (a) the success of these models at reproducing the observed X-ray properties of M82, and (b) the extent to which such X-ray observations and standard analysis techniques can allow us to derive the true properties of the hot plasma in these outflows.

In common with the previous simulations of TI, TB, S94 and S96 we shall base our models largely on the nearby ($D = 3.63$ Mpc; Freedman et al. 1994) starburst galaxy M82. M82 is the best-studied starburst galaxy and, after NGC 253 and 1569, it is the closest starburst with a galactic wind. As the observational constraints on M82's starburst and galactic wind are the best available for any starburst galaxy, we choose to concentrate on models aiming to reproduce M82's galactic wind.

2 NUMERICAL MODELLING

The primary variables that will affect the growth and evolution of a superbubble and the eventual galactic wind in a starburst galaxy are the ISM density distribution, the strength and star formation history of the starburst, and the presence, if any, of additional interchange processes between the hot and cold phases of the ISM, such as hydrodynamical or conductive mass-loading.

As a detailed exploration of such a multidimensional parameter space for all possible galactic winds would be prohibitively expensive computationally, we choose to focus on simulations of M82's galactic wind, given that is the best-studied starburst galaxy. Our aim is to attempt to roughly bracket the range of possible ISM distributions, starburst histories and mass-loading occurring in M82, in a series of 10 simulations based on recent observational studies of this fascinating galaxy. Two further simulations explore the degree to which finite numerical resolution affects our computational results.

The majority of this section explores our choice of model parameters, preceded by information on the hydrodynamical code and analysis methods we use.

2.1 Hydrodynamic code

Our simulations of starburst-driven galactic winds have been performed using VIRGINIA HYDRODYNAMICS-I (VH-1), a high-resolution multidimensional astrophysical hydrodynamics code developed by John Blondin and co-workers (see Blondin et al. 1990; Stevens, Blondin & Pollock 1992 and Blondin 1994). VH-1 is based on the piecewise parabolic method (PPM) of Collela & Woodward (1984), a third-order accurate extension of Godunov's (1959) method.

VH-1 is a PPM with Lagrangian remap (PPMLR) code, in that as it sweeps through the multidimensional computational grid of fluid variables it remaps the fixed Eulerian grid on to a Lagrangian grid, solves the Riemann problem at the cell interfaces, and then remaps the updated fluid variables back on to the original Eulerian grid. Moving to a Lagrangian frame simplifies solving the Riemann problem, and results in a net increase in performance over PPM codes using only an Eulerian grid.

For the purposes of these simulations VH-1 is run in 2D, assuming cylindrical coordinates (r, z, ϕ) and azimuthal symmetry

around the z-axis. Radiative cooling, mass and energy injection from the starburst region, and mass deposition due to the hydrodynamical ablation of dense unresolved clouds are incorporated using standard operator splitting techniques. As in the previous simulations of TI, TB and S94, only one quadrant of the flow is calculated; symmetry in the z- and r-axes is assumed, and this determines the boundary conditions that operate along these edges of the computational grid. Material is allowed to flow in or out along the remaining two grid boundaries.

Though dependent on the exact model parameters, we have generally used a computational grid formed of a rectangular grid of 400 uniform zone along the r-axis, covering a physical region $\sim$6 kpc long, by 800 equal-sized zones along the z-axis covering $\sim$12 kpc. Simulations are run until the outermost shock of the galactic wind flows off the computational grid, typically at $t \sim$ 10–15 Myr after the start of the starburst.

2.2 Data analysis

Our results are based on the analysis of data files of the fluid variables ρ, P and $\boldsymbol{v}$ that VH-1 produces at 0.5-Myr intervals.

We make a distinction between the intrinsic properties of the wind (e.g., the 'true' gas temperatures, densities, masses, energy content and luminosities, which are described in this paper) and the observable X-ray properties (covered in the forthcoming companion paper). The observed properties need not necessarily directly reflect the true, intrinsic, wind properties due to the complications of projection, instrumental limitations and the systematic and statistical errors inherent in real observations.

We analyse only the material within the wind, i.e., swept-up disc and halo ISM along with enriched starburst ejecta. The undisturbed ISM is ignored. Quantitatively, the wind is distinguished from the undisturbed ISM by the shock that marks its outer boundary. The 2D fluid variables are converted into a 3D data set covering both poles of the wind by making use of the assumed symmetries around the z-axis and in the plane of the galaxy.

2.3 Calculation of intrinsic wind properties

The value of the fluid variables are assumed to be constant within each computational cell for the purposes of all the data analysis performed on these simulations. We do not use the parabolic interpolation used by VH-1's hydrodynamic scheme to reconstruct the variation of the fluid variables within each cell from the cell averaged values in our data analysis. Numerically summing the appropriate quantities, over those cells within the 3D data set that are within the region defined as being the galactic wind, gives the total integrated wind properties such as mass, volume, energy content and X-ray luminosity. X-ray properties such as emissivities or instrument-specific count rates are obtained assuming a mean mass per particle of 10^{-24} g and collisional ionization equilibrium, using either the MEKAL hot plasma code (Mewe, Kaastra & Liedahl 1995) or an updated version of the Raymond–Smith plasma code (Raymond & Smith 1977), along with published instrument effective areas and the Morrison & McCammon (1983) absorption coefficients.

In addition to studying the total integrated values of wind volume, mass, emission measure, and similar properties, we can investigate how these values are distributed as a function of gas temperature, density or velocity within the wind.

2.3.1 *Starburst disc and halo properties*

Many of the 'classic' starburst galaxies with clear galactic winds such as M82, NGC 253, NGC 3628 and NGC 3079 are almost edge-on, allowing the low surface brightness optical and X-ray emission from the wind to be seen above the sky background. Had these galaxies been face-on (e.g., the starburst galaxy M83), it would have been much more difficult to distinguish emission from the wind from the X-ray and optically bright discs of these galaxies.

Previous simulations such as TB and S94 have considered only the total properties of galactic winds integrated over the entire volume of the outflow. We feel it is important to distinguish between the properties of the gas associated with the galactic wind within the disc of the host galaxy, and the gas clearly above the disc (in what would be observationally identified as the wind in an edge-on starburst). A more ambitious study might divide the wind up into several different sections, as done in Strickland et al. (1997), but for now we will consider only two separate regions: disc or halo.

The same techniques of analysis used on the entire wind described above are applied to gas within the plane or disc of the galaxy (defined as being the region with $|z| \leq 1.5$ kpc) and gas above the plane in the halo ($|z| > 1.5$ kpc). This allows us to study the spatial variation of the wind properties in a simple but meaningful manner.

2.4 ISM distribution and gravitational potential

We adopt the philosophy of TB and S94 in setting up an initial ISM distribution of a cool disc and hot halo, in rotating hydrostatic equilibrium under the applied gravitational field. Although the ISM in starburst galaxies is not static or in equilibrium, we choose a static solution to prevent the dynamics of an arbitrary non-static ISM distribution from affecting the wind dynamics.

The ISM modelled in these 2D numerical simulations and in TI, TB and S94 is essentially a single-phase volume-filling gas. Although in reality the ISM of late-type galaxies is clearly multiphase, we make the assumption that the most important phase, with respect to the ISM's interaction with the starburst-driven wind, is that ISM component that occupies the majority of the volume. In the disc this might be cool $\sim 10^4$ K gas and coronal gas in the halo. Mass-loaded simulations such as S96 treat the interaction of the wind with dense, low volume-filling factor clouds. Although the majority of the mass in the ISM is in molecular clouds, these occupy only a small fraction of the total volume, even within a starburst region such as the centre of M82. Lugten et al. (1986) find that the molecular gas within the nuclear region of M82 is comprised of small clouds, thin filaments or sheets with a total volume-filling factor $\eta \sim 10^{-3}$.

To investigate the effect of the ISM on the collimation and confinement of the wind, and how this alters the observable X-ray properties of the galactic wind, we study two different ISM distributions. We adopt TB's ISM distribution as representative of a thick disc with dense cool gas high above the plane of the galaxy, which provides substantial wind collimation. The gravitational potentials used by TB and S94 do not reproduce M82's observed rotation curve, as can be seen in Fig. 1. The maximal rotational velocity in TB and S94's models is a factor of 2 lower than that observed in M82. Consequently, with less enclosed mass, the gravitational force felt by the wind in S94 and TB's

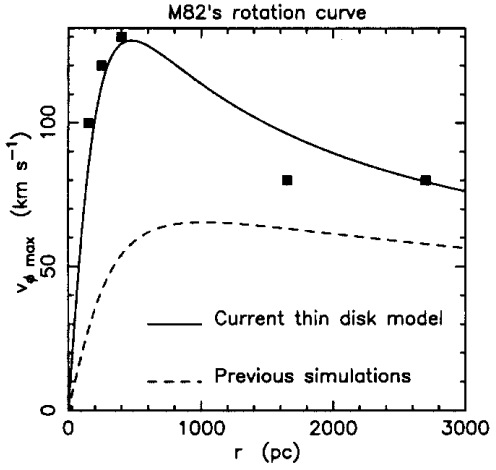

Figure 1. M82's rotation curve (filled squares, from Götz et al. 1990) compared to the rotation curves $v(r) = (r\partial\Phi_{\rm tot}/\partial r)^{1/2}$, resulting from the mass distributions assumed in our thin-disc models and the simulations of Tomisaka & Ikeuchi (1988), Tomisaka & Bregman (1993) and Suchkov et al. (1994).

simulations is too low. For our thin-disc model we remedy this by adding the potential due to a Miyamoto & Nagai (1975) disc to the stellar spheroid used in TB. The resulting disc using this combined potential is significantly thinner than that of TB.

The large-scale ISM distribution in M82 is very poorly known, and the majority of investigations into the ISM in M82 have focused on the wind or the conditions deep within the starburst region. The current ISM distribution in M82 may not be representative of the initial ISM distribution prevailing at the time of the birth of the starburst. We do not claim that these ISM distributions used in our simulations correspond to the true ISM in a starburst galaxy such as M82, but they capture the essential features which we wish to investigate, namely the effect of collimation on the wind dynamics and the resulting X-ray emission.

The initial static ISM distribution is computed as a solution to the steady-state momentum equation

$$(\boldsymbol{v}\cdot\nabla)\boldsymbol{v} = -\frac{1}{\rho}\nabla P - \nabla\Phi_{\rm tot}, \tag{1}$$

where $\boldsymbol{v}$, ρ, P and $\Phi_{\rm tot}$ are the gas velocity, density, pressure and total gravitational potential respectively.

We assume that the ISM is supported predominantly by rotation in the plane of the galaxy, so the rotational velocity v_ϕ (i.e., the azimuthal component of velocity) in the plane of the galaxy is given by

$$v_\phi(r) = e_{\rm rot}\left(r\frac{\partial\Phi_{\rm tot}}{\partial r}\right)^{1/2}. \tag{2}$$

If the disc were entirely supported by rotation, then $e_{\rm rot} = 1$. In these simulations a small fraction of the gravitational force in the plane is supported by the turbulent and thermal pressure of the ISM. For the thick disc we choose $e_{\rm rot} = 0.9$, and for the thin disc $e_{\rm rot} = 0.95$.

To reduce the rotational velocity of the gas above the plane (as seen in NGC 891 by Swaters, Sancisi & van der Hulst 1997 for example), and to have a non-rotating galactic halo, we assume a simple model where the rotational support (and hence v_ϕ) drops off exponentially with increasing height z above the plane of the galaxy

$$e = e_{\rm rot}\exp(-z/z_{\rm rot}), \tag{3}$$

where the scaleheight for this reduction in rotational velocity $z_{\rm rot} = 5\,$kpc, as used in TB.

In 2D numerical simulations such as these, which assume cylindrical symmetry around the z-axis (i.e., azimuthally symmetric), only the r and z components of the fluid variables ρ, P and $\boldsymbol{v}$ are calculated. Rotational motion is simulated by solving a modified form of equation (1):

$$-\frac{1}{\rho}\nabla P - \nabla\Phi_{\rm eff} = 0, \tag{4}$$

where $\Phi_{\rm eff}$ is the effective potential, the sum of the true gravitational potential and the centrifugal potential arising from the incorporation of the rotational motions. Similarly, the force required to hold the disc in equilibrium against the pressure gradient in these 2D simulations is not just the true gravitational force $\boldsymbol{g} = -\nabla\Phi_{\rm tot}$, but rather the effective gravitational force $\boldsymbol{g}_{\rm eff} = -\nabla\Phi_{\rm eff}$.

The gravitational potential used in our thick-disc model is identical to that used by TB, a single spherically symmetric component identified with the central stellar spheroid. Note that there are typographical errors in equations (2), (3), (4) and (7) of TB, so the equations presented here differ from those presented in TB.

We use a King model to describe the stellar spheroid,

$$\rho_{\rm ss}(\omega) = \frac{\rho_0}{[1+(\omega/\omega_0)^2]^{3/2}}, \tag{5}$$

where $\rho_{\rm ss}(\omega)$ is the stellar density as a function of the radial distance from the centre ω, ρ_0 is the central density, and ω_0 is the core radius. The gravitational potential $\Phi_{\rm ss}$ due to this stellar spheroid is then

$$\Phi_{\rm ss}(\omega) = -\frac{GM_{\rm ss}}{\omega_0}\left\{\frac{\ln\left[(\omega/\omega_0)+\sqrt{1+(\omega/\omega_0)^2}\right]}{\omega/\omega_0}\right\}, \tag{6}$$

where $\omega = \sqrt{r^2+z^2}$ is the distance from the nucleus, and we define $M_{\rm ss} = 4\pi\rho_{\rm ss}\omega_0^3$. Following TB, we choose $M_{\rm ss} = 1.2\times10^9\,{\rm M}_\odot$ and $\omega_0 = 350\,$pc.

For the thin-disc model we retain a King model to represent the central stellar spheroid, and use a Miyamoto & Nagai (1975) disc potential to represent the disc of the galaxy,

$$\Phi_{\rm disc}(\omega) = -\frac{GM_{\rm disc}}{\sqrt{r^2+(a+\sqrt{z^2+b^2})^2}}, \tag{7}$$

where a and b are the radial and vertical scale sizes of the disc. The total potential in the thin-disc model is $\Phi_{\rm tot} = \Phi_{\rm ss} + \Phi_{\rm disc}$. To approximately reproduce M82's rotation curve (Fig. 1), we use $M_{\rm ss} = 2\times10^8\,{\rm M}_\odot$, $\omega_0 = 350\,$pc, $M_{\rm disc} = 2\times10^9\,{\rm M}_\odot$, $a = 222\,$pc and $b = 75\,$pc.

We do not incorporate an additional massive dark matter halo component into the current set of simulations, as M82's rotation curve is well described by the chosen stellar spheroid plus Miyamoto & Nagai disc model. We are primarily interested in the behaviour of the winds over the initial ~20 Myr of the starburst, a period during which the gravitational effects of any dark matter halo will be negligible. Dark matter haloes may shape the long-term behaviour of material in weak winds (e.g., the 2D

simulations of winds in dwarf galaxies by Mac Low & Ferrara 1999), and the fate of slowly moving gas dragged out of the disc in starburst-driven winds like M82. These simulations are not designed to investigate the long-term fate of this gas, but rather the dynamics and properties of the gas in the observed galactic winds which have dynamical ages of $\sim 10^7$ yr.

In common with TB, we incorporate a disc ISM of central density $n_{\rm disc,0} = 20\,{\rm cm}^{-3}$ and a tenuous halo of central density $n_{\rm halo,0} = 2 \times 10^{-3}\,{\rm cm}^{-3}$ in both models. The initial ISM density and pressure is then given by

$$\rho_{\rm disc}(r,z) = \rho_{\rm disc,0} \times \exp\left[-\frac{\Phi_{\rm tot}(r,z) - e^2\Phi_{\rm tot}(r,0) - (1-e^2)\Phi_{\rm tot}(0,0)}{c^2_{\rm s,disc}}\right], \quad (8)$$

$$\rho_{\rm halo}(r,z) = \rho_{\rm halo,0} \times \exp\left[-\frac{\Phi_{\rm tot}(r,z) - e^2\Phi_{\rm tot}(r,0) - (1-e^2)\Phi_{\rm tot}(0,0)}{c^2_{\rm s,halo}}\right], \quad (9)$$

$$\rho(r,z) = \rho_{\rm disc}(r,z) + \rho_{\rm halo}(r,z), \quad (10)$$

and

$$P(r,z) = \rho_{\rm disc}(r,z)c^2_{\rm s,disc} + \rho_{\rm halo}(r,z)c^2_{\rm s,halo}, \quad (11)$$

where e quantifies the fraction of rotational support of the ISM as given in equation (3), and $c_{\rm s,disc}$ and $c_{\rm s,halo}$ are the sound speeds in the disc and halo respectively. The complexity of equations (8) and (9) is due to incorporating rotational support through an effective potential. Without the centrifugal potential, these equations would be of the form $\rho = \rho_0 \exp\{-[\Phi_{\rm tot}(r,z) - \Phi_{\rm tot}(0,0)]/c^2_{\rm s}\}$.

Radio recombination line tracing gas in H II regions within the starburst region by Seaquist et al. (1996) implies that the density of thermal electrons with $T_{\rm e} = 10^4$ K is between 10 and $100\,{\rm cm}^{-3}$. Bear in mind that observational evidence from a wide range of sources suggests that the ISM within the starburst region is extremely non-uniform, from dense molecular clouds to very hot coronal gas. The disc ISM in these models is chosen to represent one phase of this multiphase ISM, the phase which presents the starburst-driven wind with the greatest physical opposition, i.e., the phase which has the greatest volume-filling factor. Dense clouds which are enveloped and overrun by the wind can be represented within these simulations, though not resolved by the computational grid, by mass-loading as discussed in Section 2.7.

In place of our ignorance of the properties of the haloes galactic winds expand into, we envision a hot tenuous halo enveloping M82. As star formation rates in M82 appear to have been elevated since the nearest encounter with its neighbour M81 approximately 200 Myr ago (Cottrell 1997), chimneys above OB associations, a galactic fountain, or even previous galactic winds all could have created such a hot halo.

As the complex 3D, multiphase, turbulent structure of the ISM can not be treated in these simulations, we follow the lead of TI, TB and S94 in increasing the isothermal sound speed of the disc gas to simulate the turbulent pressure support seen in real discs (e.g. Norman & Ferrara 1996). Without this increased pressure the resulting discs are extremely thin. Following TB, we set $c_{\rm s,disc} = 30\,{\rm km\,s}^{-1}$ and $c_{\rm s,halo} = 300\,{\rm km\,s}^{-1}$ in both thick- and thin-disc models. This corresponds roughly to a disc temperature of $T_{\rm disc} = 6.5 \times 10^4$ K and a halo temperature of $T_{\rm halo} = 6.5 \times 10^6$ K.

This imposes a minimum allowed temperature of $T_{\rm disc}$ on the gas in these simulations, so we can not directly treat the cooler $T \sim 10^4$ K gas that is responsible for the optical emission lines in galactic winds. Currently, we make only qualitative comparisons between the dynamics of the coolest gas in our simulations and the cool gas seen in M82 the winds of and other starburst galaxies. This minimum temperature does not affect the dynamics and emission properties of X-ray-emitting gas that we are primarily interested in.

2.5 Starburst history and mass and energy injection rates

The actual star formation history in M82 is only crudely known. The high optical extinction towards the nucleus and edge-on inclination make it difficult to investigate the properties of stars or star clusters in the starburst nucleus, except by using infrared observations. Even in relatively nearby and unobscured dwarf starburst galaxies such as NGC 1569 and NGC 5253, the history of all but the most recent star formation is a subject of debate (see Calzetti et al. 1997 with reference to NGC 5253, or González Delgado et al. 1997 for NGC 1569).

As we are interested in the effect of the star formation history on the wind dynamics and observable X-ray properties, we shall explore a few simple star formation histories. These are motivated by the near-infrared spectroscopic study of individual stellar clusters in M82's starburst nucleus by Satyapal et al. (1997), dynamical arguments concerning the total mass of stars formed in the starburst by McLeod et al. (1993), and radio estimates of the current SN rate by Muxlow et al. (1994) and Allen & Kronberg (1998). We briefly review what these observations can tell us about the total mass of stars formed in M82's current starburst, and its star formation history.

2.5.1 Infrared observations of individual super star clusters

Satyapal et al. (1997) use dereddened Brγ and CO band imaging to study 12 unresolved stellar clusters within $r = 270$ pc of the nucleus. By comparison with instantaneous starburst models (appropriate for individual clusters), they used the CO indices and Brγ equivalent widths of the individual clusters to estimate the cluster ages, and the ionizing photon fluxes from the extinction-corrected Brγ line flux.

We used this information, along with the instantaneous starburst evolutionary synthesis models of Leitherer & Heckman (1995, hereafter LH95), to estimate the initial clusters masses assuming a Salpeter (1955) IMF extending between 1 and $100\,{\rm M}_\odot$.

Note that the ages of individual clusters differ between the two age estimators, with ages based on the CO index generally being a few Myr older than those based on the Brγ equivalent widths. Ages inferred from the CO index were in the range 5–10 Myr, while those from W(Brγ) lay in the range 4–8 Myr. The relative ages of the different clusters are also inconsistent between the two methods.

For a given ionizing photon flux the initial cluster mass is a sensitive function of the assumed age, due to the rapid evolution of the extremely luminous stars at the high end of the IMF. Hence the uncertainty in cluster ages leads to a large uncertainty in the mass of stars formed in the starburst.

The W(Brγ)-derived ages and ionizing photon fluxes yield a total initial mass of stars formed in the starburst of $M_{\rm SB} \sim 8 \times 10^6\,{\rm M}_\odot$. From the LH95 models the peak SN rate associated with these stars is $\sim 8 \times 10^{-3}\,{\rm SN\,yr}^{-1}$.

Using the CO index instead to derive the cluster ages yields

$M_{SB} \sim 1.3 \times 10^8\,M_\odot$, with a peak SN rate of $\sim 0.13\,SN\,yr^{-1}$. If the IMF extends down to $M_{low} = 0.1\,M_\odot$, then the total mass $M_{SB} \sim 3 \times 10^8\,M_\odot$, in agreement with the value of $M_{SB} \sim 2.5 \times 10^8\,M_\odot$ quoted in Satyapal et al. (1997). This is ~40 per cent of the total dynamical mass within the starburst region.

2.5.2 *Dynamical limits on the total mass of stars formed*

McLeod et al. (1993) present a simple dynamical argument that places an upper limit of the total mass of stars formed in M82's starburst of $\lesssim 2.5 \times 10^8\,M_\odot$. The total dynamical mass within 500 pc is $M_{tot} \approx 7 \times 10^8\,M_\odot$, of which approximately $10^8\,M_\odot$ is gas. Only a fraction of the remaining mass can be due to stars formed in the current starburst activity, as there must have been a pre-existing stellar population. McLeod et al.'s argument is based on the following scenario for the triggering of M82's starburst: The starburst was probably triggered by a close interaction of M82 with M81 approximately 200 Myr ago (Cottrell 1977), which lead to gas losing angular momentum and falling into the nucleus over a time-scale of ~100 Myr. Eventually, self-gravity within the gas will trigger the strong burst of star formation. Self-gravitation in the ISM will have become important before the gas mass equals the mass of pre-existing stars within the nucleus, so it is unlikely that the total mass of gas and stars formed in the starburst exceeds half the current dynamical mass within the starburst region.

This upper limit of $2.5 \times 10^8\,M_\odot$ is very similar to Satyapal et al.'s (1997) estimate of the starburst mass assuming conservatively a Salpeter IMF extending between 0.1–100 $M_\odot$, where very low-mass stars consume most of the mass. If we assume a top-heavy IMF (i.e., biased against low-mass stars) we can get a very powerful starburst that consumes only a small amount of gas, but would violate observational constraints on the starburst luminosity.

2.5.3 *The current SN rate*

Radio observations of the 50 or so supernova remnants (SNRs) within the central kiloparsec of M82 can be used to estimate the current (i.e., within the last several thousand years) SN rate. As a simple rule of thumb, the SN rate between $t \sim 3$ and 40 Myr for an instantaneous burst forming $10^6\,M_\odot$ of stars is $\sim 10^{-3}\,yr^{-1}$ (using the LH95 models and assuming a Salpeter IMF between $M_{low} = 1$ and $M_{up} = 100\,M_\odot$).

Muxlow et al. (1994) estimate a SN rate of $0.05\,yr^{-1}$, assuming that the SNRs are still freely expanding at $v = 5000\,km\,s^{-1}$. If the SNRs are not in free expansion, the SN rate should be reduced. This SN rate corresponds to a total starburst mass of $\sim 5 \times 10^7\,M_\odot$.

Based on the oldest and largest SNR in M82, Allen & Kronberg (1998) estimate the SN rate to be $\gtrsim 0.016\,yr^{-1}$. This is a lower limit as other large (and hence faint) SNRs may be missing from current SNR surveys.

Note that the current SN rate is not particularly sensitive to the star formation history, as the SN rate for an instantaneous burst of stars is approximately constant between ~3 and ~40 Myr.

2.5.4 *Starburst models used in these simulations*

The observational evidence considered above suggests that although the exact star formation history and mass in M82 may not be accurately known, it is possible to bracket the true solution.

We assume solar metal abundances and a Salpeter IMF between 1 and 100 $M_\odot$ in all these mass estimates below. This is purely for convenience as the LH95 models assume this IMF. All the other mass estimates have been converted to this IMF.

The total mass of the starburst clusters inferred from Satyapal et al.'s (1997) Brγ equivalent widths, $M_{tot} \sim 8 \times 10^6\,M_\odot$, and Allen & Kronberg's (1998) lower limit on the SN rate, $M_{tot} \gtrsim 1.6 \times 10^7\,M_\odot$, suggest a lower limit on the starburst mass of $M_{tot} \sim 10^7\,M_\odot$.

The dynamical arguments of McLeod et al. (1993) suggest an upper limit on the total mass recently converted into stars in M82 centre of $M_{tot} \lesssim 10^8\,M_\odot$, consistent with the mass inferred by Satyapal of $M_{tot} \sim 10^8\,M_\odot$ based on the CO index-derived ages. The recent SN rate inferred by Muxlow et al. (1994) implies a starburst mass of $M_{tot} \sim 5 \times 10^7\,M_\odot$.

The ages inferred from Satyapal et al.'s (1997) CO indices and W(Brγ), though marginally inconsistent with each other, suggest a spread in ages for the bright clusters of between 4 and 10 Myr old.

We choose three simple SF histories to explore the effects of M82's possible SF history on the dynamics and X-ray emission from the galactic wind (see Fig. 2).

(i) A single instantaneous starburst (SIB) of total mass $M_{tot} = 10^8\,M_\odot$. This model can be considered as the most powerful starburst consistent with the observational constraints.

(ii) A weaker single instantaneous starburst (SIB) of total mass $M_{tot} = 10^7\,M_\odot$, consistent with the least powerful starburst suggested observationally.

(iii) A starburst of total mass $M_{tot} = 10^8\,M_\odot$, but with a slightly more complex SF history (CSF) spread over a period of 10 Myr

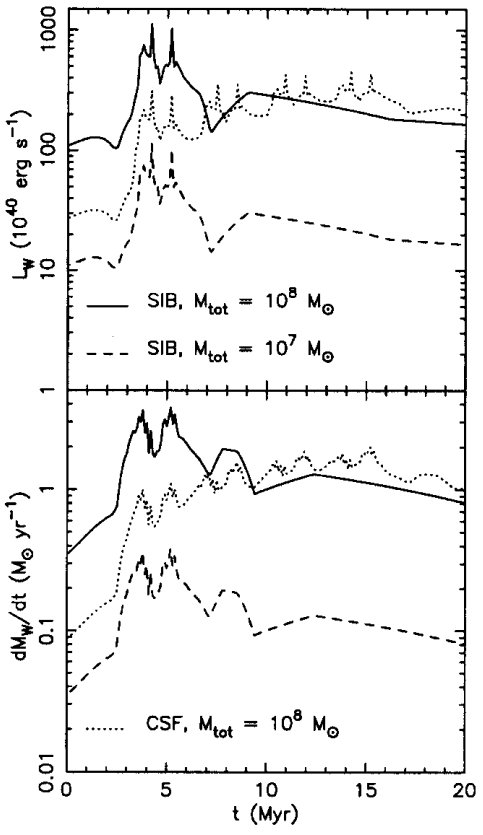

Figure 2. Starburst energy injection (top panel) and mass injection (bottom panel) rates adopted in these simulations (see Section 2.5).

rather than an SIB. With the same total mass as the power SIB, this model allows us to investigate the effect of a more gradual mass and energy injection history.

2.5.5 *Energy thermalization efficiency*

We assume that 100 per cent of the mechanical power from stellar winds and SNe is available to power the wind, i.e., the immediate radiative energy losses within the starburst region are negligible. The value of this 'thermalization efficiency' is by no means well understood either observationally or theoretically, and will depend on the specific environment (for example, whether the SN goes off in or near a molecular cloud or in a pre-existing low-density cavity).

Thornton et al. (1998) perform a parameter study to assess the radiative losses of SNRs expanding into uniform media of different densities. For an SNR of age 10^5 yr (a sufficient time for any SNR in a nuclear starburst region to have interacted or merged with neighbouring SNRs) radiative losses range from negligible (ISM number densities $\sim 10^{-2}\,\mathrm{cm}^{-3}$) to $\geq$90 per cent (number densities $\sim 10\,\mathrm{cm}^{-3}$) of the initial supernova energy.

Although the majority of the mass of the ISM in a starburst region is in dense molecular clouds, these occupy only a small fraction of the total volume ($\sim 10^{-3}$; see Lugten et al. 1986) within a starburst region such as the centre of M82. Hence on average young SNRs in M82 will interact with tenuous gas, with reasonably low radiative losses.

Observations of the properties of local starburst driven winds already strongly argue for high thermalization efficiencies. From a theoretical basis, Chevalier & Clegg (1985) explicitly state that the requirement to drive a galactic wind is a high thermalization efficiency. Two simple arguments based on M82's wind will suffice. For the purposes of the following arguments alone, we shall assume a very simple model for the starburst of 0.1 SNe yr^{-1} for 10^7 yr. This gives a total mechanical energy injection of $E = 10^{57}$ erg and an average mechanical power of $\dot{E} = 3 \times 10^{42}\,\mathrm{erg\,s}^{-1}$ (assuming 100 per cent thermalization).

(i) The thermal energy of the $T \sim 5 \times 10^6$ K gas is $\sim 3 \times 10^{56}\,\eta^{1/2}$ erg (Strickland et al. 1997, where η is the volume-filling factor of the X-ray-emitting gas). Hence to first order the thermal energy content of the wind is $\sim$30 per cent of the total energy released by SNe and stellar winds. If we instead assume that the X-ray emission comes from shocked clouds of low filling factor (cf. Chevalier & Clegg 1985), then the total energy of the wind may be even greater, as the remainder of the volume must be occupied by tenuous but energetic gas. This estimate does not include the kinetic energy of the wind, which we shall show later to larger than the thermal energy content of the wind.

(ii) The soft X-ray luminosity of the hot gas in M82 is $L_\mathrm{X} = 2 \times 10^{40}\,\mathrm{erg\,s}^{-1}$ (Strickland et al. 1997; Dahlem et al. 1998) in the *ROSAT* band. If the thermalization efficiencies were as low as the $\sim$3 per cent value argued by Bradamante et al. (1998), then galactic winds must extremely efficient at radiating X-rays. This is inconsistent with the estimated X-ray-emitting gas cooling times (cf. Read et al. 1997), and it would be extremely difficult to drive a wind at all, given such strong radiative losses.

For galactic winds the immediate thermalization efficiency within the starburst region must then be reasonably high, i.e., between 10 and 100 per cent. We therefore follow the lead of previous simulations of galactic winds and assume that 100 per cent of the mechanical energy from SNe and stellar winds can be used to drive the wind.

2.5.6 *The starburst region*

At each computational time-step we inject the appropriate amount of mass and energy uniformly within the computational cells corresponding to the starburst region.

For the thin-disc model the chosen starburst region is a cylinder 150 pc in radius, extending to a height of 30 pc above and below the plane of the galaxy. This corresponds to 10×2 computational cells in the quadrant of the flow actually modelled (the other three quadrants are by symmetry identical to the one calculated in the simulations).

For the thick-disc model we use a spherical starburst region of radius 150 pc. As the scaleheight of the ISM above the starburst region is greater than 150 pc, this does not constitute a significant difference between the thick- and thin-disc models. We did perform an additional simulation with the thin-disc model with a spherical starburst region, and confirmed that the dynamics and properties were almost identical to those in the default cylindrical starburst region models.

As discussed in Strickland & Stevens (1999), the picture of energy and mass being injected uniformly into a starburst region, and driving a single wind and bubble into the ISM, is overly simplistic. Individual super star clusters (Meurer et al. 1995; O'Connell et al. 1995) blow strong winds into the surrounding starburst region, which interact with the complex ISM structure of molecular clouds, SNRs and winds from other massive stars and clusters. The inferred ages of the star clusters in NGC 5253 (Gorjian 1996; Calzetti et al. 1997) and M82 (Satyapal et al. 1997) suggest that the formation of massive star clusters propagates across or outwards through the starburst region. Sadly, simulating such detail requires computational resources far in excess of what is currently available.

2.6 Metallicity and radiative cooling

For the purposes of calculating the radiative cooling of the gas in the simulations, as well as calculating the X-ray emission, we assume solar metallicity and collisional ionization equilibrium.

The metallicity of the cool ambient ISM and the hot gas in M82 is uncertain. Optical or infrared observations suggest a metal abundance similar to solar, while X-ray observations of the hot gas give an abundance of less than one third of the solar value.

Measurements of infrared fine-structure lines (Puxley et al. 1989) show that the abundances of argon and neon in M82's ISM are $Z = 1.0 \pm 0.5\,\mathrm{Z}_\odot$. O'Connell & Mangano (1978) find optical emission-line ratios typical of H II regions with metallicity similar to or slightly higher than solar.

In principle, X-ray observations could directly measure the metal abundance in the hot gas responsible for the observed soft thermal X-ray emission. X-ray-determined metal abundances of the hot gas in starburst galaxies (including M82) using *ROSAT* and *ASCA* generally give low abundances $Z \lesssim 0.3\,\mathrm{Z}_\odot$ (cf. Ptak 1997), with the iron abundance depressed relative to the α-process elemental abundances (the *ROSAT* PSPC is sensitive only to the iron abundance through the strong Fe-L complex at $E \sim 0.8$ keV). This may just be an artefact of using overly simplistic spectral models to fit X-ray spectra arising from multiphase hot gas (see Dahlem et al. 1998 for observational evidence for this argument, or Strickland & Stevens 1998 for supporting theoretical modelling).

We use a parametrized form of the total emissivities for gas in the temperature range $10^{4.5}$–$10^{8.5}$ K from a recent version of the

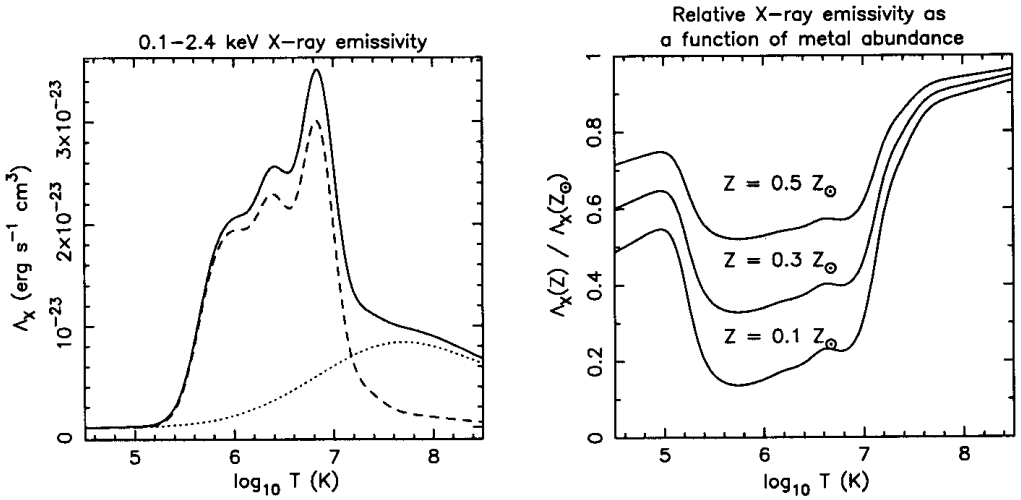

Figure 3. X-ray emissivity Λ_X in the 0.1–2.4 keV band as a function of temperature and metal abundance, assuming solar abundance ratios and collisional ionization equilibrium. (Left) The total X-ray emissivity from the Raymond–Smith hot plasma code (Raymond & Smith 1977) for solar metallicity (solid line), decomposed into the contribution from H and He only (dotted line) and metal ions (dashed line). (Right) The soft X-ray emissivity for a hot plasma of metal abundance $Z = 0.1$, 0.3 and $0.5\,Z_\odot$, relative to the emissivity of a solar-metallicity hot plasma. For temperatures between 3×10^5 and 10^7 K line emission from metals dominates the emission. X-ray emission from low-metallicity hot plasmas is significantly depressed in this temperature range due to the lack of line emission.

Raymond & Smith (1977) hot-plasma code to implement radiative cooling in VH-1. The temperature is updated each computational time-step using a fully implicit scheme as described by Strickland & Blondin (1995). Gas is prevented from cooling below $T = T_{\rm disc} = 6.5\times10^4$ K to prevent the artificially hot disc from cooling and collapsing.

We restrict the cooling rate at unresolved interfaces between hot diffuse gas and cold dense gas, as the finite width of sharp features on the computational grid can lead to anomalously high cooling rates. At any unresolved density gradients we use the minimum volume cooling rate in the immediate vicinity, a similar scheme to that used by Stone & Norman (1993).

The total cooling rate and X-ray emissivity of a hot gas in the temperature range 3×10^5–10^7 K is a strong function of its metal abundance, as shown in Fig. 3. Hence different explanations for the origin of the soft X-ray emission in galactic winds also imply that we expect different metal abundances for this gas and hence differing emissivities for given density and temperature. For example, S94 argue that the majority of the X-ray emission from starburst driven winds is due to shocked disc material, which would have significantly lower metal abundance than the SN-enriched starburst ejecta. The metallicity of the gas in the wind will strongly affect its cooling rate and X-ray luminosity. This is unlikely to affect the dynamics of the X-ray-emitting gas, as it is an inefficient radiator of its thermal energy. The main effect of the assumed metallicity on the X-ray properties will be on the absolute normalization of the X-ray luminosity, detector count rates and X-ray surface brightness from our simulations.

In the absence of more conclusive observational estimates of the metal abundance of the ISM in M82, we shall assume all the gas in these simulations is of solar abundance. In paper II we shall investigate any biases in X-ray-determined metallicities of the hot gas in galactic winds, by producing and analysing artificial X-ray observations from the multiphase gas distributions in these simulations.

2.7 Mass-loading

A starburst-driven wind, in its expansion through the ISM as a superbubble and post-blowout as a galactic wind, will overrun and envelop clumps and clouds that are denser than the ambient ISM. Once inside the bubble or wind, conductive, hydrodynamical or even photo-evaporative processes in the shocked or free wind regions will evaporate, ablate and shock-heat these clouds. This will add cool material into the hot X-ray-emitting regions, and hence potentially alter the energetics and observational properties of the wind. This addition of mass into the flow is termed 'mass-loading' (Hartquist et al. 1986). Unlike the interaction of the wind with the ambient, intercloud, medium, which adds mass to the outside of the superbubble/wind, mass-loading from clouds adds material gradually into the hot interior.

Conductive mass-loading is the evaporation of clouds by the thermal conduction of hot electrons from the hot plasma penetrating and heating the clouds (cf. Cowie, McKee & Ostriker 1981). Hydrodynamical mass-loading is the ablation and physical destruction of clouds by hydrodynamical processes as the hot plasma flows past dense clouds, either subsonically or supersonically (Hartquist et al. 1986). Our models do not incorporate thermal conduction, so we concentrate on a hydrodynamically mass-loaded model. Although the physics of the two processes are quite different, our simple model captures the essential feature of mass-loading, which is the addition of additional cold material into the hot interior of the flow. Our aim is to study the effects of a simple but physically motivated model of the interaction of the wind with dense clouds.

A dense cloud embedded in a subsonic flow will experience pressure differences along its surface that lead to it expanding perpendicularly to the direction of the surrounding flow (the head of the cloud experiences the ram pressure plus the thermal pressure of the tenuous flow, whereas the sides of the cloud only experience the thermal pressure of the surrounding flow). Rayleigh–Taylor (RT) and Kelvin–Helmholtz (KH) instabilities will remove material from the perimeter of the expanding cloud. The ablation rate of the cloud (i.e., its mass-loading rate) is proportional to the expansion speed of the cloud divided by the size of the mixing region between the cloud and the wind.

Dense clouds embedded in supersonic flows are crushed by

shocks driven into them by the wind, before being disrupted by pressure differences in a similar manner to clouds in subsonic flows.

Physical arguments based on the picture given above (Hartquist et al. 1986; see Arthur & Henney 1996 for a numerical treatment of mass-loaded SNRs) suggest that the mass-loading rate $\dot{q}$ of a flow that ablates small, denser clouds depends on the Mach number $\mathcal{M}$ of the upstream flow for subsonic flows, but not for supersonic flows which are ablated at a maximum mass-loading rate Q, i.e.,

$$\dot{q} = \begin{cases} Q \times \mathcal{M}^{4/3} & \text{if } \mathcal{M} < 1.0 \\ Q & \text{if } \mathcal{M} \geq 1.0. \end{cases} \quad (12)$$

In practice, the maximum mass-loading rate Q depends on both the properties of the cloud and the flow density and velocity. The maximum mass-loading rate per unit volume over the cloud is

$$Q = a\left(\frac{\rho_{\rm w} v_{\rm w} k T_{\rm cl} \rho_{\rm cl}^2}{\mu m_{\rm H} R_{\rm cl}^3}\right)^{1/3}, \quad (13)$$

where a is a constant of order unity, $\rho_{\rm w}$ and $v_{\rm w}$ are the density and velocity of the flow the cloud is embedded in, and $T_{\rm cl}$, $\rho_{\rm cl}$ and $R_{\rm cl}$ are the cloud temperature, density and radius.

Despite the simplicity of this analytical treatment, numerical simulations of clouds ablated by tenuous flows (Klein, McKee & Collela 1994) support this model of mass-loading. For the purposes of these simulations we shall consider two different models of mass-loading of a starburst-driven galactic wind, based loosely on the central and distributed mass-loading models used by S96.

2.7.1 *Central mass-loading*

S96's steady-state mass-loaded wind models (with no ISM apart from the clouds) suggested that all mass-loading in M82 was confined to the starburst region itself. Given the observed molecular ring at a radius of $\sim$250 pc from the centre, and that large masses of molecular material must have existed within the starburst region to form the young stars, it is not unreasonable to expect the majority of cloud material to exist within the starburst region.

As in S96's model we simulate this central mass-loading by ignoring the detailed cloud mass-loading rates given above, and increasing the mass deposition rate in the starburst by a factor of 5. This results in a typical mass injection rate of $\sim 5\,{\rm M}_\odot\,{\rm yr}^{-1}$, similar to the models S96 considered most successful.

2.7.2 *Distributed mass-loading*

The alternative to a central reservoir of cloud material is clouds distributed throughout the disc of the galaxy. We assume that all clouds have the same density, size and temperature, irrespective of their position within the galaxy. As these clouds are destroyed by the wind, these properties do not alter, but only the total mass in clouds is reduced. The only cloud property we allow to vary with spatial position over the disc is the local cloud volume-filling factor, which then controls the local mass in clouds. This cloud filling factor is assumed to remain constant with time, the total mass in clouds reducing with time as the wind overruns them and destroys them.

The maximum mass-loading rate Q is a relatively weak function of the wind and cloud properties (as can be seen in equation 13). Rather than explicitly calculate Q as a function of the local flow variables at every computational cell and time-step, we fix this maximum mass-loading rate over the entire grid. This allows us to explicitly control the minimum cloud destruction time-scale

$$\tau_{\rm cl} = \rho_{\rm cl}/Q, \quad (14)$$

where $\rho_{\rm cl}$ is the density within a cloud.

We choose Q and $n_{\rm cl}$ to give a minimum cloud destruction time-scale that is scientifically interesting. If the cloud destruction time-scale $\tau_{\rm cl} \ll \tau_{\rm dyn}$ (where $\tau_{\rm dyn} \sim 10$ Myr is the dynamical age scale of the galactic wind), then clouds will be destroyed almost instantaneously by the outer shock of the wind. All the cloud mass will be added to the outermost part of the wind, and the mass-loading will be almost identical to the evolution of a wind in a slightly denser medium. If $\tau_{\rm cl} \gg \tau_{\rm dyn}$, then almost no mass-loading will occur. Hence the case of $\tau_{\rm cl} \sim \tau_{\rm dyn}$ is the most interesting as far as the effects of mass-loading on the properties of galactic winds are concerned. We therefore set $\tau_{\rm cl} = 10$ Myr.

We assume that the clouds are distributed identically to the high filling factor ambient ISM, in rotating hydrostatic equilibrium. All clouds are assumed to have number density $n_{\rm cl} = 10^3\,{\rm cm}^{-3}$ and temperature $T_{\rm cl} = 10^3$ K, and apart from the assumed rotational motion, are at rest with respect to the starburst region. The total mass in clouds is almost identical in the thick- and thin-disc models, with a central cloud filling factor of $\eta_{\rm cl} = 4 \times 10^{-2}$ in the thin-disc models and $\eta_{\rm cl} = 1.3 \times 10^{-2}$ in the thick-disc models. The original mass of cloud material within the central 500 pc is $\sim 3 \times 10^7\,{\rm M}_\odot$, and within the volume occupied by the entire galactic wind at an age $t \sim 15$ Myr the original cloud mass is $\sim 3 \times 10^8\,{\rm M}_\odot$. As the minimum cloud destruction time is $\tau_{\rm cl} = 10$ Myr, not all of this cloud mass will have been added into the flow.

At each computational step we calculate the local Mach number $\mathcal{M}$ and calculate the cloud mass-loading rate $\dot{q}$ from equation (12). Note that this is the mass-loading rate per unit volume of cloud material, so the total mass-loading rate at any position is this $\dot{q}$ multiplied by the local cloud filling factor. We computationally track the mass remaining in clouds to ensure mass-loading ceases in regions where all the clouds have been destroyed.

2.8 Model parameter study

We have chosen the following set of models to investigate how the dynamics and observational properties of starburst-driven galactic winds depend on the host galaxy's ISM distribution, the starburst strength and history, and the presence and distribution of mass-loading by dense clouds. Although only comprising 12 simulations, we believe this to be the most detailed and systematic theoretical study of galactic winds to date. The model parameters for these simulations are summarized in Tables 1 and 2.

2.8.1 *Thick-disc models*

The thick-disc models have the same ISM distributions as TB's simulations, although run on a higher resolution computational grid. The resulting thick collimating disc allows us to investigate the effect of strong wind collimation by dense gas high above the plane of the galaxy on the wind dynamics, morphology and X-ray emission.

(i) **Model tbn_1** has a powerful starburst forming $10^8\,{\rm M}_\odot$ of

Table 1. Model parameters for the 12 starburst-driven galactic wind simulations studied. The thick- and thin-disc ISM and gravitational potential parameters are given in Table 2.

Model	ISM model	Starburst mass ($M_\odot$)	SFH	R_* (pc)	H_* (pc)	Mass-loading	Grid size (cells, $r \times z$)	Cell size (pc^2)
tbn_1	thick	10^8	SIB	150	–	none	400×800	14.6×14.6
tbn1a	thick	10^8	SIB	150	–	none	400×800	7.3×7.3
tbn1b	thick	10^8	SIB	150	60	none	640×1280	4.9×4.9
tbn_2	thick	10^7	SIB	150	–	none	400×800	14.6×14.6
tbn_6	thick	10^8	SIB	150	–	central	400×800	14.6×14.6
tbn_7	thick	10^8	CSF	150	–	none	400×800	14.6×14.6
tbn_9	thick	10^8	SIB	150	–	distributed	400×800	14.6×14.6
mnd_3	thin	10^8	SIB	150	60	none	480×800	14.6×14.6
mnd_4	thin	10^7	SIB	150	60	none	480×800	14.6×14.6
mnd_5	thin	10^8	SIB	150	60	central	480×800	14.6×14.6
mnd_6	thin	10^8	CSF	150	60	none	480×800	14.6×14.6
mnd_8	thin	10^8	SIB	150	60	distributed	480×800	14.6×14.6

Table 2. Thick and thin-disc ISM parameters.

Parameter	Thick-disc models	Thin-disc models
M_{ss} ($M_\odot$)	1.2×10^9	2×10^8
ω_0 (pc)	350	350
M_{disc} ($M_\odot$)	–	2×10^9
a (pc)	–	222
b (pc)	–	75
$n_{disc,0}$ (cm^{-3})	20	20
$c_{s,disc}$ ($km\,s^{-1}$)	30	30
$T_{disc,0}$ (K)	6.5×10^4	6.5×10^4
$n_{halo,0}$ (cm^{-3})	2×10^{-3}	2×10^{-3}
$c_{s,halo}$ ($km\,s^{-1}$)	300	300
$T_{halo,0}$ (K)	6.5×10^6	6.5×10^6
e_{rot}	0.90	0.95
Z ($Z_\odot$)	1.0	1.0

stars (assuming a Salpeter IMF between 1 and 100 $M_\odot$) instantaneously within a spherical starburst region of radius 150 pc. To investigate the interaction of the wind with the ambient ISM alone, no mass-loading is included in this simulation.

(ii) **Model tbn1a** has identical model parameters to model tbn_1, but is run on a higher resolution grid of twice the resolution to the other models (each cell is $7.3 \times 7.3\,pc^2$), although covering only a smaller physical region. This allows us to investigate the effects of limited numerical resolution of the wind properties.

(iii) **Model tbn1b** has triple the resolution of model tbn_1, with cells $4.9 \times 4.9\,pc^2$ in size. As with model tbn1a the aim to investigate the influence of numerical resolution. Unlike the other thick-disc models, the starburst region in this model is a more realistic cylindrical region also used in the thin-disc models described below.

(iv) **Model tbn_2** is almost identical to model tbn_1 with a single instantaneous starburst (SIB), except that the starburst is only one-tenth as powerful as that in model tbn_1. This starburst represents a lower limit on the power of the starburst in M82. By comparison with model tbn_1, this simulation allows us to investigate how wind properties and dynamics scale with starburst power.

(v) **Model tbn_6** has the same starburst as in model tbn_1, but mass-loading of the wind by dense clouds occurs within the starburst region (central mass-loading). This is modelled by increasing the mass injection rate from the starburst by a factor of 5.

(vi) **Model tbn_7** has a more complex star formation (CSF) history than the instantaneous starbursts used in the other models. The total mass of stars formed in the starburst is $10^8\,M_\odot$, as in model tbn_1, but the star formation is spread over a period of 10 Myr. This results in a more gradual deposition of mass and energy by the starburst, allowing us to investigate the effects of the history of mass and energy injection on the wind dynamics.

(vii) **Model tbn_9** has a SIB as in model tbn_1, but also incorporates mass-loading distributed throughout the disc as discussed in Section 2.7. In combination with model tbn_6, these mass-loaded simulations allow us to investigate both the effect of mass-loading on starburst-driven winds in combination with the wind's interaction with the ambient high filling factor ISM (unlike S96's mass-loaded simulations, where the wind did not interact with the ambient ISM), and how the distribution of the cloud material affects the wind dynamics.

2.8.2 *Thin-disc models*

The thin-disc models include a more realistic gravitational potential than the one used in TB and S94's simulations (and the thick-disc models). This new gravitational potential approximately reproduces M82's observed rotation curve (Fig. 1). The deeper potential results in a much thinner disc, with less collimation of the wind and lower gas density above the plane of the galaxy. We use a larger computational grid of 480×800 cells covering a physical region $7.0 \times 11.6\,kpc^2$ to allow for the greater radial expansion of the wind in this less collimating ISM distribution.

(i) **Model mnd_3** differs only from model tbn_1 in its thin-disc ISM distribution and more realistic gravitational potential, and its cylindrical starburst region of radius 150 pc and height 60 pc (i.e., extends to $z = \pm 30$ pc). The starburst is a SIB of total mass $10^8\,M_\odot$.

(ii) **Model mnd_4** is a weaker SIB of mass $10^7\,M_\odot$, but otherwise is identical to model mnd_3.

(iii) **Model mnd_5** is a centrally mass-loaded wind with otherwise identical model parameters to model mnd_3. As in the centrally mass-loaded thick-disc model, tbn_6 the starburst mass deposition rate has been increased by a factor of 5.

(iv) **Model mnd_6** explores the same complex SF history as model tbn_7, but in a thin-disc ISM.

(v) **Model mnd_7** is a thin-disc model with a SIB of mass $10^8\,M_\odot$ that incorporates distributed mass-loading. The total mass in clouds is very similar to model tbn_9, although the clouds are distributed within a thin disc.

3 RESULTS

We shall concentrate on three main topics in this present paper: (a) wind growth and outflow geometry, in particular the issues of wind collimation and confinement; (b) the origin and physical properties of the soft X-ray-emitting gas in these winds, in particular the filling factor of the X-ray-dominant gas, and (c) the previously unexplored aspects of wind energetics and energy transport efficiencies.

The observable X-ray properties of these models, i.e., simulated X-ray imaging and spectroscopy, will be presented in the second paper of this series. Also deferred to Paper II is the discussion of which model parameters seem best to describe M82's observed properties.

Table 3 provides a general compilation of physically interesting wind properties in all 12 of the models at a fairly typical epoch of wind growth, 7.5 Myr after the start of the starburst.

For descriptive convenience we shall define gas temperatures in the following terms. In general, 'cool' gas has temperatures in the range $4.5 \leq \log T(\mathrm{K}) < 5.5$, 'warm' gas lies in the range $5.5 \leq \log T(\mathrm{K}) < 6.5$, 'hot' gas has $6.5 \leq \log T(\mathrm{K}) < 7.5$, and 'very hot' gas has temperatures $7.5 \leq \log T(\mathrm{K}) < 8.5$.

3.1 Wind growth and outflow geometry

In this section we shall concentrate on the intrinsic morphology of the wind, in particular opening angles and the radius of the wind in the plane of the galaxy, as well as the qualitative wind structure in comparison to standard wind-blown bubbles. We shall consider the information X-ray surface brightness morphology provides separately in Paper II.

Morphological information on the wind geometry in M82 is primarily based upon optical and X-ray observations. Optical emission-line studies such as Heckman, Armus & Miley (1990), Götz et al. (1990) and McKeith et al. (1995) constrain the cool-gas

Table 3. Galactic wind properties in all the models at $t = 7.5$ Myr. Note that these values account for both lobes of the bipolar wind, except the quoted sizes, which are measured from the centre of the galaxy. The input parameters for the different models can be found in Tables 1 and 2.

Property	Units	tbn_1	tbn1a	tbn1b	tbn_2	tbn_6	tbn_7	tbn_9	mnd_3	mnd_4	mnd_5	mnd_6	mnd_7
L_{W} [a]	$10^{40}\,\mathrm{erg\,s^{-1}}$	206.0	206.0	206.0	20.6	206.0	210.0	206.0	206.0	20.6	206.0	210.0	206.0
$L_{\mathrm{X,soft}}$ [b]	$10^{40}\,\mathrm{erg\,s^{-1}}$	18.78	12.08	6.92	0.84	57.49	14.45	36.86	0.63	0.07	22.38	0.88	3.67
$L_{\mathrm{X,hard}}$ [c]	$10^{38}\,\mathrm{erg\,s^{-1}}$	8.22	8.12	6.14	0.19	51.76	3.89	13.96	5.92	1.77	40.18	2.11	7.09
$F_{\mathrm{X,int}}$ [d]	$\mathrm{count\,s^{-1}}$	30.68	19.05	10.76	1.37	79.1	24.00	50.12	0.83	0.08	21.36	1.27	5.61
$F_{\mathrm{X,abs}}$ [e]	$\mathrm{count\,s^{-1}}$	1.65	1.40	1.00	0.05	11.85	1.02	7.16	0.13	0.02	9.29	0.07	0.74
E_{inj} [f]	$10^{56}\,\mathrm{erg}$	7.10	7.10	7.10	0.71	7.10	2.53	7.10	7.10	0.71	7.10	2.53	7.10
E_{th} [g]	$10^{56}\,\mathrm{erg}$	1.55	1.35	1.15	0.15	0.75	0.65	1.53	2.47	0.44	0.81	1.15	2.57
$E_{\mathrm{th},z>1.5}$ [g]	$10^{56}\,\mathrm{erg}$	1.06	0.73	0.80	0.02	0.17	0.27	0.53	2.31	0.40	0.61	1.03	2.28
E_{KE} [h]	$10^{56}\,\mathrm{erg}$	2.73	2.51	3.21	0.19	3.13	1.08	2.74	4.86	0.35	5.75	1.78	4.70
$E_{\mathrm{KE},z>1.5}$ [h]	$10^{56}\,\mathrm{erg}$	2.04	1.71	2.58	0.04	1.51	0.51	1.63	4.27	0.30	4.28	1.22	4.05
M_{inj} [f]	$10^{7}\,\mathrm{M_{\odot}}$	1.20	1.20	1.20	0.12	1.20	0.43	1.20	1.20	0.12	1.20	0.43	1.20
M_{gas} [i]	$10^{7}\,\mathrm{M_{\odot}}$	56.5	54.8	49.4	19.5	56.8	30.9	61.1	18.9	8.0	21.1	11.7	24.9
$M_{\mathrm{gas},z>1.5}$ [i]	$10^{7}\,\mathrm{M_{\odot}}$	9.6	6.7	7.4	0.4	6.1	2.5	7.5	4.0	0.9	5.8	2.0	5.4
η_{warm} [j]	–	0.10	0.12	0.11	0.20	0.38	0.13	0.17	0.21	0.12	0.23	0.20	0.08
$f_{\mathrm{M,warm}}$ [k]	–	0.06	0.04	0.04	0.013	0.05	0.03	0.04	0.04	0.03	0.13	0.05	0.12
$f_{\mathrm{TH,warm}}$ [l]	–	0.11	0.10	0.11	0.06	0.17	0.07	0.09	0.02	0.04	0.17	0.03	0.07
$f_{\mathrm{KE,warm}}$ [m]	–	0.21	0.22	0.19	0.11	0.31	0.15	0.14	0.33	0.16	0.30	0.27	0.05
$\log n_{\mathrm{e,warm}}$ [n]	$\mathrm{cm^{-3}}$	−0.77	−0.80	−0.98	−1.06	−0.52	−0.62	−0.63	−2.15	−2.30	−1.54	−1.80	−1.52
v_{warm} [o]	$\mathrm{km\,s^{-1}}$	621	668	802	433	745	646	607	1936	1143	732	1579	289
η_{hot} [p]	–	0.81	0.75	0.83	0.55	0.32	0.72	0.77	0.71	0.82	0.55	0.80	0.87
$f_{\mathrm{M,hot}}$ [q]	–	0.03	0.03	0.04	0.005	0.03	0.02	0.07	0.18	0.11	0.08	0.15	0.18
$f_{\mathrm{TH,hot}}$ [r]	–	0.57	0.45	0.66	0.23	0.61	0.40	0.78	0.83	0.88	0.76	0.89	0.81
$f_{\mathrm{KE,hot}}$ [s]	–	0.49	0.41	0.59	0.16	0.15	0.46	0.50	0.56	0.74	0.53	0.66	0.89
$\log n_{\mathrm{e,hot}}$ [t]	$\mathrm{cm^{-3}}$	−2.04	−1.91	−2.02	−2.15	−0.79	−1.82	−1.31	−2.65	−2.76	−1.50	−2.74	−2.40
v_{hot} [u]	$\mathrm{km\,s^{-1}}$	804	742	836	660	591	889	735	772	644	331	693	815
z_{max} [v]	pc	7088	5826	6217	3471	4025	5469	6329	8444	5338	6635	6796	7831
r_{max} [w]	pc	2888	2392	2460	1327	1546	1983	2115	5513	3675	4404	4696	5119
r_{base} [x]	pc	1167	1096	1102	695	1259	841	1220	1220	763	1395	904	1045

[a] Starburst mechanical energy injection rate averaged over the period between $t = 6.5$ and 7.5 Myr.
[b] Intrinsic soft X-ray luminosity in the *ROSAT* 0.1–2.4 keV band.
[c] Intrinsic hard X-ray luminosity in the 2.4–15.0 keV energy band.
[d] *ROSAT* PSPC count rate assuming no absorption and distance $D = 3.63$ Mpc to M82.
[e] *ROSAT* PSPC count rate assuming a uniform hydrogen column of $N_{\mathrm{H}} = 4 \times 10^{20}\,\mathrm{cm^{-2}}$ (the Galactic column density towards M82; Stark et al. 1992) and distance $D = 3.63$ Mpc to M82.
[f] Total energy and mass injected from SNe and stellar winds in the starburst up to this time.
[g] Total thermal energy within the entire wind (E_{TH}), and within those parts of the wind lying above $z = 1.5$ kpc ($E_{\mathrm{TH},z>1.5}$).
[h] Total kinetic energy within the entire wind (E_{KE}), and within those parts of the wind lying above $z = 1.5$ kpc ($E_{\mathrm{KE},z>1.5}$).
[i] Total gas mass within the entire wind and within the wind lying above $z = 1.5$ kpc
[j] Volume-filling factor of the warm [$5.5 \leq \log T(\mathrm{K}) < 6.5$] gas.
[k] to [m] Fraction of total gas mass (f_{M}), thermal energy (f_{TH}) and kinetic energy (f_{KE}) in warm gas.
[n] Root mean square electron density of warm gas within the wind.
[o] Volume-averaged velocity of warm gas.
[p] to [u] As *i–o*, but for hot [$6.5 \leq \log T(\mathrm{K}) < 7.5$] gas.
[v] Maximum extent of the wind (the position of the outermost shock) along the minor axis measured from the nucleus of the galaxy.
[w] Maximum radial extent of the wind, measured from the minor axis.
[x] Maximum radial extent of the wind in the plane of the galaxy (i.e., at $z = 0$).

outflow geometry strongly within $z \lesssim 2$ kpc of the plane of the galaxy, using spectroscopy and imaging. Narrow-band optical imaging can trace the wind out to $z \sim 6$ kpc. X-ray observations by the *ROSAT* PSPC and HRI also trace the warm and hot phases of the wind out to $z \sim 6$ kpc from the plane, but suffer from poor resolution and point-source confusion near the plane of the galaxy.

3.1.1 *Wind density structure*

As an effective visual method of illustrating galactic wind evolution and growth, and some of the differences between the various models, we reproduce grey-scale images of log number density in the r–z plane in Figs 4–7. These show the wind at 2.5-Myr intervals up to $t = 10$ Myr in models tbn_1 and mnd_3, and at $t = 7.5$ Myr in all the other models except models tbn1a and tbn1b.

We shall briefly describe the evolution and structure of the wind in model tbn_1 (see Fig. 4), a single instantaneous starburst occurring in the thick-disc ISM, and then discuss the differences in the evolution of the wind in the other models to this model. Differences between model tbn_1 and the higher resolution models tbn1a and tbn1b are discussed in Section 4, along with a general discussion of the effects of finite numerical resolution.

At $t = 2.5$ Myr the starburst-driven superbubble has yet to blow out of the thick disc, although it is elongated along the minor axis. Though difficult to see when shown to scale alongside the later stages of the wind, the superbubble has a standard structure of starburst region, free wind, shocked wind and a denser cooler shell of swept-up and shocked disc material.

By $t = 5$ Myr the superbubble has blown out, the dense superbubble shell fragmenting under RT instabilities. The superbubble shell was RT-stable as long as it was decelerating, but the negative density gradient along the z-axis and the sudden influx of SN energy at $t \sim 3$ Myr rapidly accelerate the shell along the minor axis after $t \sim 3$ Myr. The internal structure of the wind is more complex than the superbubble described above. A new shell of shocked halo matter forms, but given its low density and high temperature, it never cools to form a dense shell as in the superbubble phase. The re-expanding shocked wind can be seen to

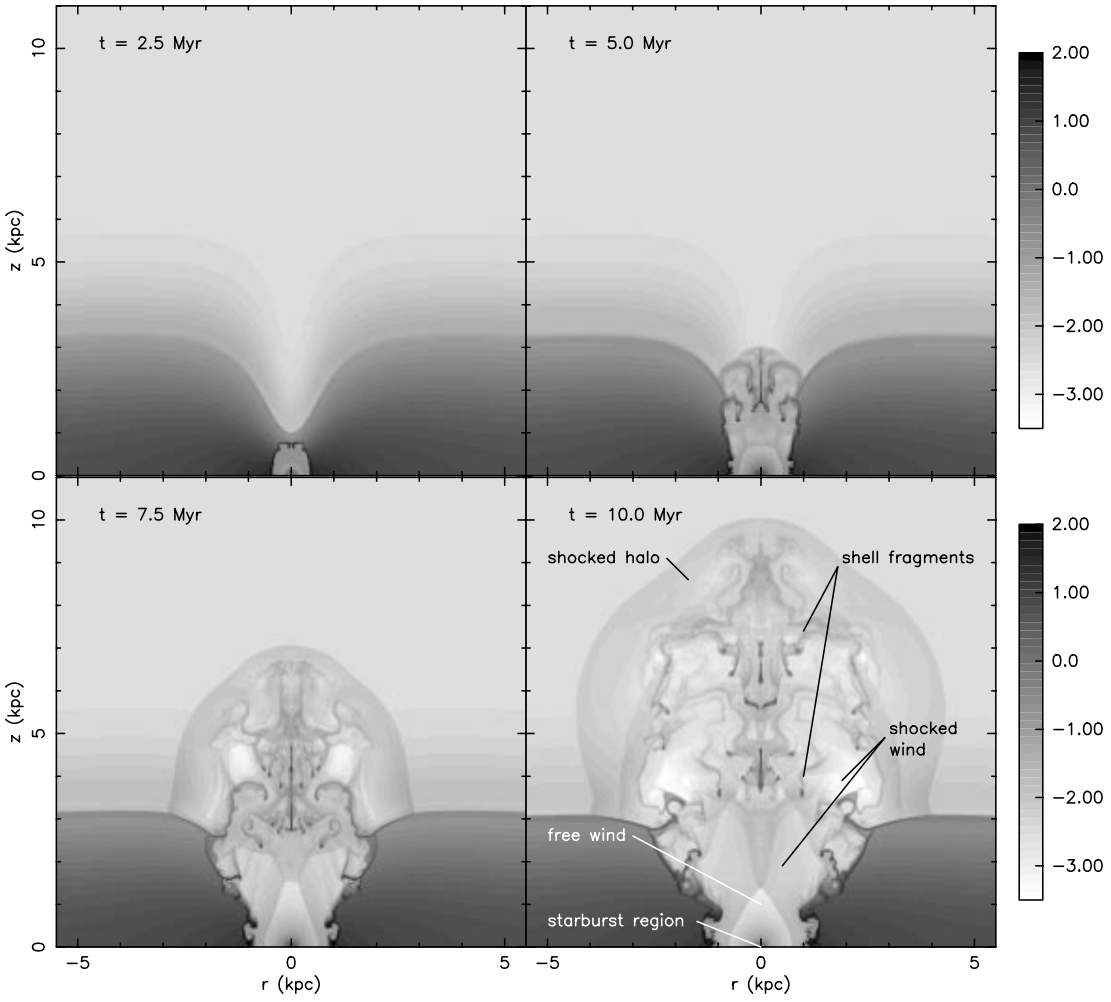

Figure 4. The logarithm of the wind number density in the thick-disc model tbn_1 at four epochs. The intensity scale extends over the range $-3.5 \leq \log n(\mathrm{cm}^{-3}) \leq 2.0$, and number densities above or below this range are shown as black or white respectively. The final panel labels some important features of the wind: the starburst region in the nucleus of the galaxy, the freely expanding wind, shocked wind, shocked disc and halo gas, and superbubble shell fragments. Note that these numerical simulations assume cylindrical symmetry around the z-axis, so the shell fragments are actually annuli. Note the very small region of freely expanding wind, the initially cylindrical geometry of the wind opening out with time into a truncated cone, and the increasing size of the wind in the plane of the galaxy.

be ablating the shell fragments. Note also the structure of the reverse shock terminating the free wind region, which is no longer spherical. The oblique nature of this shock away from the minor axis acts to focus material out of the plane of the galaxy, as first described by TI. The combination of the disc density gradient and this shock-focusing make the wind cylindrical at this stage.

Note that the complex structure of the wind after blowout and shell fragmentation means that it is not meaningful to model the emission from interior of a galactic wind using the standard Weaver et al. (1977) similarity solutions. Nevertheless, semi-analytical models based on the thin-shell approximation (e.g. Mac Low & McCray 1988; Silich & Tenorio-Tagle 1998) can be used to explore the location of the outer shock of the wind with good accuracy, provided the radiative losses from the interior of the wind are not significant. Tracking the location of the outer shock is perhaps only important in assessing if a superbubble of a set mechanical energy injection rate can blow out of a given ISM distribution. Calculations of observable properties and the long-term fate of the matter in any outflow do require the use of multi-dimensional hydrodynamical simulations.

The wind geometry within the disc is similar to a truncated cone at $t = 7.5$ Myr. In the halo the outer shock propagating in the halo becomes more spherical as the anisotropy of the ISM reduces with increasing distance along the z-axis. The structure of the shocked wind region is becoming even more complex, as it interacts with the superbubble shell fragments. The shell fragments are steadily being carried out of the disc, although being slowly spread out over a larger range of z with time. The shocked wind also interacts with the disc, removing disc gas and carrying it slowly out of the disc.

At $t = 10$ Myr the wind has increased in size, but remains qualitatively very similar in structure to the wind at $t = 7.5$ Myr. Shell fragments are spread over $3.5 \leq z \leq 7$ kpc, a large range given their common origin in the superbubble shell. Long tails can be seen extending from the shell fragments, their curling shapes tracing the complex flow pattern within the shocked wind.

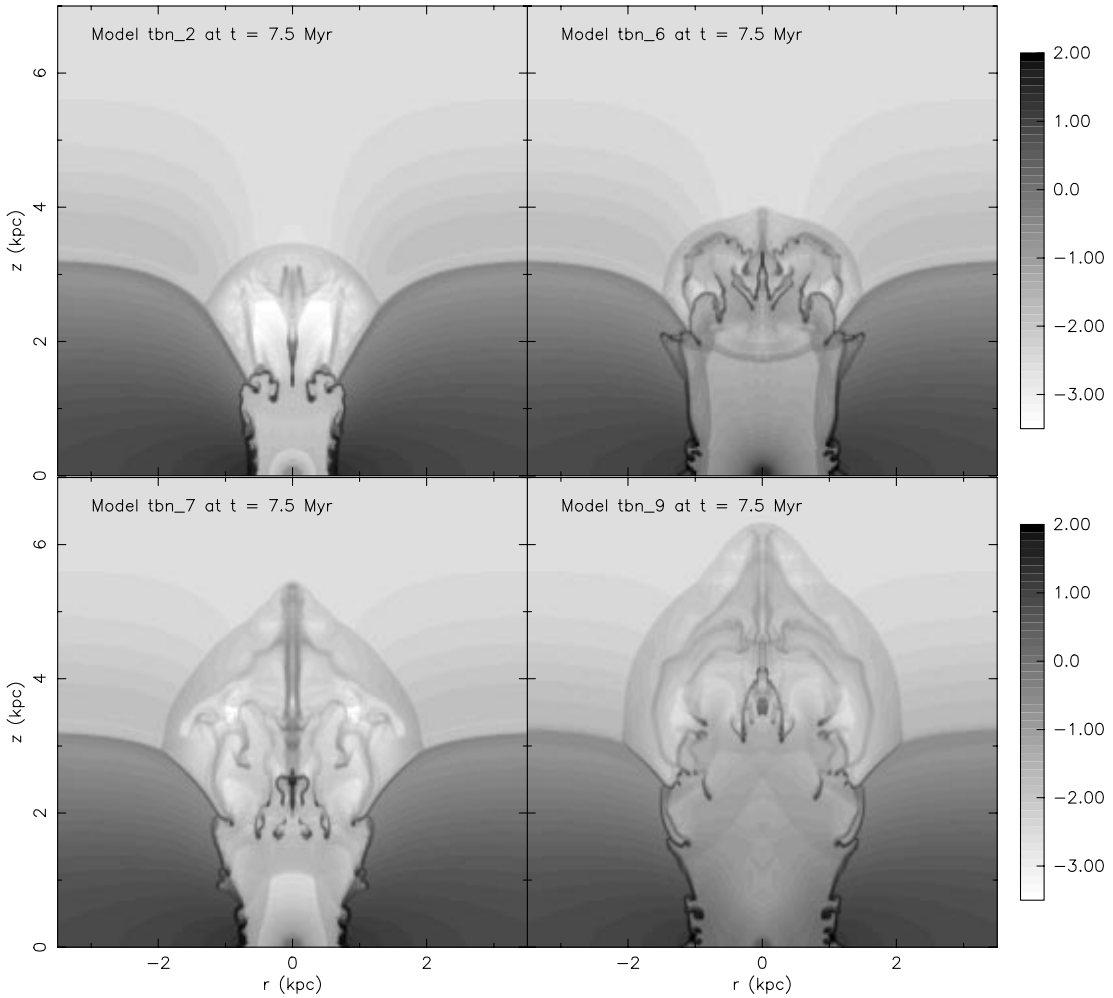

Figure 5. The logarithm of the wind number density in the thick-disc models tbn_2, tbn_6, tbn_7 and tbn_9 at $t = 7.5$ Myr. The intensity scale extends over the range $-3.5 \leq \log n(\mathrm{cm}^{-3}) \leq 2.0$, and number densities above or below this range are shown as black or white respectively. The weaker starburst tbn_2 (10 times less powerful than model tbn_1) leads to a smaller but otherwise structurally similar wind to model tbn_1. In model tbn_6 the cooler and denser wind (due to the additional mass injection within the starburst region) significantly alters the structure of the regions of shocked wind material within the galactic wind, and reduces its expansion rate. The more gradual energy injection rate of model tbn_7 compared to model tbn_1 also reduces the wind's growth rate, but otherwise this model is very similar to model tbn_1. The interior structure of the wind in model tbn_9 is much more homogeneous than the other thick-disc models due the enhanced wind density due to distributed mass-loading, and it is difficult to distinguish separate free wind and shocked wind regions.

Regions of expansion followed by new internal shocks can also be seen within the shocked wind, a marked difference from the structure of conventional wind blown bubbles.

With mass and energy injection rates from the starburst reduced by a factor of 10 from model tbn_1, the wind in model tbn_2 evolves at a slower pace than model tbn_1 (see Fig. 5). The eventual wind structure is very similar to that of model tbn_1, although disruption of the disc appears reduced and the wind remains more cylindrical within the disc. From standard self-similar wind-blown bubble theory (Weaver et al. 1977) the size of a pressure-driven bubble is only a weak function of the energy injection rate, $R \propto L_{\rm w}^{1/5}$, so we might expect model tbn_2 to be $\sim$60 per cent the size of model tbn_1 at any given epoch. In practice, model tbn_2 is less than 60 per cent the size of model tbn_1 at the same epoch, which may be due the increased relative importance of radiative cooling in depressurising tbn_2's wind, given that the cooling time-scales are the same in both simulations.

The wind in model tbn_6 (Fig. 5) grows at slower rate than model tbn_1, despite having exactly the same energy injection history. In this case the reduced growth must be due to the central mass-loading used. The mass injection rate within the starburst has been increased by a factor of 5 from that due to stellar winds and SNe alone, representing the entrainment of dense gas remaining from the star formation. The central mass-loading increases the density of the free wind by a factor of $5^{3/2} \approx 11$, due to the additional mass and the reduced outflow rate (as the energy per particle is less), and reduces the temperature of the gas by a factor of 5 from $\sim 1.5 \times 10^8$ to $\sim 3 \times 10^7$ K. Despite the enhanced density of the material ejected from the starburst, the wind retains recognizable features of shell fragments and shocked halo, although their dynamics and morphology have clearly been altered by the denser, slower wind fluid in this model.

Model tbn_7 (Fig. 5) was chosen to investigate the effect of a more gradual energy and mass injection history than the instantaneous starburst used in the other models (see Fig. 2). Apart from the resulting slightly slower growth, the structure of the wind in this model is very similar to that in model tbn_1.

The distributed mass-loading in model tbn_9 significantly increases the density of what would be the free and/or shocked wind regions. Note the apparent lack of an obvious shock separating the free wind and shocked wind regions in this model (Fig. 5). This is not unexpected, as distributed mass-loading has the interesting property of increasing the Mach number of subsonic flows while reducing the Mach number in supersonic flows, to produce a flow with a Mach number of order unity (Hartquist et al. 1986). As in model tbn_6, the wind's growth is slightly slower than the non-mass-loaded model tbn_1.

The wind structure in model mnd_3 (Fig. 6) is significantly different from model tbn_1 due to the thin, less-collimating disc used in this and the following models. The lack of substantial amounts of dense gas above the starburst region allows very rapid blowout of the wind, easily shattering a much less massive superbubble shell. The net result is a wind with a larger opening angle (due to the lack of any significant collimation by the disc), a very large free wind region, and an indistinct region of shocked

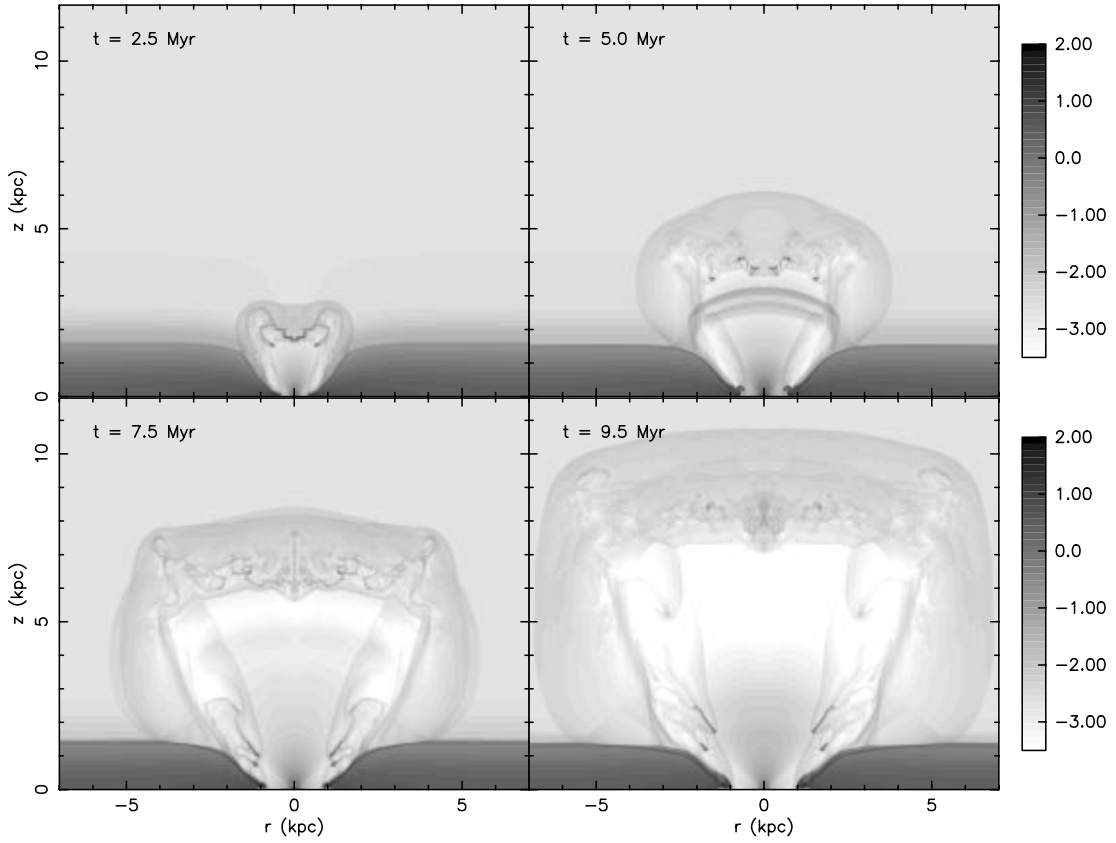

Figure 6. The logarithm of the wind number density in the thin-disc model mnd_3 at four epochs. The intensity scale extends over the range $-3.5 \leq \log n(\mathrm{cm}^{-3}) \leq 2$, and number densities above or below this range are shown as black or white respectively. By comparison with the thick-disc model tbn_1, note the very large volume occupied by the freely expanding wind and the large opening angle. Due to the lack of disc material above the starburst the importance of shocked disc and shell fragments is reduced in these thin-disc models.

wind and shocked disc material surrounded by the standard shocked halo region. The few superbubble fragments rather rapidly loose definition and are mixed in with the shocked wind by $t \sim 7.5$ Myr. Due to the early blowout into the halo and the lack of collimation, the wind is much more spherical than in the thick-disc models.

The morphology of the weak starburst model mnd_4 (Fig. 7) is generally similar to that of model mnd_3, although with two interesting exceptions. The much less energetic wind is not able to punch out into the halo as effectively as the wind in model mnd_3. A weak, almost spherical, shock wave does propagate out into the halo, leading to a wind with much of the volume being shocked halo material. Also note that the free wind is confined to a narrow region along the z-axis by shocked wind material flowing up out of the disc. This flow of shocked wind is also present in the other thin-disc models, and is responsible for their peculiar, almost box-like, morphology.

The structure and growth of the central mass-loaded thin-disc model mnd_5, the complex star formation history model mnd_6, and the distributed mass-loading model mnd_7 (see Fig. 7) are related to the basic thin-disc model mnd_3 in the same way as the equivalent thick-disc models are related to model tbn_1.

The main differences between the thin-disc models and the thick-disc models are the lack of collimation in the thin models, the resulting large regions of freely expanding wind, and less complex shocked wind, and disc regions with shell fragments that are disrupted and mixed into the flow at an earlier stage.

3.1.2 *Wind growth*

The vertical and radial growth of the galactic winds as a function of time in these models is shown in Fig. 8. The maximum vertical extent of the wind (almost invariably size of wind on the z-axis) $z_{\rm max}$, maximum radial extent $r_{\rm max}$ and radius of the base of the wind $r_{\rm base}$ in all the models can be seen to be well-behaved power laws (or broken power laws) in time.

The vertical and radial growth rates in the thick-disc models clearly differ from those in the thin-disc models. The thick-disc models all show initially slow vertical ($z_{\rm max}$) and radial growth ($r_{\rm max}$), followed by rapid acceleration. The wind begins to accelerate along the z-axis after $t \sim 3$ Myr, and later along the r-axis, $t \sim 5$ Myr. The initial evolution is similar to that predicted by the Weaver et al. (1977) model of a pressure-driven bubble in a constant density medium, i.e., $R \propto t^{0.6}$. The later phase of acceleration is caused by both the superbubble 'running down'

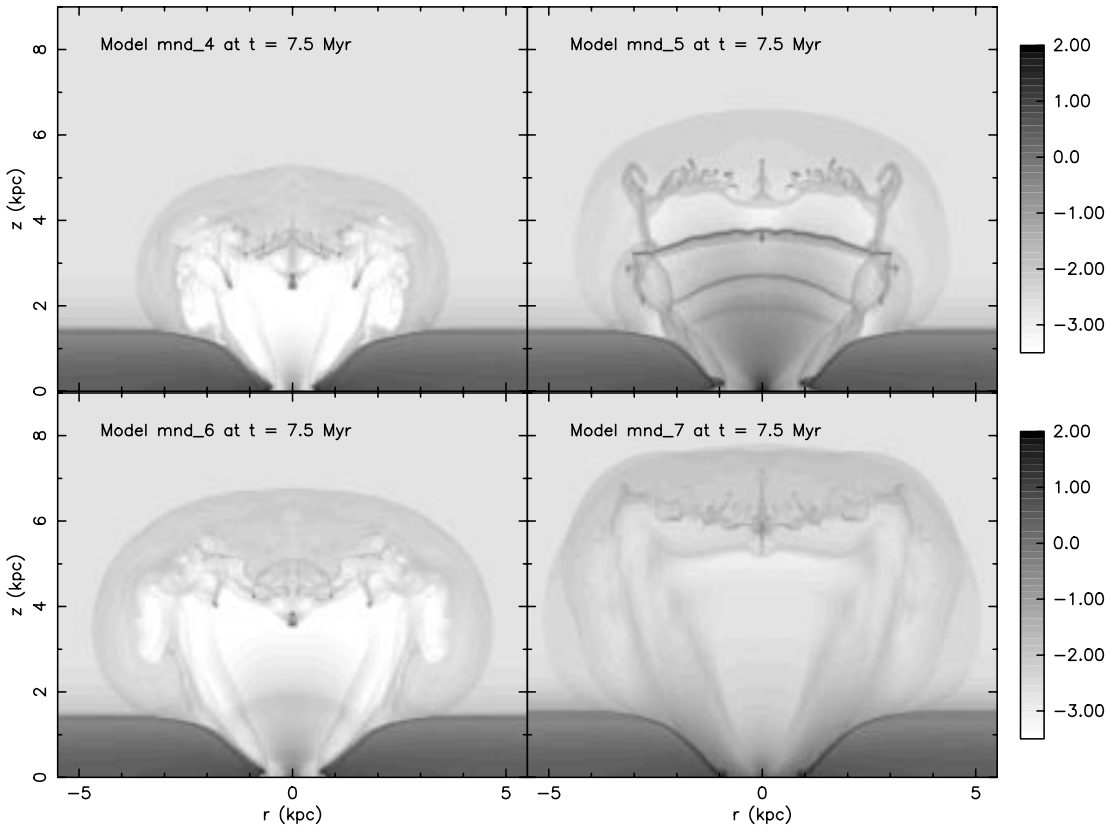

Figure 7. The logarithm of the wind number density in the thin-disc models mnd_4, mnd_5, mnd_6 and mnd_7 at $t = 7.5$ Myr. The intensity scale extends over the range $-3.5 \leq \log n(\mathrm{cm}^{-3}) \leq 2$, and number densities above or below this range are shown as black or white respectively. The weak starburst in model mnd_4 leads to a smaller free wind region, and the majority of the outflow volume is occupied by shocked halo material. In model mnd_5, as in model tbn_6, the cooler and denser mass-loaded wind alters the structure of the regions of shocked wind material within the galactic wind. The sharp features seen propagating out in the free wind are due to periods of increased mass injection in the instantaneous starburst model used (see Fig. 2). The simple model for central mass-loading used assumes that the total mass-loading rate in the starburst region is just a multiple of the starburst mass injection rate. A more realistic model of starburst history and mass-loading would lead to a smoother mass injection rate. The more gradual energy injection rate of model mnd_6 compared to the instantaneous burst model mnd_3 reduces the wind's growth rate slightly, but otherwise this model is very similar to model mnd_3. In model mnd_7 the density of the free wind is increased due to distributed mass-loading. As the clouds are assumed to be distributed in the same way as the ambient ISM, most of the mass-loading occurs not near the z-axis but near the outer edge of the wind.

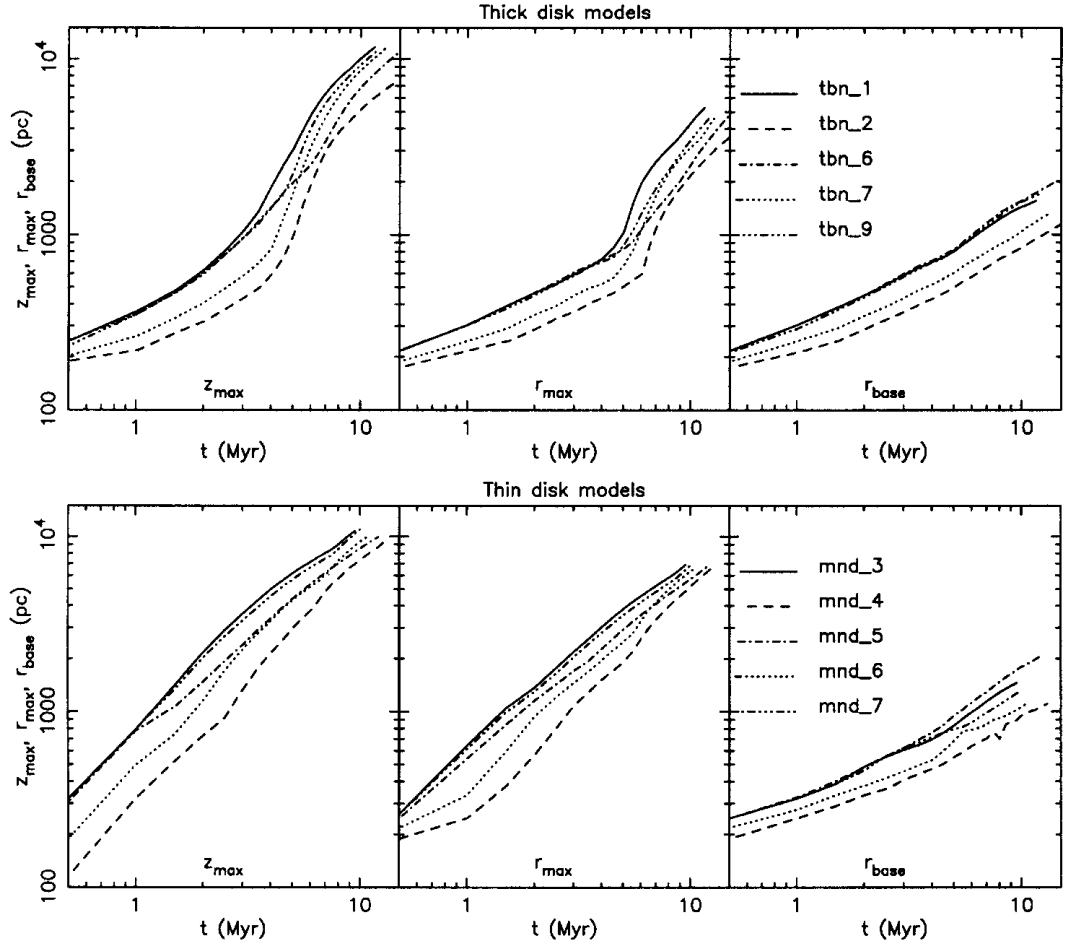

Figure 8. Vertical and radial growth of all the wind models as a function of time. The initial evolution of the maximum vertical size $z_{\rm max}$, maximum radial size $r_{\rm max}$ and size of the wind in the plane of the galaxy $r_{\rm base}$ for the thick-disc models, obey the $R \propto t^{0.6}$ law expected of confined pressure-driven bubbles. Post-blowout (which occurs almost instantaneously in the thin-disc models) $z_{\rm max}$ and $r_{\rm max}$ grow more rapidly, as the wind accelerates down the density gradient into the halo.

the ISM density gradient leading into the halo, and the dramatic increase in mechanical energy injection rate at $t \sim 3$ Myr due to the first SNe. At later times the wind should return to the $R \propto t^{0.6}$ expansion law once it is in the almost constant density halo. The initial stages of this final deceleration may be what is seen in Fig. 8 at late times in models tbn_2 and tbn_7.

By contrast, the wind in the thin-disc models shows no evidence for periods of increased or decreased acceleration over the simulation. Measured over the period from $t = 0.5$ Myr until the end of the simulation, the wind is constantly accelerating both vertically ($1.10 \leq \partial \log z_{\rm max}/\partial \log t \leq 1.37$) and radially ($1.04 \leq \partial \log r_{\rm max}/\partial \log t \leq 1.25$) in all the thin-disc models. The thin disc allows the wind to blow out very early in its evolution, and it gradually runs down the density gradient into the halo.

In all the models (both thin- and thick-disc) the growth of the wind in the plane of the galaxy ($r_{\rm base}$) is well approximated by the expansion law of a constant power bubble expanding into a uniform medium. The base of the wind expands at a rate $\partial \log r_{\rm base}/\partial \log t \sim 0.6$, measured over the period $t = 0.5$ Myr until the end of the simulation. The range in slope around the expected value of 0.6 is small, from 0.53 (model mnd_6) to 0.67 (model tbn_9), and does not deviate in any clear systematic manner due to mass-loading, the ISM distribution or the star formation history.

There is no evidence for a change in $\partial \log r_{\rm base}/\partial \log t$ once the wind has broken out, as might be expected if blowout leads to a depressurisation of the wind. The evolution of the hot gas in the plane of the galaxy does not appear to be affected by the blowout over the period covered by our simulations.

3.1.3 Wind collimation and opening angles

The density distributions shown in Figs 4–7 clearly demonstrate that the main factor controlling the wind morphology is the disc ISM distribution. The thick disc ISM models produce initially cylindrical winds that evolve into collimated truncated conical winds with low opening angles. The thin-disc models invariably produce conical winds with large opening angles.

These outflow geometries should be compared to that inferred from optical observations of M82 (see Fig. 9), of an initially conical wind ($r \sim 420$ pc for $z \leq 330$ pc) flaring out above $z = 330$ pc into a cone of opening angle[1] $\theta \sim 30°$ (based on Götz et al. 1990 and McKeith et al. 1995, scaled to our assumed distance of 3.63 Mpc to M82).

[1] Note that we quote the full opening angle, and not the half opening angle, which is also commonly used in the literature.

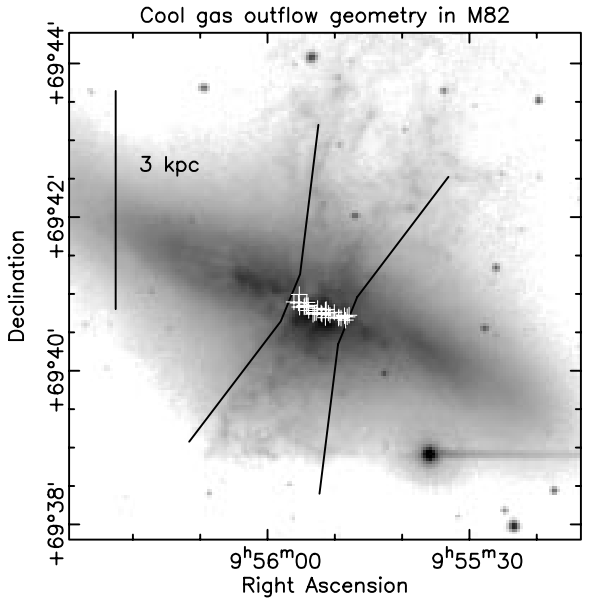

Figure 9. The wind outflow geometry in M82 based on the work of Götz et al. (1990) and McKeith et al. (1995), overlaid on a Hα image. The young SNRs (Muxlow et al. 1994) marking the starburst region are shown as a series of white crosses.

Measuring the wind opening angles in our models as a function of time, it is clear that the thin-disc models fail to produce such a well-collimated wind. The opening angle is $\theta_{\rm thin} \sim 90°$ in model mnd_3 at all epochs, which is typical of all the thin-disc models.

By comparison, the thick-disc models (deliberately chosen to provide a collimating ISM distribution) are much more successful, although even in these models the opening angles can become too large to be a good match for M82 at late times. The opening angles in the thick-disc models do show some variation between the different models, but typically the wind is initially spherical in its superbubble phase, becoming much more cylindrical (i.e., $\theta \sim 0°$) as it begins to blow out. Post-blowout the opening angles are typically $\theta_{\rm thick} \sim 40°$, but this masks a general increase from $\theta \sim 0°$ at $t \sim 5$ Myr to $\theta \sim 60°$ at $t \sim 10$–15 Myr. More gentle energy injection histories, as in models tbn_2 and tbn_7, do give *slightly* lower opening angles at a given epoch than in model tbn_1, confirming S94's conclusion that weak initial winds can reduce later disruption of the disc by the more energetic phases of the starburst. Note that this is a *weak* effect in the simulations we consider, and the main factor affecting wind geometry is the initial ISM distribution, not the starburst energy injection history.

It is clear that a thick, collimating ISM distribution seems necessary to reproduce the observed narrow, low opening angle, wind in M82. Even our thick-disc model does not provide sufficient collimation.

3.1.4 Confinement

TT's criticism that the size of the base of the wind is too large in TB and S94's simulations remains true in these simulations. The radius of the wind in the plane of the galaxy grows larger than that observed in M82, and shows no signs of slowing down, as can be seen Fig. 8.

Götz et al.'s (1990) observations limit the radius of the wind to $r \sim 420$ pc at $z \sim 110$ pc above the plane of the galaxy. This radius is very similar to the extent of the SN remnants that measure the current SN rate (see Fig. 9).

By contrast, $r_{\rm base} \sim 1500$ pc in model mnd_3 at $t = 9.5$ Myr, a factor of 10 larger than the assumed starburst region. All the simulations have base radii in the range $r_{\rm base} \sim 1$–2 kpc at $t \sim 10$ Myr. A dramatic reduction in starburst power by a factor of 10 (model tbn_1 to model tbn_2) only reduces $r_{\rm base}$ from $\sim$1400 pc to $\sim$850 pc at $t = 10$ Myr.

By $t = 5$ Myr the base of the wind is too large in all the models, so to explain this problem away with the ISM distributions we have used would require M82's starburst to be very young, i.e., $t < 5$ Myr. This is difficult to justify observationally and, as we shall show in Paper II, the observed X-ray extent of the wind requires a slightly older wind ($t \gtrsim 7.5$ Myr).

TT constructed steady-state models of bipolar outflows from starburst galaxies, where the ram pressure of infalling dense molecular gas confines the radius of the base of the wind to a fixed position. Although this solves the confinement problem, their model requires unphysically large masses of gas to be falling in along the plane of the galaxy. For example, in the model published in TT, the mass of the ISM within central kiloparsec is $M_{\rm gas} \sim 5 \times 10^9\,{\rm M}_\odot$, where observations of M82 limit the total mass of the ISM to be $\lesssim 10^8\,{\rm M}_\odot$ within the same radius.

Dense molecular gas, even if not falling into the nuclear region, may none the less be important for confining the base of the wind. CO observations (Nakai et al. 1987) reveal a molecular 'ring' extending in radius between $r \sim 100$–400 pc, at the outer edge of which spurs of molecular material emerge perpendicular to the plane and extend $\sim$500 pc from the disc. Much of the gas mass within the central kiloparsec is probably within this molecular gas. It may be that this molecular ring can provide the wind with enough resistance to slow its expansion in the plane of the galaxy. Although this molecular gas does not have a volume-filling factor of order unity as envisioned by TT (see Lugten et al. 1986), its areal filling factor may be high, and it undoubtedly could strongly mass-load the wind in the plane of the galaxy. Further simulations explicitly including a molecular ring are currently in progress to explore this possibility.

Somewhat more speculatively, magnetic fields might collimate the wind (e.g. de Gouveia Dal Pino & Medina Tanco 1999). We do not believe that pursuing this option is currently necessary, given that the alternatives have not yet been explored. Nevertheless, we explore this idea further when discussing magnetic fields in Section 4.1.

3.2 X-ray emission from galactic winds

3.2.1 Efficiency of soft X-ray emission

Soft X-ray luminosities as a function of time, for all the models excluding the resolution study models tbn1a and tbn1b, are shown in Fig. 10, in comparison to the starburst mechanical energy injection rate $L_{\rm W}$. Note the overall similarity in form between $L_{\rm X}$ and $L_{\rm W}$, with periods of increased starburst energy injection are closely followed by periods of increased soft X-ray emission (time lag $\Delta t \sim 0.5$ Myr).

The thick-disc models are clearly significantly more X-ray-luminous than the equivalent thin-disc models. Lacking significant amounts of dense gas for the wind to interact with, the thin-disc models are very inefficient at radiating the mechanical energy supplied by the starburst. Typically, the thin-disc models radiate $\lesssim$1 per cent of $L_{\rm W}$ as soft X-rays in the *ROSAT* band. By contrast,

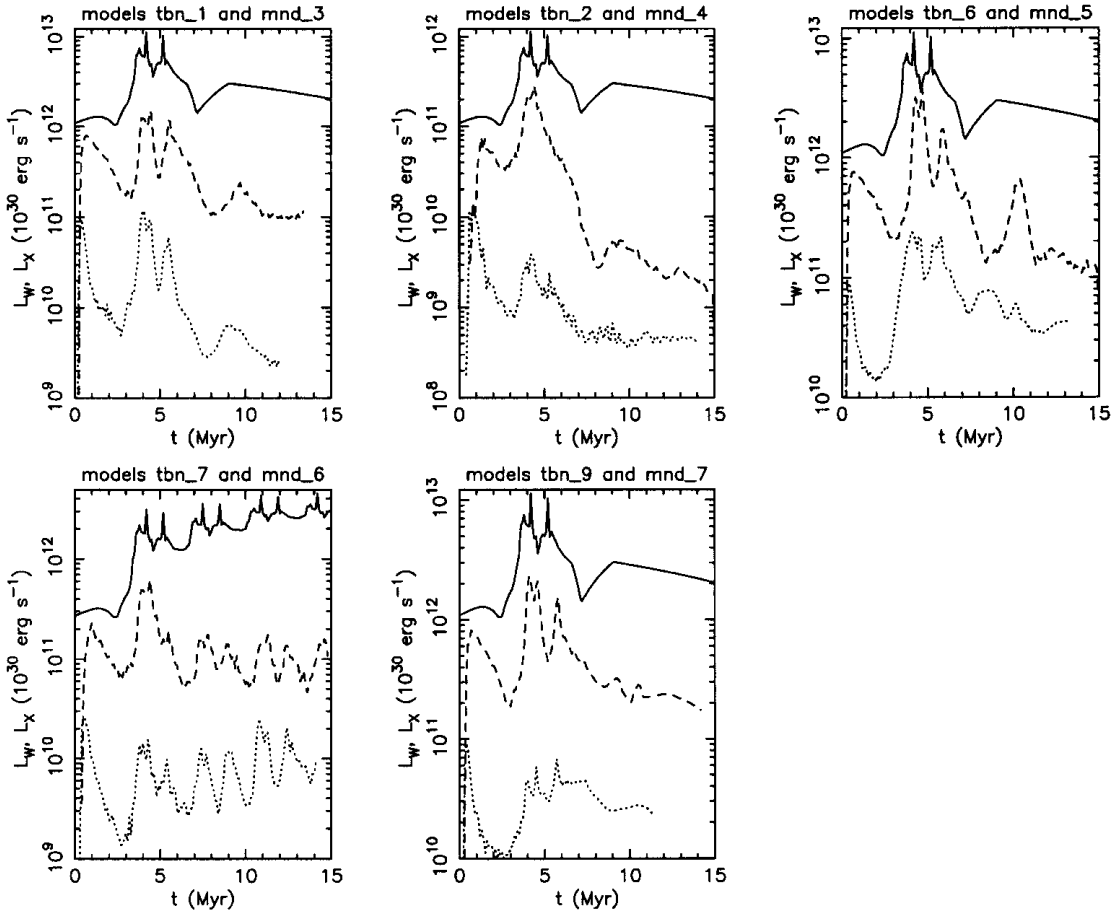

Figure 10. Soft X-ray luminosities in the *ROSAT* 0.1–2.4 keV band for the simulated galactic winds compared to the starburst energy injection rate L_W. The five panels show L_W (solid line) and L_X for each of the starburst models. Equivalent models differing only in having thick-disc (dashed line) or thin-disc (dotted line) ISM distribution have been grouped together. Note the overall similarity in form between L_X and the L_W – periods of increased starburst energy injection are closely followed by periods of increased soft X-ray emission. The initial spike of high X-ray luminosity in all the models for $t \lesssim 2$ Myr is a numerical artefact due to poor numerical resolution when the superbubble is very young.

the thick-disc models typically radiate ~5 per cent of L_W, and up to ~20 per cent of L_W at some epochs.

Note that the high X-ray luminosities at early times, $t \lesssim 2$ Myr, are numerical artefacts due to poor numerical resolution of the very young superbubbles when they cover only relatively few computational cells.

The primary variable influencing the emerging X-ray luminosity of these galactic winds is the ISM density distribution. The starburst energy injection rate L_W is of secondary importance (in that $L_X \propto L_W$), followed by the presence of mass-loading.

Both mass-loading (models tbn_6, tbn_9, mnd_5 and mnd_7) and more distributed star formation histories (models tbn_7 and mnd_6) increase the soft X-ray luminosities at later times with respect to the luminosities found in the instantaneous starburst models. Central mass-loading is most noticeable in altering the X-ray emission in the thin-disc models (model mnd_5), where the soft X-ray luminosity can be increased by typically an order of magnitude from the non-mass-loaded models. Mass-loading, either distributed or central, is much less significant in the thick-disc models, where the soft X-ray luminosities are typically 1 to 3 times those in the non-mass-loaded models.

The extremely high absolute values of some of these soft X-ray luminosities should be remarked upon. In the thick-disc models L_X is typically several times 10^{41} erg s^{-1}, while in the thin-disc models it is approximately an order of magnitude lower. The mass-loaded thick-disc models tbn_6 and tbn_9 have peak 0.1–2.4 keV luminosities $L_X \sim 2 \times 10^{42}$ erg s^{-1}. This is considerably more luminous than the majority of starburst galaxies, which typically have total X-ray luminosities in the *ROSAT* 0.1–2.4 keV band in the range 10^{39}–10^{41} erg s^{-1} (e.g. Read et al. 1997), of which only a fraction is due to hot gas. Only the most luminous starburst galaxies have soft X-ray luminosities as high as we find in some of our models; e.g., NGC 3690 has $L_X \sim 5 \times 10^{41}$ erg s^{-1} (Zezas, Georgantopoulos & Ward 1998).

Both TB and S94's simulations had high simulated X-ray luminosities in the range 10^{41}–10^{42} erg s^{-1}. With reasonably similar parameters it is not surprising that we find similar luminosities. That real starburst galaxies do not typically have such high soft X-ray luminosities may be telling us that the physical conditions assumed in the high-L_X models are not a good representation of the true conditions within starburst galaxies such as M82. However, we must be careful in interpreting the absolute values of L_X from numerical simulations, as low numerical resolution leads to overestimated X-ray luminosities, as discussed in Section 4. The X-ray luminosities in higher resolution simulations will be lower, though similar in form, than those in these simulations.

Another factor leading to high soft X-ray luminosities in these

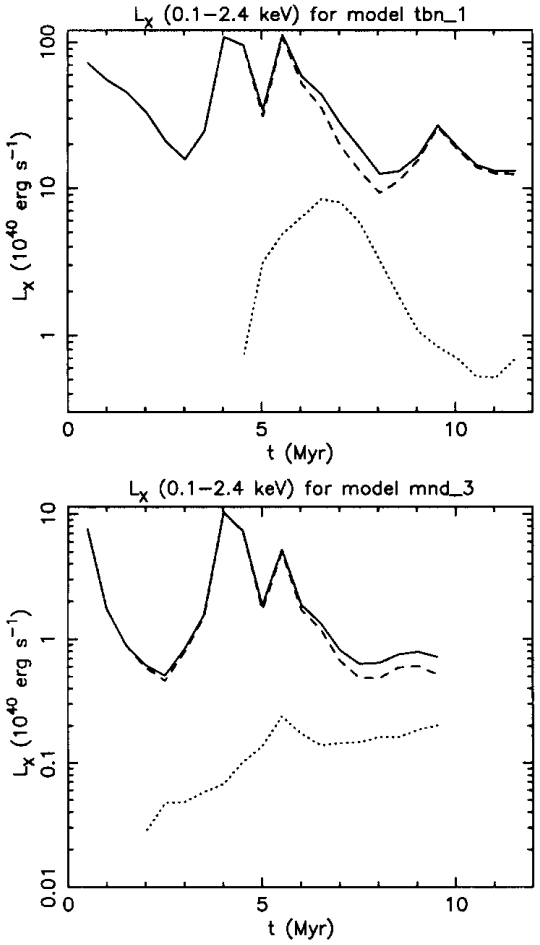

Figure 11. Soft X-ray luminosity as a function of time and position in models tbn_1 and mnd_3. The total *ROSAT* 0.1–2.4 keV band X-ray luminosities are shown as a function of time (solid line), along with L_X decomposed into emission from within the disc ($|z| \leq 1.5$ kpc, dashed line) and halo ($|z| > 1.5$ kpc, dotted line). At least half of the total soft X-ray emission is produced within the plane of the galaxy in all the models we have run.

models is the assumption of solar metallicity, as discussed in Section 2.6. As we shall discuss below, when considering in detail the origin of the X-ray emission from within the galactic wind (Section 3.3), the majority of the soft X-ray emission comes from regions of interaction between swept-up disc material and the wind, and not directly from the hot metal-enriched shocked wind fluid. If the ambient ISM material has subsolar abundances, then the resulting X-ray luminosities will be reduced proportionally (see Fig. 3).

A particularly interesting question not answered by the total X-ray luminosities given in Fig. 10, or in TB and S94, is whether the X-ray emission is dominated by particular regions within the wind (e.g., gas within the disc or in the halo), or is relatively uniformly spread throughout the wind volume.

A significant fraction of the X-ray emission from these galactic winds comes from hot gas in the plane of the galaxy (Fig. 11). X-ray emission away from the plane of the galaxy, in what would observationally be classed the 'wind,' is typically much less luminous than that from the plane of the galaxy. This is important, as observational studies of the hot gas in the disc of galaxies with classic starburst-driven winds (i.e., edge-on systems), such as M82, are hampered by source confusion and high absorption columns. A result of this is that clear predictions of the X-ray properties of galactic winds away from the plane of the galaxy, where absorption and source confusion are less of a problem, are necessary.

3.2.2 *Hard X-ray emission*

Hard thermal X-ray emission from the galactic wind comes predominantly from the starburst region itself, with a lesser contribution from the free wind and shocked wind regions. Although the volume of the starburst region is small compared to regions of hot or very hot gas in the free or shocked wind, the density of the very hot gas in the starburst region is significantly higher than that of the very hot gas elsewhere in the wind.

Hard X-ray luminosities for all the models in the 2.4–15.0 keV band are given in Table 3, and lie in the range $L_{\rm X,hard} = 2 \times 10^{37}$ to 5×10^{39} erg s^{-1}. This is typically 2 orders of magnitude lower than the soft X-ray luminosity of the wind. S94 had already found similarly low ratios of thermal hard to soft X-ray luminosity, so our results are in good agreement with theirs.

Cappi et al. (1999) have argued that the hard X-ray emission from starburst galaxies is from a very hot ($kT = 6$ to 9 keV) diffuse component of the ISM, most likely associated with the starburst-driven wind. Based on *BeppoSAX* observations, they find a ratio of hard X-ray to soft X-ray luminosity (in the 2–10 keV band relative to the 0.1–2 keV energy band) of ~4 for M82 and ~2 for NGC 253. This is totally inconsistent with the ratio of $\sim 10^{-2}$ we and S94 have found for diffuse thermal emission from starburst-driven winds.

Non-thermal processes associated with starburst-driven winds may well increase the total hard diffuse X-ray emission from starbursts. Moran & Lehnert (1997) attribute the hard X-ray emission from the nuclear region of M82 to inverse-Compton emission from IR photons scattered off relativistic electrons. This process is less likely to be important for generating hard X-ray emission in the halo (Seaquist & Odegard 1991). An imminent solution to these uncertainties is at hand, as *Chandra* observations of local starbursts will have the spatial and spectral resolution necessary to determine the physical origin of the hard X-ray emission.

We therefore reiterate and emphasize S94's conclusion that *the hard X-ray emission from starburst galaxies is not due to thermal emission from the starburst-driven wind.*

3.2.3 *Phase distribution and filling factor of the X-ray-emitting gas*

In almost all of the models we find that hot gas fills the majority of the volume of the wind (see the hot gas filling factor $\eta_{\rm hot}$ in Table 3). The exception is the centrally mass-loaded model tbn_6, where warm and hot gas fill approximately equal fractions of the wind volume.

Although the distribution of gas volume can always be approximated by a broadly peaked function of temperature, centred at a temperature of $kT \sim 0.5$ to 1 keV, it would be an over-simplification to say that gas at any one temperature fills the majority of the wind.

While the temperature of the gas that fills the majority of the wind volume is similar to those derived from fitting simple spectral models to *ROSAT* and *ASCA* spectra of diffuse X-ray

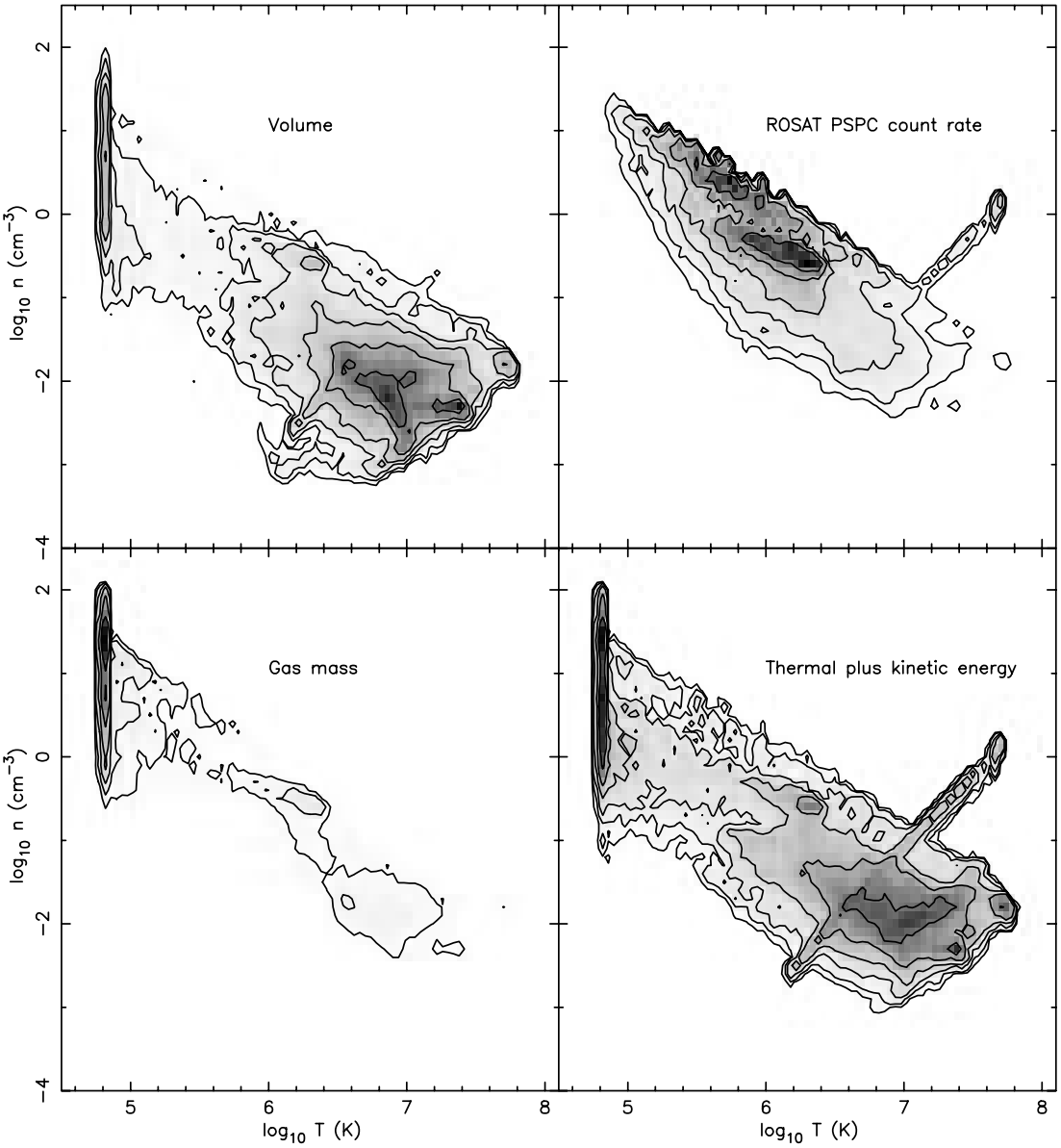

Figure 12. The distribution of volume, soft X-ray emission (*ROSAT* PSPC count rate), gas mass and total energy (thermal plus kinetic) as a function of gas temperature and density within the wind in model tbn1b at $t = 7.5$ Myr, binned logarithmically in temperature and density. The intensity scale has been normalized to the peak value in each panel. Contours begin at 0.1 per cent of the peak intensity, and increase in 0.5 dex intervals up to 31.6 per cent. Note that the locus of maximum X-ray emission is not the same as the locus of maximum volume, mass or energy – the X-ray emission comes from low volume-filling factor gas, containing a relatively small fraction of the total mass and energy content of the galactic wind. The starburst region and the initially adiabatically expanding wind (for which $T \propto n^{2/3}$) produce the ridge running from ($\log T = 7.8$, $\log n = 0$) to ($\log T = 6.2$, $\log n = -2.5$) in the X-ray emission and energy diagrams. The use of a minimum allowed temperature leads to the spike of material at $\log T = 4.8$, which contains the majority of the total mass in the wind.

emission from starburst galaxies, *almost all of the intrinsic soft X-ray emission comes from cooler denser low filling factor gas*. The hot gas filling most of the volume contributes only a small fraction of the soft X-ray emission of the wind. This is true of all the models we have explored.

As an example of this, we show the distribution of gas volume and X-ray emission (detectable *ROSAT* PSPC count rate in the absence of absorption, so as to include the energy-dependent sensitivity of the PSPC) as a function of the gas temperature and number density from model tbn1b at $t = 7.5$ Myr in Fig. 12. It is clear that most of the X-ray emission comes from higher pressure ($P/k \sim 10^6$ K cm^{-3}), denser and slightly cooler, material than the gas that fills the majority of the volume (which has $P/k \sim 10^5$ K cm^{-3}).

Just as the most X-ray-luminous gas does not occupy much of the total wind volume, neither does it contain much of the mass and energy (either thermal or kinetic) of the wind (see Fig. 12).

The exact filling factors and mass and energy fractions depend on what we define the majority of the X-ray emission to mean. Clearly, the hot gas filling most of the volume does emit soft X-rays at some level. Table 4 shows the percentage of the total gas mass, volume and energy in model tbn1b as a function of the fraction of the total unabsorbed *ROSAT* PSPC count rate it is responsible for, from the 50 per cent to the 95 per cent levels.

Table 4. Fraction of the total wind mass, volume and energy content in the gas contributing most to the intrinsic X-ray emission (in the *ROSAT* PSPC band) from model tbn1b at $t = 7.5$ Myr. The most X-ray-luminous gas occupies a small fraction of the wind volume, and contains little of the mass and energy of the outflow. For example, 95 per cent of the X-ray emission is produced by only 2.4 per cent of the wind's mass, occupying only 1.5 per cent of the total volume.

	Fraction (%)			
X-ray emission	50	75	90	95
Mass	0.17	0.38	0.83	2.40
Volume	0.08	0.34	0.78	1.45
Thermal energy	0.69	2.21	5.04	7.93
Kinetic energy	0.62	2.18	5.02	10.42

Table 5. Fractions of the total wind mass, volume, thermal and kinetic energy in the gas that produces the most luminous 90 per cent of the intrinsic X-ray emission in the *ROSAT* PSPC band (see Section 3.2.3). In all models the X-ray-dominant gas is of low volume-filling factor, and allows us to probe only a small fraction of the mass and energy content of the wind.

Model	$f_{\rm M}$ (%)	η ($f_{\rm V}$) (%)	$f_{\rm TH}$ (%)	$f_{\rm KE}$ (%)
tbn_1	0.51	0.09	1.89	4.93
tbn1a	1.08	0.79	4.36	5.62
tbn1b	0.83	0.78	5.04	5.02
tbn_2	0.05	0.01	0.19	8.09
tbn_6	0.38	0.02	2.91	4.58
tbn_7	0.12	0.01	0.53	2.02
tbn_9	0.99	0.14	7.11	9.62
mnd_3	2.21	1.61	4.24	12.76
mnd_4	0.82	2.37	5.10	21.42
mnd_5	0.35	0.02	1.81	3.49
mnd_6	0.08	0.003	0.11	0.12
mnd_7	0.63	0.40	2.85	2.53

Even if we consider 95 per cent of all the X-ray emission, we are only sampling just over 1 per cent of the wind volume, 2 per cent of the total mass, and 10 per cent of the energy of the wind!

Note that although the fraction of the total mass in the X-ray-dominant gas is small, there is relatively little mass in the warm and hot phases to begin with. For example, in model tbn1b only ~8 per cent of the total mass is in gas with $T \geq 10^{5.5}$ K (Table 3). The X-ray-dominant gas in this model contains about ~0.8 per cent of the total mass, so X-ray observations would be probing of order 10 per cent of the mass of the warm and hot gas.

In all of the models we have run, the gas contributing the majority of the intrinsic soft X-ray emission comes from a very small fraction of the wind. Table 5 shows the filling factors, mass and energy fractions of the gas dominating the intrinsic soft X-ray emission in all models, at a typical epoch once a full galactic wind has developed ($t = 7.5$ Myr). The lowest filling factors in Table 5, of order 10^{-2} per cent, may be numerical artefacts due to limited numerical resolution. This is discussed further in Section 4.

Nevertheless, it is clear that soft X-ray observations probe only a minor fraction of the wind, whether measured in terms of total volume, energy content, total mass or even mass of warm/hot gas.

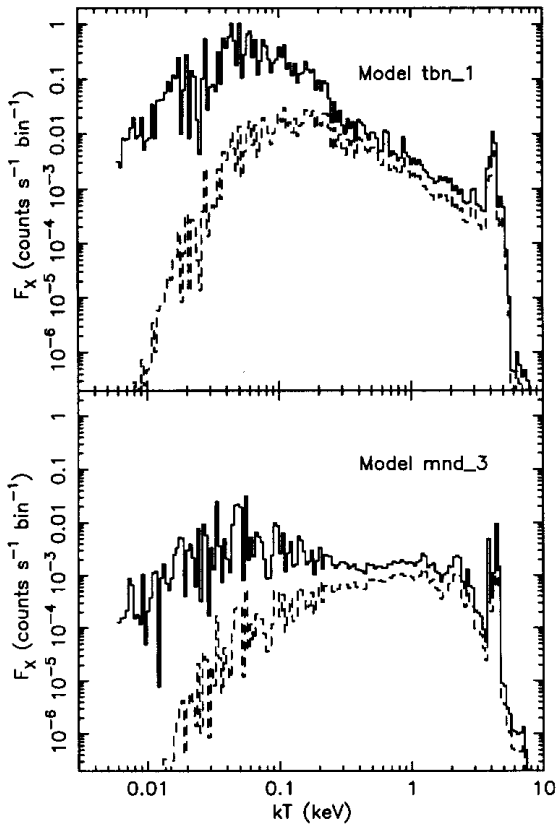

Figure 13. The contribution from gas at each logarithmic temperature bin to the total *ROSAT* PSPC count rate in models tbn_1 and mnd_3 at $t = 7.5$ Myr, assuming no absorption (solid line) and $N_{\rm H} = 4 \times 10^{20}$ cm^{-2} (dashed line). A very wide range of gas temperatures is responsible for the emission that would be detected by the *ROSAT* PSPC, even allowing for a realistic amount of absorption.

3.2.4 *Temperature distribution of the X-ray-emitting gas*

From Fig. 12, which is typical of the temperature–density distributions found in all of these models, it is clear that gas at a wide range of temperatures and densities contributes to the X-ray emission in the *ROSAT* band. In Fig. 13 we show the contribution from gas at each logarithmic temperature bin to the total *ROSAT* PSPC count rate in models tbn_1 and mnd_3 (the default thick- and thin-disc galactic wind models). Even when the effect of realistic intervening absorption is included, the PSPC would detect photons from a very wide range of gas temperatures.

Is this consistent with existing X-ray data on the hot gas in galactic winds? As a first-order approximation to a characteristic X-ray temperature for these models we have calculated the average gas temperature $T_{\rm PSPC}$, which has been weighted by the *ROSAT* PSPC count rate (see Table 6). This assumes no absorption, or that given an observed X-ray spectrum we could correct for any absorption to obtain the true temperature distribution of the emitting gas.

These temperatures range from $T_{\rm PSPC} = 0.08$ to 0.55 keV, similar if slightly lower than single-temperature fits to *ROSAT* PSPC spectra of galactic winds. For example, Strickland et al. (1997) find best-fitting temperatures ranging between 0.3 and 0.7 keV in M82's wind, and Dahlem et al. (1998) find $kT \approx 0.1$ to 0.7 keV in NGC 253's wind. Note that the characteristic temperatures in Table 6 are not the result of fitting spectral

Table 6. Average gas temperature in each of the models at $t = 7.5$ Myr (weighted by *ROSAT* PSPC count rate, and ignoring absorption), and a qualitative description of what region the majority of the soft X-ray emission originates in.

Model	$T_{\rm PSPC}$ (keV)	SB[a]	FW[b]	IR[c] w/d	IR[c] w/c	SH[d]
tbn_1	$0.09^{+0.20}_{-0.04}$			yes	yes	
tbn1a	$0.11^{+0.26}_{-0.05}$			yes	yes	
tbn1b	$0.13^{+0.27}_{-0.06}$			yes	yes	
tbn_2	$0.07^{+0.15}_{-0.03}$			yes	yes	
tbn_6	$0.21^{+0.27}_{-0.14}$	yes		yes		
tbn_7	$0.08^{+0.24}_{-0.03}$			yes	yes	
tbn_9	$0.16^{+0.21}_{-0.09}$			yes	yes	
mnd_3	$0.44^{+0.89}_{-0.33}$	yes	yes	yes	yes	yes
mnd_4	$0.35^{+0.42}_{-0.20}$	yes		yes	yes	yes
mnd_5	$0.55^{+0.23}_{-0.25}$	yes	yes	yes		
mnd_6	$0.14^{+0.65}_{-0.10}$			yes		
mnd_7	$0.19^{+0.40}_{-0.10}$	yes		yes		

[a] The starburst region.
[b] The freely expanding wind of SN and stellar wind ejecta.
[c] Interface regions, either between the wind and the ISM of the galactic disc (w/d) or between the wind and clumps of disc ISM entrained into the wind, such as superbubble shell fragments (w/c).
[d] Shocked halo gas.

models to observed spectra. Nevertheless, they are in broad agreement with the observed characteristic soft X-ray temperatures of galactic winds.

Although fitting simple spectral models (such as one- or two-temperature thermal plasma models) to simulated *ROSAT* or *ASCA* X-ray spectra from these models does give statistically good fits (as we shall show in Paper II), the derived plasma properties are misleading. We urge caution in interpreting spectra of hot gas in starburst galaxies, observed with either the preceding generation of X-ray telescopes (*ROSAT* or *ASCA*) or the latest generation (*Chandra* or *XMM*).

Very broad-band sensitive X-ray spectroscopy of the hot gas in these outflows should show more evidence of the complex temperature structure than current *ROSAT* or *ASCA* spectroscopy (where the existing broad-band coverage is compromised by source confusion and limited sensitivity). The simulated X-ray spectra for models tbn_1 and mnd_3 at $t = 7.5$ Myr are shown in Fig. 14. Note that both are softer and harder than the spectrum of a $kT = 0.5$ keV thermal plasma, reflecting the wide range of temperatures in the gas in these winds.

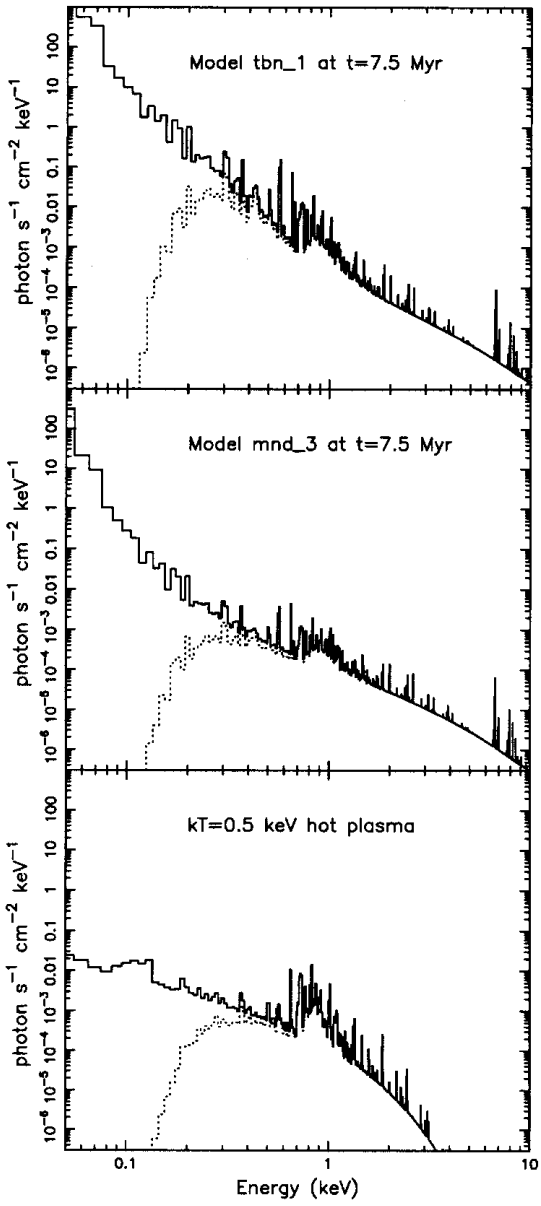

Figure 14. Intrinsic X-ray spectra for models tbn_1 (top) and mnd_3 (bottom) at $t = 7.5$ Myr, shown in comparison to the X-ray spectrum for a hot plasma of temperature $kT = 0.5$ keV (bottom panel, similar to the temperature of the hot gas in starburst galaxies inferred from X-ray observations). The dotted lines show the same spectra after absorption by a hydrogen column of $N_{\rm H} = 4 \times 10^{20}$ cm^{-2} (equivalent to the Galactic hydrogen column towards M82).

3.3 Physical origin of the soft X-ray emission

As discussed in Section 1, the origin and properties of the X-ray-emitting gas in galactic winds is unclear. S94 had concluded that the majority of the soft X-ray emission in their four models came from disc and halo gas shock-heated by the wind. Recently, D'Ercole & Brighenti (1999) argued that the soft X-ray emission in these models was not shock-heated disc or halo gas, but was from warm gas in the numerically broadened interfaces (i.e., artificially smoothed-out contact discontinuities) between cool dense gas and the hot wind.

In all likelihood, a mixture of these two effects are responsible for the X-ray emission in these previous models, but it is very difficult to separate the two effects. Regions of ambient ISM shock-heated by the wind are also unavoidably interfaces between dense cool gas and hot tenuous gas, which will be artificially smoothed out over a number of computational cells (the exact number of which depends on the hydrodynamical scheme used; see Fryxell, Müller & Arnett 1991 for a comparison of different codes, which shows the PPM-based codes that S94 and ourselves have used in a favourable light!).

Without performing much higher resolution simulations it is difficult to assess the relative significance of these two effects. See Section 4 for a more detailed discussion of the effect of numerical resolution and numerical artefacts, as well as a comparison between the models we have run at increasing resolution.

To avoid a premature choice between shock-heating of clouds and the numerical broadening of contact discontinuities as the dominant source of the soft X-ray emission in these simulations, we shall refer to 'the interaction of the wind with cool dense gas.' X-ray emission from such interaction regions could then come from one or more of any number of processes: in our numerical simulations shock-heating and numerically broadened contact discontinuities, and in reality shock-heating, conductive or photo-evaporative interfaces, or turbulent mixing layers (Begelman & Fabian 1990).

If we pick out the most X-ray-luminous regions within the wind, i.e., those regions responsible for the most luminous 90 per cent of the soft X-ray emission, we can find the physical origin of this emission. As we have run a wider range of models than S94 or D'Ercole & Brighenti (1999), and have included mass-loading (another process leading to soft X-ray emission), this exercise is of some interest.

We have already shown above that the soft X-ray emission comes from low filling factor gas, $\eta \sim 10^{-2}$ to $\sim$2 per cent. We find that in all the models interaction regions (as defined above) are responsible for some, and in a few cases, all of the soft X-ray emission.

It is important to note that such interface regions do not always dominate the X-ray emission. We provide a qualitative description of which regions within the wind are responsible for the most luminous 90 per cent of the soft X-ray emission in Table 6.

In the mass-loaded models tbn_6, mnd_5 and mnd_7 the starburst region itself is a source of significant X-ray emission in the *ROSAT* band. This is easily understandable in the centrally mass-loaded models tbn_6 and mnd_5, where the central gas densities in the starburst region are an order of magnitude higher due to the additional mass injection and lower outflow velocity.

Without additional mass-loading we would not normally expect the starburst region or free wind regions to be significant sources of X-ray emission, due to the low density (cf. CC). Nevertheless, the total X-ray luminosities of models mnd_3 and mnd_4 are so low (see Table 3 or Fig. 10) that these regions are counted as being X-ray-dominant. Shocked halo gas is also important in these two models. The thickness of the shell of swept-up and shocked halo gas is large enough that there is no problem of unresolved contact discontinuities, as this shell is very well resolved in all the models. These models are so X-ray-underluminous compared to M82 (see Table 3 or Fig. 10) that it is unlikely they are good models of M82's wind itself.

When interface regions and shock-heated halo gas dominate the soft X-ray emission of galactic winds, abundance determinations based on X-ray spectroscopy will reflect the metallicity of the ambient disc and halo ISM to a significant degree. This is the same conclusion as reached by D'Ercole & Brighenti (1999). As a result, it seems unlikely that we can directly probe the metal-enriched gas in these winds with X-ray observations, which will make it difficult to measure the metal ejection efficiency of such outflows directly.

3.4 Wind energy and mass transport

The distribution of thermal and kinetic energy within conventional wind-blown bubbles and superbubbles has been discussed in the literature (see Mac Low & McCray 1988 and Weaver et al. 1997), but the energy distribution within galactic winds has not been addressed until now. As galactic winds are, by definition, bulk outflows, their 'energy budget' can differ substantially from the energy distribution within superbubbles.

In what form (i.e., thermal or kinetic) is the energy within the wind stored, in which gas phases, and does this depend on time, position within the wind and on the starburst or ISM? What fraction of the wind's energy is transferred to the swept-up ISM? Which, if any, components of the wind have sufficient energy to escape the host galaxy completely? How efficient is the wind at transporting energy into the IGM?

The answer to the final question has important cosmological consequences. Galactic winds may be important for the heating of the ICM in galaxy groups and clusters (e.g. Ponman et al. 1999) and the IGM, but without knowing what fraction of the total wind energy budget can be observed in a particular waveband (e.g. soft X-ray emission, or observations of the optical emission-line gas) it is difficult to assess the impact of galactic wind heating.

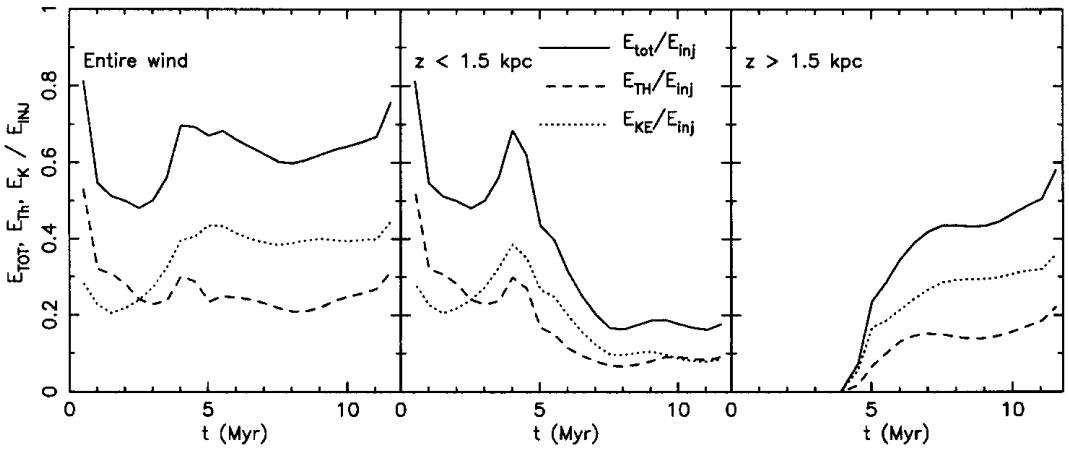

Figure 15. The energy content of the wind in model tbn_1 as a function of time. Each of the three panels show the total (thermal plus kinetic energy, solid line), thermal (dashed line) and kinetic energy (dotted line) content of the wind as fractions of the total energy injected into the wind by the starburst. The three panels show the energy fractions within the entire wind, the energy fractions of the wind within the plane of the galaxy ($|z| \leq 1.5$ kpc), and the energy fractions of the wind within the halo ($|z| > 1.5$ kpc). Initially dominated by thermal energy, post-blowout kinetic energy dominates the energy budget of the wind. Note that the wind is an efficient mechanism of transporting energy into the halo.

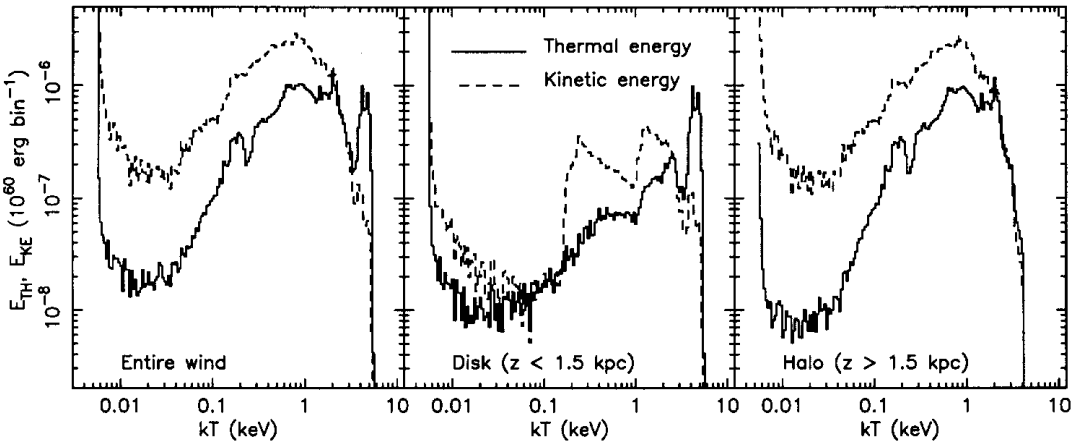

Figure 16. Temperature distributions of thermal (solid line) and kinetic (dashed line) energy in model tbn1b at $t = 7.5$ Myr. The three panels show the energy within the entire wind, the energy within wind material still in the plane of the galaxy ($|z| \leq 1.5$ kpc), and the energy of the wind in the halo ($|z| > 1.5$ kpc) as a function of gas temperature. The majority of the thermal and kinetic energy of the wind is in hot, $kT \sim 0.1$ to 2.0 keV, gas expanding out into the halo.

3.4.1 Wind energy budget and energy transport

In the standard model of a wind-blown bubble or superbubble (Weaver et al. 1977) expanding into a uniform density medium, the majority of the energy is in the thermal energy of the shocked wind region. Of the total mechanical energy injected, ~45 per cent is thermal energy in the hot shocked wind, ~20 per cent is in the form of the kinetic energy in the cool dense shell and the majority of the remaining ~35 per cent has been radiated away, primarily from the shell.

We find that blowout of the superbubble from the disc changes the energy balance of a galactic wind, from being dominated by thermal energy, to being dominated by kinetic energy (Fig. 15). In the thick-disc models this can clearly be seen occurring at $t \sim 3$ Myr. Blowout in our thin-disc models is almost instantaneous, and they become kinetic energy-dominated within ~0.5 Myr.

Decomposing the energy budget into disc ($|z| \leq 1.5$ kpc) and halo ($|z| > 1.5$ kpc) components reveals that invariably the majority of the energy injected by the starburst is transported out of the disc and into the halo (a single example using model tbn_1 is shown in Fig. 15). The total energy within the disc remains approximately constant after $t \sim 5$ Myr, but this is a decreasing fraction of the total energy injected by the starburst.

In superbubbles the thermal energy is in predominantly in the hot ($T \geq 10^6$ K) bubble interior, and the majority of the kinetic energy is in the cool ($T \sim 10^4$ K) dense shell. In what temperature gas is the energy of a galactic wind stored?

In most of the models the majority of both the thermal and kinetic energy outside the plane of the galaxy ($|z| > 1.5$ kpc) is in hot gas [$6.5 \leq \log T(\mathrm{K}) \leq 7.5$], with relatively little thermal or kinetic energy in cool gas [$4.5 \leq \log T(\mathrm{K}) \leq 5.5$]. This can be seen in Fig. 16, which shows the temperature distribution of the thermal and kinetic energy, over the entire wind and decomposed into disc and halo components, from model tbn1b. Table 3 gives the fractions of the total thermal or kinetic energy in the warm and hot phases of the wind in all the models.

It is interesting to note that a large fraction of the total energy of the wind is in gas that can, *in principle*, be probed with X-ray absorption-line studies, where the relative dominance of denser X-ray-emitting gas is reduced. Such absorption-line studies would require bright X-ray sources in the background behind a galactic wind, and a combination of high sensitivity and spectral and spatial resolution.

In the centrally mass-loaded thick-disc model tbn_6, there is very little hot gas [$6.5 \leq \log T(\mathrm{K}) \leq 7.5$]. Instead, the thermal energy is predominantly in warm gas [$5.5 \leq \log T(\mathrm{K}) \leq 6.5$], while the kinetic energy of the wind is evenly spread between warm and cool gas.

Distributed mass-loading (models tbn_9 and mnd_7) differs from central mass-loading in not having such an strong effect on the energy–temperature distributions, and these models are quite similar to the non-mass-loaded models in terms of energetics.

In the weak starburst models, such as tbn_2 and mnd_4, thermal energy begins to dominate the total energy budget again after $t \sim 7.5$ Myr. This is due to the thermal energy of the halo gas swept-up being a significant fraction of the total energy injected by the starburst in these models. In more powerful starburst models the energy content of the disc and halo ISM overrun by the wind is insignificant.

In all models the wind is efficient at transporting energy out of the plane of the galaxy, and as the winds are generally inefficient at radiating this energy away, galactic winds can in principle be good sources of heating for the IGM.

3.4.2 Mass transport and ejection

Although the starburst can sweep up and shock large masses of ambient gas ($\lesssim 10^2\times$ the total mass of SN ejecta), most of this mass is in, and remains in the plane of, the galaxy (see Fig. 17). Only a small fraction of the total mass can be found at heights above $z = 1.5$ kpc from the plane. Galactic winds of power similar to M82's are *inefficient at transporting gas out of the plane of the galaxy.*

Note that the total mass of metal-enriched gas injected by the starburst is significantly smaller than the total mass of wind material that is transported out of the disc. If all of mass associated with wind that is transported out of the disc were to make its way into the IGM, then on average gas injected into the IGM by galactic winds would not be highly metal-enriched.

We cannot quantitatively assess the long-term fate of the material in our simulations, given the necessarily limited spatial and temporal domain of these high-resolution simulations. We can quantify what fraction of the mass of the wind currently has

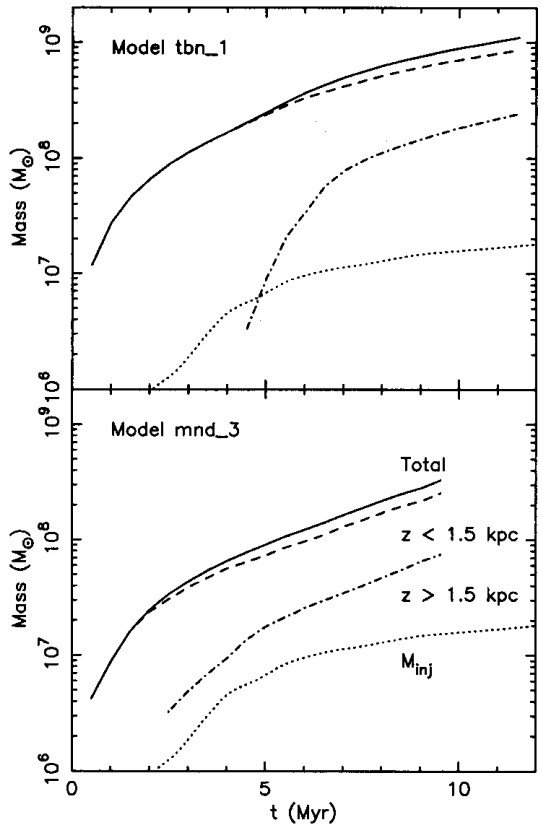

Figure 17. Wind mass as a function of time in models tbn_1 and mnd_3 (solid line), compared to the total mass of gas injected by the starburst (dotted line). The wind masses within the plane of the galaxy ($|z| \leq 1.5$ kpc, dashed line) and above the plane ($|z| > 1.5$ kpc, dot-dashed line) are also shown. The mass of enriched material injected by the starburst ($M_{\rm inj}$) is always small compared to the mass of disc and halo gas swept-up by the wind. Note that the majority of the gas in the 'wind' remains in the plane of the galaxy – galactic winds are relatively inefficient at removing gas from the galaxy.

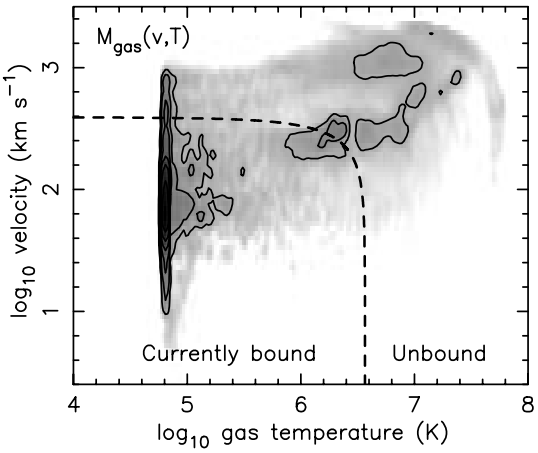

Figure 18. Mass in model tbn1b at $t = 7.5$ Myr, as a function of gas temperature and velocity. Gas above and to the right of the dashed line *currently* has sufficient total energy to escape the galaxy entirely, based on an escape velocity for M82 of $v_{\rm esc} = 390\,{\rm km\,s^{-1}}$. Only a mass of $4 \times 10^7\,{\rm M_\odot}$ out of a total gas mass of $5 \times 10^8\,{\rm M_\odot}$ is unbound. A logarithmic intensity scale has been used to display both the cool gas dominating the total mass and the hot but tenuous energetic gas.

energy sufficient to escape the gravitational potential of the galaxy at any particular epoch. The distribution of gas mass as a function of temperature and velocity in model tbn1b at $t = 7.5$ Myr is shown in Fig. 18. Several broad conclusions can be drawn from this figure.

(i) Most of the wind's mass is in cool gas, expanding at $v \lesssim 100\,{\rm km\,s^{-1}}$. This represents the slow expansion of the wind within the plane of the galaxy, where the majority of the mass is swept-up.

(ii) Assuming conservatively that the escape velocity $v_{\rm esc}$ from M82 is $v_{\rm esc} \sim 3 \times v_{\rm rot} \sim 390\,{\rm km\,s^{-1}}$ (see, for example, the arguments in Heckman et al. 2000, and M82's rotation curve in Fig. 1), then only gas above and to the right of the dashed line in Fig. 18 *currently* has sufficient total energy to escape the galaxy. This gas is only 8.0 per cent ($\sim 4 \times 10^7\,{\rm M_\odot}$) of the total mass associated with the wind.

(iii) Interactions between the hot, energetic SN-ejecta phases of the wind and the ambient ISM has swept up and accelerated $\sim 6 \times 10^6\,{\rm M_\odot}$ of cool gas ($T \lesssim 10^5$ K) up to velocities in the range $400 \leq v \lesssim 1000\,{\rm km\,s^{-1}}$.

(iv) The concentration of mass at $\log T \sim 4.8$ is due to minimum temperature allowed in these simulations. The distribution and dynamics of mass at temperatures lower than this limit is unknown, so the results above may overestimate the mass of gas with energy sufficient to escape. Note that even these high-resolution simulations ($\Delta x = 4.9$ pc) do not have the numerical resolution necessary to resolve the structure and dynamics of gas cooler than this limit (see the discussion in Section 4.3), so there is little point in simulations with lower temperature limits that do not have significantly enhanced numerical resolution.

(v) Using the temperature of the X-ray-emitting gas in starbursts to assess if this gas can escape the host galaxy (the so-called 'escape temperature'; e.g. Wang et al. 1995; Martin 1999) will underestimate the mass of gas that can escape, as it neglects the motion of the hot gas. As discussed in Section 3.4.1, most of the energy in a galactic wind is in the kinetic energy of hot gas.

(vi) Assessing what mass of gas can escape a galaxy in the long term, based on some measure of gas energy or velocity at a particular epoch, seems extremely difficult. As the wind evolves, the hot energetic gas within it will continue to entrain and accelerate cold gas. A major unknown is the effect of any halo medium (as assumed in these simulations), which acts to impeded and decelerate the wind's expansion. Given a dense enough halo environment, none of the material in a galactic wind might escape into the IGM. Treating this problem numerically is challenging, given that it requires high numerical resolution to resolve the interaction between cloud and wind, as well as including the physics important to wind/cloud interactions (e.g., hydrodynamic stripping of clouds, thermal conduction, maybe even magnetic fields?).

To summarize: (a) the mass of gas that can escape the galaxy in a starburst-driven wind is low (perhaps a few times $10^7\,{\rm M_\odot}$ in a moderate starburst such as M82's), and (b) winds are inefficient at transporting the ISM out of galaxies. These results are qualitatively consistent with those of Mac Low & Ferrara (1999) or D'Ercole & Brighenti (1999), although the outflows we have considered are 2.0–3.5 orders of magnitude more powerful than the winds of those authors.

4 PHYSICAL AND NUMERICAL LIMITATIONS

A very important aspect of any numerical hydrodynamical simulation is the degree to which the finite amount of physics included and numerical limitations (in particular, finite resolution) influence the results. Understanding these effects is difficult for even the specialist, let alone for the general astronomer.

We think it is important for readers to understand the basic problems that can and do affect these and other hydrodynamical simulations. Without an understanding the limitations of a simulation it is difficult to judge what results are real and what are not. We shall discuss qualitatively the effect and importance of some of the physics that is not included in these simulations. Numerical artefacts, in particular those related to resolution and numerical diffusion, are then discussed in some detail. Finally, we present a comparison between three models designed to study how the simulated properties of the hot gas in galactic winds varies as we increase the numerical resolution.

4.1 Missing physics

4.1.1 Using effective instead of true gravitational potentials

The use of an effective potential $\Phi_{\rm eff}$ and the resulting effective gravity $\boldsymbol{g}_{\rm eff}$ to maintain the ISM in hydrostatic equilibrium are artefacts of a 2D approach. A 3D code would incorporate the azimuthal velocity component without altering the gravitational field. 3D simulations would require significant increases in terms of computation resources and code development, and are difficult to justify, given that the potential scientific return of 2D simulations has barely been tapped.

The use of a centrifugal potential means that the gravitational force felt by material within the galactic wind will be different from the true gravitational force it should feel. Put another way, the effective gravitational force in these simulations has been tuned to hold the ISM in its initial distribution, given the assumption that at any position (r, z) its rotational velocity v_ϕ around the z-axis and hence angular momentum is known a priori. The problem is how to treat the material within the galactic wind, given that it is a mixture of material flowing outward from the central starburst region and ambient ISM swept up and entrained into the flow. Hot gas from the starburst region itself can be presumed to have almost zero angular momentum, given its origin at the centre of the galaxy and the violent dynamics of the gas. As it flows radially and vertically outward in these 2D simulations, it feels the effective, i.e., modified by assumed rotation, gravitational force, whereas it should feel only the true gravitational force.

What effect does this have on the dynamics of the material within the wind? The effect on the very energetic free wind or shocked wind gas is negligible, as the terminal velocity of this gas is $v_\infty \sim 3000\,{\rm km\,s^{-1}}$, so it hardly feels the gravitational field of the galaxy. The main area where problems may arise is that the dynamics and long-term evolution (over hundreds of Myr) of the dense disc material dragged out of the disc and entrained into the flow (and which is assumed to be associated with the optical emission lines observed in local starbursts such as M82) may well be distorted, given that typical velocities for this gas are only several hundred kilometres per second.

As a very rough estimate of the magnitude of the force required to significantly affect the dynamics of material within the galactic wind, a final velocity of $500\,{\rm km\,s^{-1}}$ (a velocity slightly greater than the escape velocity and also significant in terms of the dynamics and morphology of the denser gas within the wind) after 10 Myr of constant acceleration requires an acceleration of $\approx 1.5 \times 10^{-7}\,{\rm cm\,s^{-2}}$. As the difference between the true and effective gravitational fields for the thick-disc ISM model is typically one-tenth of this value, we can conclude that the use of an effective gravitational field does not lead to a major distortion of the wind dynamics over the time-scales of the simulations we are interested in.

4.1.2 Non-ionization equilibrium

The hot plasma emissivities used to calculate the radiative cooling and X-ray emission from these models assume the gas is in collisional ionization equilibrium (CIE).

For a suddenly heated plasma, the time required to reach ionization equilibrium is approximately $t_{\rm ieq} \approx 0.03 n_{\rm e}^{-1}\,{\rm Myr}$ (Masai 1994) for a range of the important elements. The density and temperature structure within the wind is complex, but typical electron densities in the gas dominating the X-ray emission are of order $n_{\rm e} \sim 0.3\,{\rm cm^{-3}}$, implying an ionization time-scale of $t_{\rm ieq} \sim 0.1\,{\rm Myr}$. Though much shorter than the typical age of the wind, $t \sim 10\,{\rm Myr}$, the complex dynamical state within the wind probably means it is rare that the conditions of any parcel of gas remain unchanged for this amount of time. For example, gas returned to the ISM by a SN in the starburst region is shocked within the starburst region to $T \sim 10^8\,{\rm K}$, then flows out of the starburst region in a $v \sim 3000\,{\rm km\,s^{-1}}$ wind which rapidly adiabatically cools, before passing through the reverse shock after $\lesssim 1\,{\rm Myr}$ and being reheated to $T \sim 10^8\,{\rm K}$.

Much of the soft X-ray emission within a galactic wind will be due to initially cool gas incorporated into the wind, e.g., swept-up and shock-heated ISM, cool gas mixed into the hot wind by conduction or mass-loading and instabilities (see Section 3.3). The ionization state of this gas will lag behind its temperature rise, as discussed by Weaver et al. (1977). Metal ions that in CIE contribute significantly to the X-ray emission of plasmas with $T \sim 10^6\,{\rm K}$ will in practice be underionized. In general, then, the true X-ray luminosity will be less than that obtained assuming CIE.

For a rapidly cooling plasma, for example, the adiabatically expanding free wind or some similar region of expansion, the gas will be overionized with respect to its thermal temperature. The emissivity of this gas will be less than that of a gas in CIE.

As a result of the complex ionization histories of the gas within the wind, it is difficult to quantify how non-ionization equilibrium (NIE) effects would alter the properties of the wind from the CIE case we assume. Calculating the ionization state of the gas in these simulations would require tracking the history of individual parcels of gas, and would be prohibitively expensive computationally.

Given that the majority of observational analysis of real X-ray spectra assumes CIE in using the Raymond–Smith or MEKAL plasma codes, assuming CIE in creating artificial X-ray spectra does not seem too unrealistic. Systematic biases in standard X-ray spectral fitting discovered in studying the artificial X-ray observations of these wind simulations will only underestimate the true biases of fitting complex, NIE X-ray spectra with simple CIE spectral models.

4.1.3 Magnetic fields and cosmic rays

These simulations, along with the previous work of TI, TB, S94,

S96 and Tenorio-Tagle & Muñoz-Tuñón (1997), ignore both cosmic rays and magnetic fields, instead focusing on a totally hydrodynamic model of galactic winds. One of the aims of this work is to see if such pressure-driven winds can reproduce the observed properties (primarily based on X-ray observations) of the best-studied galactic wind in M82.

Magnetic fields and cosmic rays are known be present within the wind, but studying them is difficult and the results somewhat uncertain. Magnetic fields may be important in galactic winds over large and/or small scales. Large-scale fields (over hundreds or thousands of parsecs) could potentially alter the general dynamics and expansion of the wind, for example confining its expansion in the plane of the galaxy or maybe acting to collimate it (see Sections 3.1.3 and 3.1.4). Even if magnetic fields are not important on such large scales, any smaller scale fields associated with the clouds and clumps of ambient ISM entrained into these winds could well be important. Such small-scale fields might alter or inhibit the hydrodynamical stripping or conductive evaporation of these clouds, and hence affect the X-ray emission from galactic winds.

We can qualitatively assess the importance of large-scale magnetic fields and of cosmic rays, relative to purely hydrodynamical processes, through comparison between the gas properties in our simulations and the existing observational data (summarized below).

(i) Seaquist & Odegard (1991) estimate that the total energy injection rate into the halo in the form of relativistic particles is $\lesssim 10^{40}\,\mathrm{erg\,s^{-1}}$. Compared to the mechanical energy injection rate from the starburst in these simulations of typically $\sim 10^{42}\,\mathrm{erg\,s^{-1}}$, cosmic rays are energetically unimportant in the halo. Cosmic rays also are unlikely to be an important source of non-thermal X-ray emission from the halo (but might be important within the starburst region itself; e.g. Moran & Lehnert 1997).

(ii) Klein, Wielebinski & Morsi (1988) estimate a magnetic field strength of $B \sim 50\,\mu G$ within the central $650 \times 200\,\mathrm{pc}^2$ starburst region, based on the assumption of equipartition.

(iii) A rotation measure analysis by Reuter et al. (1994) gives a more direct estimate of the field strength $B \sim 10\,\mu G$ (modulo uncertainties in the column density of ionized gas), at one position at the periphery of the main Hα emission, about 1 kpc to the south-west of the nucleus.

Are fields of this range in strength dynamically important? Could such high field strengths in the starburst region constrict and confine the expansion of the wind in the plane of the galaxy? Comparing magnetic pressure ($P_\mathrm{B} = B^2/8\pi$) to thermal and ram pressures within the wind provides a simple basis for comparison. A magnetic field strength of $B = 50\,\mu G$ corresponds to $P_\mathrm{B}/k \sim 8 \times 10^5\,\mathrm{K\,cm^{-3}}$, and a field of $B = 10\,\mu G$ to $P_\mathrm{B}/k \sim 3 \times 10^4\,\mathrm{K\,cm^{-3}}$.

In the plane of the galaxy, where confinement of the wind's expansion is such a problem, typical thermal and ram pressures are $P_\mathrm{TH}/k \sim 2 \times 10^6\,\mathrm{K\,cm^{-3}}$ and $P_\mathrm{RAM}/k \sim 7 \times 10^6\,\mathrm{K\,cm^{-3}}$ for the powerful starbursts we have simulated (e.g., tbn1b, mnd_3). At a height of $z = 1\,\mathrm{kpc}$ above the plane of the galaxy, pressures are typically lower ($P_\mathrm{TH}/k \sim 10^6\,\mathrm{K\,cm^{-3}}$, $P_\mathrm{RAM}/k \sim 2 \times 10^6\,\mathrm{K\,cm^{-3}}$), but in some locations ram pressures can reach exceedingly high values ($P_\mathrm{RAM}/k \gtrsim 2 \times 10^7\,\mathrm{K\,cm^{-3}}$).

Drawing some tentative conclusions from this, it appears that:

(i) the estimated magnetic field strength of $B \sim 50\,\mu G$ within M82's starburst region, though high by the standards of normal galactic magnetic fields, is still somewhat lower than that required to make the magnetic field dynamically important in confining the expansion of the wind within the plane of the galaxy;

(ii) if large-scale field strengths are typically $B \lesssim 10\,\mu G$ within the wind, then they are dynamically unimportant, but

(iii) if stronger large-scale fields, of order $B \sim 50\,\mu G$, exist throughout the entire wind, then the energy in such magnetic fields would be comparable to, or greater than, the thermal and kinetic energy of the hot gas.

Hence it does not appear that large-scale magnetic fields are dynamically important for understanding this class of galactic-scale outflows. The question of the influence and importance of smaller scale fields in the interaction between the wind and clouds embedded within it remains open.

4.1.4 Thermal conduction

In common with most previous simulations, we ignore thermal conduction, as it difficult to include in multidimensional hydrodynamic schemes and computationally expensive. In the standard wind-blown bubble model of Weaver et al. (1977) evaporation of the cold bubble shell by thermal conduction is the dominant source of mass in the hot bubble interior, increasing its density by approximately an order of magnitude. As a result, the effects of thermal conduction on the X-ray emission from wind-blown bubbles and superbubbles are very important.

In galactic winds, thermal conduction is expected to be important in regions where there are reservoirs of dense cool gas in close proximity to hot gas, such as the interface between the shocked wind and the disc within the plane of the galaxy, or in the vicinity of superbubble shell fragments within the halo.

One effect of thermal conduction is to increase the density of the hot X-ray-emitting gas, in a similar manner to mass-loading. Indeed, Mac Low & Ferrara (1999) add additional mass into their simulations of very weak winds in dwarf galaxies to approximate the effects of conduction in a manner similar to our method of central mass-loading. Our mass-loading can be considered as a rough approximation to the effects of both hydrodynamical mass-loading and thermal conduction, although a rigorous treatment of thermal conduction is beyond the scope of this work.

Thermal conduction, unless inhibited in some manner, might also totally evaporate the cool dense clumps and clouds seen in our simulations. As described in Ferrara & Shchekinov (1993), clouds smaller than the Field length (Field 1965) will suffer rapid conduction-driven evaporation, losing a very substantial fraction of their mass before achieving a semi-stable configuration. For the range of temperatures and densities found in the hot gas filling most of the wind's volume in our simulations, the Field length ranges from several hundred parsecs to several kiloparsecs, so all of the clumps seen in our simulations should suffer conductive evaporation.

The net effect of conduction is difficult even to describe qualitatively. The addition of mass to the hot phases of a galactic wind will increase the X-ray emission from the wind itself, but if conduction destroys clouds totally, then the net effect might be a reduction in total X-ray luminosity, given that cloud/wind interfaces appear to be such strong sources of X-ray emission in these simulations.

Very recently, D'Ercole & Brighenti (1999) have performed a 2D simulation of a starburst-driven wind in a dwarf galaxy (based approximately on the dwarf starburst NGC 1569) that includes

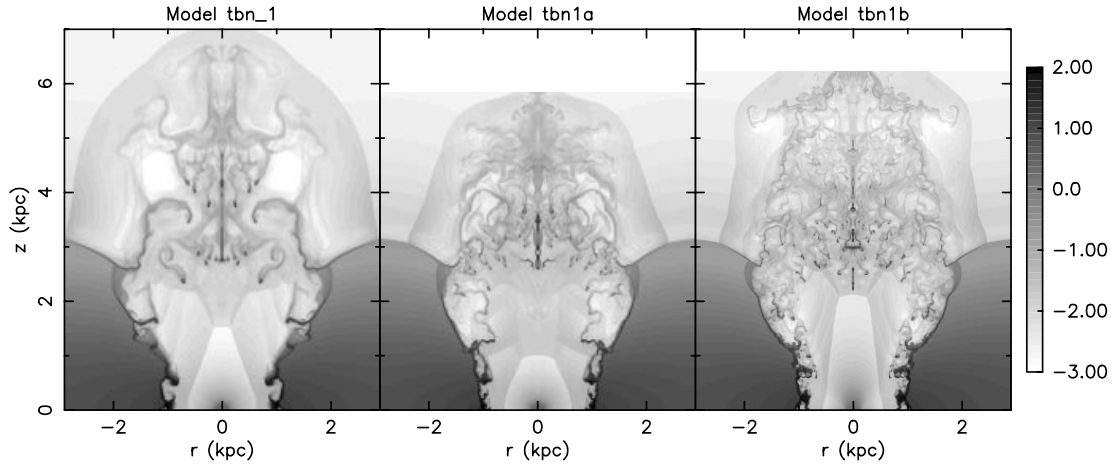

Figure 19. Wind number density distributions for models tbn_1, tbn1a and tbn1b at $t = 7.5$ Myr, shown as grey-scale images of $\log n(\mathrm{cm}^{-3})$. Model tbn1a has twice the resolution of model tbn_1, and model tbn1b 3 times the resolution. Note the dramatic increase in the complexity of the structure of the densest gas as the resolution is increased.

thermal conduction. Interestingly, thermal conduction leads to an increase in the soft X-ray luminosity of this particular model by a factor of between 1 and 3 from the non-conductive case.

4.1.5 Photoionization by the wind

These simulations assume that all material within the wind is optically thin to its own radiation, i.e., there is no absorption intrinsic to the wind. This assumption is necessary to carry out these simulations, as coupled multidimensional radiation-hydrodynamic problems are exceedingly challenging to solve.

For emission from, and propagating through, the hot tenuous material of the wind (e.g., free wind, shocked wind and shocked halo regions) this assumption is reasonable. Typical columns densities of the highly ionized material that would be encountered by radiation traversing the wind are in the range 10^{19}–$10^{20}\,\mathrm{cm}^{-2}$.

In the vicinity of cool dense clouds and the walls of the outflow within the disc, column densities become more significant. Typical column densities traversing a single clump range from $\sim 5 \times 10^{19}$ to $10^{21}\,\mathrm{cm}^{-2}$, depending on whether the line of sight crosses the tail or head of a clump and what the angle of incidence is.

The environment around these cool dense regions is the source of the majority of soft X-ray emission (and UV emission, which we have not discussed) from galactic winds. Photoionization of these clouds by the energetic radiation produced through various cloud/wind interactions may well have dynamical and observational consequences. This could lead to further evaporation of the clouds, as well as to alter their ionization state further from the collision ionization equilibrium assumed in these calculations and in most X-ray spectral fitting.

Another important consequence of this will be a reduction in the X-ray emission escaping the wind, due to the absorption of a substantial fraction of the softest X-ray emission, produced at cloud/wind interfaces, by the clouds themselves. A column of $10^{20}\,\mathrm{cm}^{-2}$ (assuming solar abundances, at it is the 'metals' such as carbon, nitrogen and oxygen that dominate the photoelectric absorption cross-section) is optically thick to radiation of energy below $E \sim 0.2$ keV. The densest clouds, with individual columns of $\sim 10^{21}\,\mathrm{cm}^{-2}$ are optically thick to X-rays with energy less than ~ 0.4 keV. Such a reduction in the 'escaping' X-ray luminosity from the wind will bring the soft X-ray luminosities of our simulations into closer agreement with the observed soft X-ray luminosities of galactic winds (cf. Section 3.2.1).

4.2 Numerical resolution and cell size

For a structured Cartesian grid as employed in these simulations the resolution is proportional to the cell size used. The properties of an unresolved structure, e.g., the cold dense superbubble shell, will be averaged out over the computational cell, as the finite volume scheme employed ensures that the total mass and energy within the cell are conserved correctly. For the example of a unresolved superbubble shell, the density and thickness of the shell in the simulation will respectively be less than and greater than the true values.

In addition to affecting the absolute values of the fluid variables, finite numerical resolution can affect the dynamics of the fluid in other ways. Consider, for example, the fragmentation of the superbubble shell by RT instabilities (cf. S94). The RT instability time-scale is $\tau_{\mathrm{RT}} \propto \lambda^{1/2}$, where λ is the wavelength. The perturbations that eventually disrupt the shell have wavelengths similar to the shell thickness, so unresolved shells are artificially stable against the RT instability, and eventually fragment into artificially large pieces.

This directly affects the dynamics and properties of the coolest gas in these simulations. Fig. 19 shows images of the logarithm of the gas number density in models tbn_1, tbn1a (which have cells half the size of those in model tbn_1) and tbn1b (cells one-third the size of those in model tbn_1). It is immediately clear that the coolest densest gas in models tbn1a and tbn1b is far more structured than that in model tbn_1, and that there are many more superbubble shell fragments being dragged out with the wind.

The limitations of a finite cell size are worst for the densest, coolest gas, as it is typically found in the smallest structures. The hotter, tenuous gas, such as the thick shell of shocked halo gas or regions of shocked wind material, is on the other hand most likely to be well resolved, as it occurs in structures much larger than the cell size.

Nevertheless, poor numerical resolution of cool dense gas can affect the properties of the hot X-ray-emitting gas we are primarily interested in. The main problems here are the artificial

broadening of contact discontinuities between cool dense gas and hot tenuous gas, which creates regions of intermediate-density warm gas that will produce significant amounts of soft X-ray emission, and numerical diffusion which further acts to increasingly broaden contact discontinuities and spread material over more cells with time.

4.3 Cell size versus shell thickness

It is important to understand that the true resolution of a hydrodynamic simulation is not equal to the size of a single cell, but to the number of cells over which the code used can represent abrupt changes in the fluid variables such as shocks or contact discontinuities.

One of the great advantages of the PPM used by VH-1 is that it spreads out shocks over only two cells, a major advantage over many other numerical schemes which spread shocks out over four or five cells. Shocks are an integral part of galactic winds, as can be seen from the many shocks visible in the gas number density images shown in Figs 4–7.

As a rough estimate of how well the densest structures in our simulations are resolved, we compare the cell size to analytical estimates of the thickness of the superbubble shell before RT instabilities fragment it. A simple method of estimating the shell thickness is to use the Weaver et al. (1977) model of a constant mechanical luminosity wind blowing into a constant-density medium. Using the analytical solutions presented by Weaver et al., we can calculate the total mass in the shell and its pressure, as a function of time. Assuming that the shell cools to the minimum temperature we allow on our computational grid, $T_{\rm disc} = 6.5 \times 10^4$ K, the density of the shell follows directly from the pressure. Given the total mass of the shell and its surface area, the shell thickness follows trivially. Using the appropriate conditions that the superbubble experiences before blowout at $t \sim 3$ Myr in the thick-disc models, the shell thickness is typically $\Delta r_{\rm sh} \sim 10$ pc. Comparing this to the cell size in model tbn_1 ($\Delta x = 14.6$ pc), model tbn1a ($\Delta x = 7.3$ pc) and model tbn1b ($\Delta x = 4.9$ pc) shows that the superbubble shell is underresolved, though not drastically so.

Hence the shell fragmentation process and the number and size of superbubble fragments are controlled by the resolution of these simulations.

Note that this also means that without dramatic increases in resolution there is no point in allowing gas temperatures below the minimum gas temperature of $T_{\rm disc} = 6.5 \times 10^4$ K we impose (see Section 2.4). A superbubble shell of temperature equivalent to the optical emission-line gas observed in winds like M82's of $T \sim 10^4$ K would be $\sim$2 pc thick, and hence totally unresolved.

4.4 Numerical diffusion at contact discontinuities

As we have mentioned, numerical broadening of contact discontinuities will affect the properties of the X-ray-emitting gas. In reality, physical processes such as thermal conduction and turbulent mixing layers will also create layers of intermediate temperature and density gas between cool dense gas and hot tenuous wind material. The problem with numerically broadened contact discontinuities is that their width and structure (and hence the properties of any artificial X-ray-emitting region) is determined directly by the numerical scheme employed, and not by real physical processes.

As discussed in Fryxell et al. (1991), contact discontinuities continue to spread diffusively without limit in many Eulerian hydrodynamical codes, as the contact region moves over the computational grid. They show that of a series of numerical methods, PPM is the best at retaining sharp contact discontinuities. With the additional use of an contact discontinuity steepener algorithm, PPM spreads and maintains such discontinuities over a width of only two cells. VH-1 does not use such a contact discontinuity steepener, although the Lagrangian remap scheme used in VH-1 is believed to be better than the Eulerian PPM scheme studied by Fryxell et al. at maintaining sharp contact discontinuities without the use of a steepener (Blondin 1994).

We also employ a scheme similar to that used by Stone & Norman (1993) to reduce cooling in the region of contact discontinuities to reduce the unphysical cooling from the broadened discontinuity.

Although the efficient shock and discontinuity capturing within PPM mitigate the effects of finite numerical resolution, we cannot totally remove such effects.

4.5 Increasing numerical resolution: models tbn_1, tbn1a and tbn1b

To investigate how sensitively our results depend on the numerical resolution of our models, we ran three simulations using almost the same starburst and ISM parameters but successively increasing the resolution.

Models tbn_1 and tbn1a differ only in the cell size. Each computation cell in model tbn_1 representing a region 14.6×14.6 pc^2 in size, compared to cells of 7.3×7.3 pc^2 in model tbn1a. Model tbn1b has 3 times the resolution of model tbn_1, with cells of 4.9×4.9 pc^2, but differs from the other thick-disc models in using a cylindrical rather than spherical starburst region.

The most dramatic differences between the three simulations is in the amount of structure visible in the densest coolest gas. For example, the number of superbubble shell fragments visible at $t = 7.5$ Myr increases significantly and their size decreases as the resolution increases (see Fig. 19), for the reasons explained in Section 4.2. Otherwise the overall morphology of the wind is very similar between the different simulations, barring some minor differences in overall volume occupied by the wind.

The properties of the X-ray-emitting gas, whether measured in terms of the distribution of volume, average density, emission measure or emitted X-ray flux as a function of temperature, are all very similar between the three models when measured at the same epoch (see Fig. 20 and Table 3).

Concentrating on the properties most important observationally, the emission measure and *ROSAT* PSPC count rates, the agreement between the different models is excellent at gas temperatures above $kT \sim 0.1$ keV. For gas with temperatures below this, the higher resolution models predict systematically less emitting material and less X-ray flux. This is consistent with a picture of some, though not necessarily all, of the X-ray emission from gas at these lower temperatures being due to numerically broadened contact discontinuities.

The only other significant difference between these models we have found is in the filling factors of the X-ray-dominant gas (Table 5), where model tbn_1 has a much lower filling factor than models tbn1a and tbn1b. We do not believe the filling factors of the most of the other models are as dependent on numerical resolution as model tbn_1. In particular, in the thin-disc models

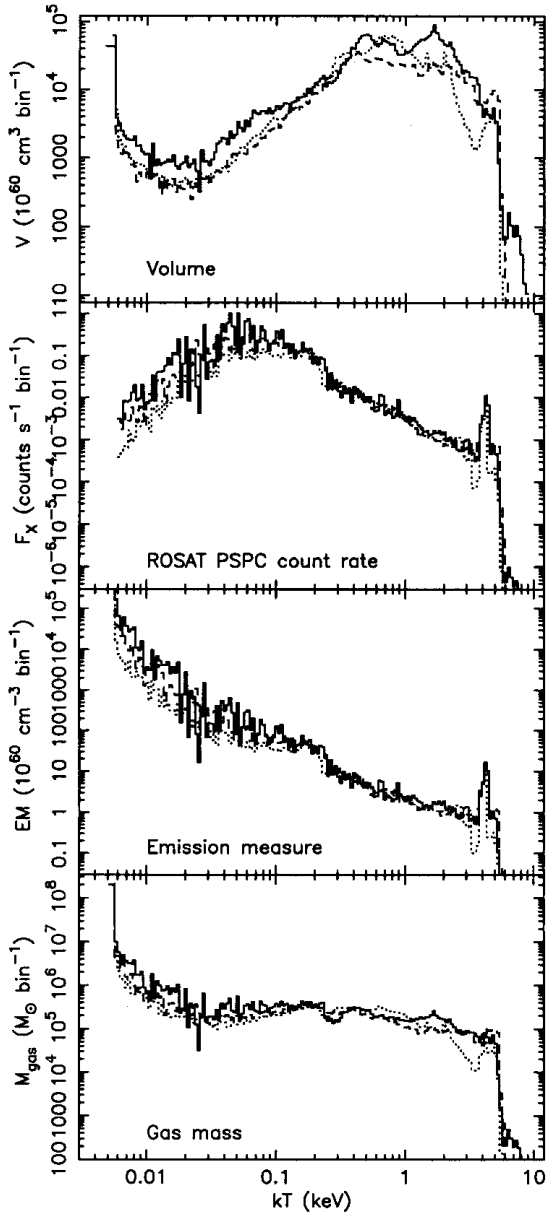

Figure 20. The distribution of volume, X-ray flux, emission measure and mass with temperature at $t = 7.5$ Myr in models tbn_1 (solid line), tbn1a (dashed) and tbn1b (dotted). Note the extremely close agreement between the emission measure and *ROSAT* count rate distributions for gas hotter than $kT \sim 0.1$ keV. For gas cooler than this temperature the higher resolution models predict less emission.

the X-ray emission is not purely from such interface regions (where numerically broadened contact discontinuities are such a problem), so increased numerical resolution should not lead to order of magnitude increases in the filling factor of the X-ray-dominant gas.

The models where the properties of the X-ray-dominant gas are most likely to be affected by resolution effects are models tbn_1, tbn_2, tbn_7 and mnd_6. This is based on the number of computational cells the most X-ray-luminous gas covers (i.e., the gas contributing 90 per cent of the soft X-ray counts in the *ROSAT* band), which is much lower in these models than in any of the other models.

Comparing the intrinsic X-ray luminosities in the *ROSAT*

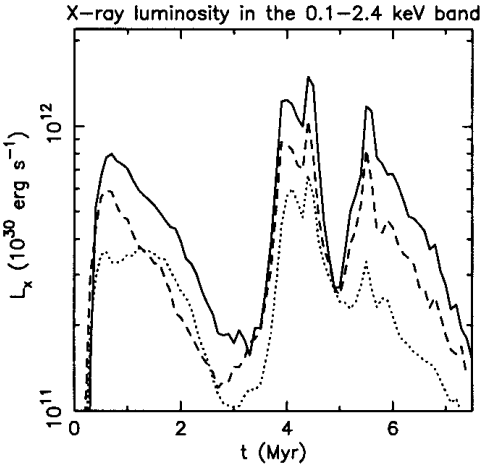

Figure 21. X-ray luminosity in the *ROSAT* 0.1–2.4 keV energy band, as function of time in models tbn_1 (solid line), tbn1a (dashed) and tbn1b (dotted). Most of the variation in X-ray luminosity is due to changes in the properties of warm gas ($kT \lesssim 0.1$ keV) as the numerical resolution increases from model tbn_1 to tbn1b.

0.1–2.4 keV energy band as a function of time between the three models also shows progressively lower X-ray luminosity accompanies higher numerical resolution (Fig. 21). This figure probably exaggerates the importance of the variation in X-ray luminosity with resolution, as what can be measured in reality will be the count rate of the attenuated emission, where the influence of the low-temperature gas so affected by numerical effects is significantly reduced. There will be much less difference between the 'observable' X-ray properties of these models than between their intrinsic X-ray luminosities.

The coolest gas in these simulations is not resolved, and would require quite substantial further increases in numerical resolution to resolve if it were allowed to cool to $T \sim 10^4$ K. The dramatic increase in the complexity of the structures associated with the coolest gas with increasing resolution does suggest to us that the complex filamentary structure of the optical emission-line gas observed in galactic winds (cf. McKeith et al. 1995; Lehnert & Heckman 1996; Shopbell & Bland-Hawthorn 1998) will be produced as a natural consequence of these models, once they achieve the necessary resolution.

The level of variation found between these three simulations implies that in these simulations, including the other thick- and thin-disc models, the emission properties of the low filling factor warm gas responsible for the majority of the soft X-ray emission ($kT \lesssim 0.1$ keV) are partially controlled by unresolved, numerically broadened, warm gas interfaces between cool dense gas and hotter wind material. Nevertheless, the important finding that the X-ray-dominant gas has low filling factor ($\lesssim$2 per cent), is likely to be robust.

Hotter gas within these winds ($kT \gtrsim 0.1$ keV), in particular volume-filling components, seems well resolved, even in our lowest resolution simulations, and therefore its properties are reasonably quantitatively correct.

5 SUMMARY

We have performed an extensive parameter study of starburst-driven galactic winds using a high resolution 2D hydrodynamical code, focusing on the best-studied galactic wind in M82. These

simulations allow us to study how the properties of galactic winds vary depending on the influence of the host galaxy's ISM distribution, starburst strength and star formation history, and the presence or absence of additional mass-loading from clouds enveloped in the wind.

In this paper we have used this sample of 12 simulations to investigate several aspects of galactic winds that are uncertain or have previously received little attention: the origin and filling factor of the gas responsible for the observed soft X-ray emission, wind energetics and energy transport efficiencies, and wind collimation and growth. In addition, we have explored in detail the influence of finite numerical resolution on the results of these simulations.

The results of this study are summarized below.

5.1 Wind collimation and confinement

(i) Thick ISM discs are required to reproduce the well-collimated wind observed in M82. Thin-disc models (e.g. S94) have wind opening angles that are too large, $\theta \gtrsim 90°$. Thick-disc models, such as that used by TB, are much better collimated, with typical opening angles $\theta \sim 40°$, much closer to the observed value of $\theta \sim 30°$.

(ii) All the simulations, regardless of ISM distribution or star formation history, fail to confine the size of the wind in the plane of the galaxy to the observed size of roughly the size of the starburst region (∼400 pc in M82). The radius of the wind in the plane of the galaxy grows to between 1 and 2 kpc over the 10-Myr period covered by these simulations. The confinement of galactic winds within the plane of the galaxy remains a problem, as initially pointed out by Tenorio-Tagle & Muñoz-Tuñón (1997). There is clearly something interesting happening in the central regions of starburst galaxies, perhaps related to the existing circumnuclear molecular rings, that must be able to confine the base of the wind over time-scales of ∼10 Myr.

5.2 X-ray emission in galactic winds

(i) The gas responsible for the majority of the soft X-ray emission detectable by *ROSAT* comes from very low filling factor ($\eta \sim 0.01$ to 2 per cent) gas that contains very little of the total mass or energy of the wind. As a result, X-ray observations with *ROSAT*, *ASCA*, *Chandra* or *XMM* will give only lower limits on the mass and energy content of galactic winds.

(ii) The winds in these models contain gas at a wide range of temperatures and densities. In terms of a phase description there is a phase continuum of states rather than any particular well-defined characteristic temperatures or densities.

(iii) The majority of the wind volume in almost all of these models is filled with hot gas, covering the temperature range $10^{6.5}$ to $10^{7.5}$ K. This gas is only a weak source of soft X-ray emission due to its low density.

(iv) The soft X-ray emission in these models does not come from any single well-defined temperature gas, but from a very wide range of temperatures from $T \sim 10^5$ K to 10^8 K. Fitting the resulting complex X-ray spectra with standard simple spectral models is likely to give misleading results.

(v) In all of our models, regions of interaction between the hot wind and cooler denser material (originally part of the ambient ISM) give rise to a large fraction of the soft X-ray emission. In these simulations this X-ray emission can be from shock-heated ambient gas, and from the numerically broadened interfaces between cool dense and hot tenuous gas, although it is very difficult to discriminate between the two cases. In some of the models, in particular the mass-loaded models, the starburst region itself or the free wind region can be significant sources of soft X-ray emission. In the thin-disc models shock-heated halo gas is also an important source of X-ray emission.

(vi) The primary variable affecting the soft X-ray luminosity of the galactic winds in these models is the density and distribution of the ambient, volume-filling, component of the ISM. The energy injection rate from the starburst, and mass-loading from dense clouds, do have a significant but secondary effect on the X-ray luminosity.

(vii) Mass-loading of the wind, either within the starburst region itself, or from clouds distributed more generally throughout the ISM, is not necessary to produce galactic winds of M82's luminosity or characteristic soft X-ray temperature.

(viii) Hard X-ray emission from galactic winds is dominated by the starburst region itself. The ratio of hard X-ray to soft X-ray luminosity is typically $L_{\rm X,hard}/L_{\rm X,soft} \sim 10^{-2}$. We confirm S94's conclusion that the hard X-ray emission from starburst galaxies is *not* due to thermal emission associated with the starburst-driven wind.

5.3 Wind energetics

(i) Galactic winds are efficient at transporting the energy supplied by the starburst out of the plane of the galaxy. As radiative losses are low, galactic winds seem likely to be good sources of heating for the IGM and ICM. This is in contrast to their low efficiency at moving mass out of the disc of starburst galaxies.

(ii) The energy within galactic winds is predominantly (∼60 per cent) kinetic energy of hot gas [$10^{6.5} \leq T(K) \leq 10^{7.5}$]. This is significantly different from the standard superbubble, where the most of the energy is in the thermal energy of the hot bubble interior. The change from thermally dominated to kinetically dominated energetics occurs when the superbubble breaks out of the disc.

(iii) Hot gas also contains the majority (∼60 per cent) of the total thermal energy content of these winds. Exceptions to this rule are models with strong centralized mass-loading, where warm gas [$10^{5.5} \leq T(K) \leq 10^{6.5}$] dominates the thermal energy content.

(iv) The total energy content of galactic winds appears extremely difficult to measure directly. Soft X-ray observations probe only denser low filling factor gas containing relatively little (≲10 per cent) of either the total thermal or kinetic energy. Measuring the kinetic energy of the warm and hot phases is also hampered by the lack of any direct measurements of this gas's velocity.

5.4 Concluding remarks

Our findings have major implications for the ultimate aim behind the study of galactic winds: measuring quantitatively the transport of mass, metal-enriched gas and energy out of star-forming galaxies.

These simulations measure, for the first time, the observationally important filling factor of the X-ray-emitting gas. In all models, even those including different forms of mass-loading, we find that the soft X-ray emission from galactic winds comes from low filling factor ($\eta \lesssim 2$ per cent) gas. This gas contains only a

small fraction of the mass and energy of the wind. Most of the thermal and kinetic energy of these outflows is in a hot, volume-filling, component, which is extremely difficult to probe observationally due to its low density and hence low emissivity.

We also find that galactic winds are efficient at transporting energy out of the host galaxy, primarily in the form of the kinetic energy of hot, $T \sim 10^{6.5}$ to $10^{7.5}$ K, gas. This is an important finding, as it suggests that starburst-driven winds are a good mechanism for reheating the IGM and ICM, as required by recent observations.

In Paper II we shall present a direct comparison between the spectral properties and spatial distribution of the soft X-ray emission in these models and the existing X-ray data on M82, along with a discussion of which of these models best reproduces M82's observed properties.

ACKNOWLEDGMENTS

It is a pleasure to thank the referee, A. Ferrara, both for the scientific value of his comments and the punctuality of his response! We also thank the numerous people whose comments on this work we have found enlightening, in particular Timothy Heckman, Martin Ward, Duncan Forbes, Trevor Ponman, Crystal Martin and Martin Norbury. DKS acknowledges financial support from a PPARC studentship, a Teaching Assistantship from the School of Physics and Astronomy at the University of Birmingham, and through NASA grant NAGW 3138. IRS acknowledges support from a PPARC Advanced Fellowship.

REFERENCES

Allen M. L., Kronberg P. P., 1998, ApJ, 502, 218
Arthur S. J., Henney W. J., 1996, ApJ, 457, 752
Begelman M. C., Fabian A. C., 1990, MNRAS, 244, 26P
Blondin J. M., 1994, The VH-1 Users Guide, Univ. Virginia
Blondin J. M., Kallman T. R., Fryxell B. A., Taam R. E., 1990, ApJ, 356, 591
Bradamante F., Matteucci F., D'Ercole A., 1998, A&A, 337, 338
Bregman J. N., Schulman E., Tomisaka K., 1995, ApJ, 439, 155
Calzetti D., Meurer G. R., Bohlin R. C., Garnett D. R., Kinney A. L., Leitherer C., Storchi-Bergmann T., 1997, AJ, 114, 1834
Cappi M. et al., 1999, A&A, 350, 777
Chevalier R. A., Clegg A. W., 1985, Nat, 317, 44(CC)
Cole S., Aragon-Salamanca A., Frenk C. S., Navarro J. F., Zepf S. E., 1994, MNRAS, 271, 781
Collela P., Woodward P. R., 1984, J. Comp. Phys., 54, 174
Cottrell G. A., 1977, MNRAS, 178, 577
Cowie L. L., McKee C. F., Ostriker J. P., 1981, ApJ, 247, 908
Dahlem M., 1997, PASP, 109, 1298
Dahlem M., Heckman T. M., Fabbiano G., Lehnert M. D., Gilmore D., 1996, ApJ, 461, 724
Dahlem M., Weaver K. A., Heckman T. M., 1998, ApJS, 118, 401
de Gouveia Dal Pino E. M., Medina Tanco G. A., 1999, ApJ, 518, 129
Dekel A., Silk J., 1986, ApJ, 303, 39
Della Ceca R., Griffiths R. E., Heckman T. M., 1997, ApJ, 485, 581
De Young D. S., Heckman T. M., 1994, ApJ, 431, 598
D'Ercole A., Brighenti F., 1999, MNRAS, 309, 941
Fabbiano G., 1988, ApJ, 330, 672
Ferrara A., Shchekinov Yu., 1993, ApJ, 417, 595
Field G. B., 1965, ApJ, 142, 531
Freedman W. L. et al., 1994, ApJ, 427, 628
Fryxell B., Müller E., Arnett D., 1991, ApJ, 367, 619
Godunov S. K., 1959, Matematicheskii Sbornik, 47, 271
González Delgado R. M., Leitherer C., Heckman T., Cerviño M., 1997, ApJ, 483, 705
Gorjian V., 1996, AJ, 112
Götz M., McKeith C. D., Downes D., Greve A., 1990, A&A, 240, 52
Hartquist T. W., Dyson J. E., Pettini M., Smith L. J., 1986, MNRAS, 221, 715
Hartquist T. W., Dyson J. E., Williams R. J. R., 1997, ApJ, 482, 182
Heckman T. M., 1998, in Woodward C. E., Shull J. M., Thronson H. A. Jr., eds, ASP Conf. Ser. Vol. 145, Origins. Astron. Soc. Pac., San Francisco, p. 127
Heckman T. M., Armus L., Miley G. K., 1990, ApJS, 74, 833
Heckman T. M., Lehnert M. D., Armus L., 1993, in Shull J. M., Thronson H. A. Jr., eds, The Environment and Evolution of Galaxies. Kluwer, Dordrecht, p. 455
Heckman T. M., Lehnert M. D., Strickland D. K., Armus L., 2000, ApJ, in press
Kauffman G., Guiderdoni B., White S. D. M., 1994, MNRAS, 267, 981
Klein R. I., McKee C. F., Collela P., 1994, ApJ, 420, 213
Klein U., Wielebinski R., Morsi H. W., 1988, A&A, 190, 41
Lehnert M. D., Heckman T. M., 1996, ApJ, 462, 651
Leitherer C., Heckman T. M., 1995, ApJS, 96, 9 (LH95)
Loewenstein M., Mushotzky R. F., 1996, ApJ, 466, 695
Lugten J. B., Watson D. M., Crawford M. K., Genzel R., 1986, ApJ, 311, L51
MacLow M.-M., Ferrara A., 1999, ApJ, 513, 142
MacLow M.-M., McCray R., 1988, ApJ, 324, 776
McCarthy P. J., Heckman T., van Breugel W., 1987, AJ, 92, 264
McKeith C. D., Greve A., Downes D., Prada F., 1995, A&A, 293, 703
McLeod K. K., Rieke G. H., Rieke M. J., Kelly D. M., 1993, ApJ, 412, 111
Martin C. L., 1999, ApJ, 513, 156
Masai K., 1994, ApJ, 437, 770
Meurer G. R., Heckman T. M., Leitherer C., Kinney A., Robert C., Garnett D. R., 1995, AJ, 110, 2665
Mewe R., Kaastra J. S., Liedahl D. A., 1995, Legacy, 6, 16
Miyamoto M., Nagai R., 1975, PASJ, 27, 533
Moran E. C., Lehnert M. D., 1997, ApJ, 478, 172
Morrison R., McCammon D., 1983, ApJ, 270, 119
Muxlow T. W. B., Pedlar A., Wilkinson P. N., Axon D. J., Sanders E. M., de Bruyn A. G., 1994, MNRAS, 266, 455
Nakai N., Hayashi M., Handa T., Sofue Y., Hasegawa T., 1987, PASJ, 39, 685
Norman C. A., Ferrara A., 1996, ApJ, 467, 280
O'Connell R. W., Mangano J. J., 1978, ApJ, 221, 62
O'Connell R. W., Gallagher J. S., Hunter D. A., Colley W. N., 1995, ApJ, 446, L1
Pettini M., Steidel C. C., Adelburger K. L., Dickinson M., Giavalisco M., 2000, ApJ, 528, 96
Ponman T. J., Cannon D. B., Navarro J. F., 1999, Nat, 397, 135
Ptak A. F., 1997, PhD thesis, Univ. Maryland
Ptak A., Serlemitsos P., Yaqoob T., Mushotzky R., Tsuru T., 1997, AJ, 113, 1286
Puxley P. J., Brand P. W. J. L., Moore T. J. T., Mountain C. M., Nakai N., Yamashita T., 1989, ApJ, 345, 163
Raymond J. C., Smith B. W., 1977, ApJS, 35, 419
Read A. M., Ponman T. J., Strickland D. K., 1997, MNRAS, 286, 626
Reuter H.-P., Klein U., Lesch H., Wielebinski R., Kronberg P. P., 1994, A&A, 282, 724
Salpeter E. E., 1955, ApJ, 121, 161
Satyapal S., Watson D. M., Pipher J. L., Forrest W. J., Greenhouse M. A., Smith H. A., Fischer J., Woodward C. E., 1997, ApJ, 483, 148
Seaquist E. R., Odegard N., 1991, ApJ, 369, 320
Seaquist E. R., Carlstrom J. E., Bryant P. M., Bell M. B., 1996, ApJ, 465, 691
Shopbell P. L., Bland-Hawthorn J., 1998, ApJ, 493, 129
Silich S. A., Tenorio-Tagle G., 1998, MNRAS, 299, 249
Somerville R. S., Primack J. R., 1999, MNRAS, 310, 1087
Stark A. A., Gammie C. F., Wilson R. W., Bally J., Linke R. A., Heiles C., Hurwitz M., 1992, ApJS, 79, 77

Stevens I. R., Blondin J. M., Pollock A. M. T., 1992, ApJ, 386, 265
Stone J. M., Norman M. L., 1993, ApJ, 413, 198
Strickland D. K., Stevens I. R., 1998, MNRAS, 297, 747
Strickland D. K., Stevens I. R., 1999, MNRAS, 306, 43
Strickland D. K., Ponman T. J., Stevens I. R., 1997, A&A, 320, 378
Strickland R., Blondin J. M., 1995, ApJ, 449, 727
Suchkov A. A., Balsara D. S., Heckman T. M., Leitherer C., 1994, ApJ, 430, 511 (S94)
Suchkov A. A., Berman V. G., Heckman T. M., Balsara D. S., 1996, ApJ, 463, 528 (S96)
Swaters R. A., Sancisi R., van der Hulst J. M., 1997, ApJ, 491, 140
Tenorio-Tagle G., Muñoz-Tuñón C., 1997, ApJ, 478, 134
Tenorio-Tagle G., Muñoz-Tuñón C., 1998, MNRAS, 293, 299 (TT)
Thornton K., Gaudlitz M., Janka H.-Th., Steinmetz M., 1998, ApJ, 500, 95
Tomisaka K., Bregman J. N., 1993, PASJ, 45, 513 (TB)
Tomisaka K., Ikeuchi S., 1988, ApJ, 330, 695 (TI)
Tsuru T. G., Awaki H., Koyama K., Ptak A., 1997, PASJ, 49, 619
Vader J. P., 1986, ApJ, 305, 669
Wang Q. D., Walterbos R. A. M., Steakley M. F., Norman C. A., Braun R. A., 1995, ApJ, 439, 176
Watson M. G., Stanger V., Griffiths R. E., 1984, ApJ, 286, 144
Weaver R., McCray R., Castor J., Shapiro P., Moore R., 1977, ApJ, 218, 377
Zezas A. L., Georgantopoulos I., Ward M. J., 1998, MNRAS, 301, 915

This paper has been typeset from a TEX/LATEX file prepared by the author.